JAERI-Tech
2002-063

JP0250394

FABRICATION OF PROTOTYPE MOCKUPS OF ITER SHIELDING BLANKET WITH SEPARABLE FIRST WALL

July 2002

Yasuo KOSAKU, Toshimasa KURODA, Mikio ENOEDA,
Toshihisa HATANO, Satoshi SATO and Masato AKIBA

日本原子力研究所
Japan Atomic Energy Research Institute

本レポートは、日本原子力研究所が不定期に公刊している研究報告書です。
入手の問合わせは、日本原子力研究所研究情報部研究情報課（〒319-1195　茨城県那珂郡東海村）あて、お申し越しください。なお、このほかに財団法人原子力弘済会資料センター（〒319-1195　茨城県那珂郡東海村日本原子力研究所内）で複写による実費頒布をおこなっております。

This report is issued irregularly.
Inquiries about availability of the reports should be addressed to Research Information Division, Department of Intellectual Resources, Japan Atomic Energy Research Institute, Tokai-mura, Naka-gun, Ibaraki-ken 319-1195, Japan.

© Japan Atomic Energy Research Institute, 2002

編集兼発行　日本原子力研究所

Fabrication of Prototype Mockups of ITER Shielding Blanket with Separable First Wall

Yasuo KOSAKU, Toshimasa KURODA, Mikio ENOEDA, Toshihisa HATANO, Satoshi SATO and Masato AKIBA

Department of Fusion Engineering Research,
Naka Fusion Research Establishment,
Japan Atomic Energy Research Institute
Naka-machi, Naka-gun, Ibaraki-ken

(Received May 31, 2002)

Design of shielding blanket for ITER-FEAT applies the first wall which has the separable structure from the shield block for the purpose of radio-active waste reduction in the maintenance work and cost reduction in fabrication process. Also, it is required to have various types of slots in both of the first wall and the shield block, to reduce the eddy current for reduction of electro-magnetic force in disruption events. This report summarizes the demonstrative fabrication of the ITER shielding blanket with separable first wall performed for the shielding blanket fabrication technology development, under the task agreement of G 16 TT 108 FJ (T420-2) in ITER Engineering Design Activity Extension Period. The objectives of the demonstrative fabrication are:

• to demonstrate the comprehensive fabrication technique in a large scale component (e.g the joining techniques for the beryllium armor/copper alloy and copper alloy/SS, and the slotting method of the FW and shield block);
• to develop an improved fabrication method for the shielding blanket based on the ITER-FEAT updated design.

In this work, the fabrication technique of full scale separable first wall shield blanket was confirmed by fabricating full width Be armored first wall panel, full scale of 1/2 shield block with poloidal cooling channels. As the R&D for updated cooling channel configuration, the fabrication technique of the radial channel shield block was also demonstrated. Concluding to the all R&D results, it was demonstrated successfully that the fabrication technique and optimized conditions in the results obtained under the task agreement of G 16 TT 95 FJ (T420-1) was applicable to the prototype of the separable first wall blanket module. Additionally, basic echo data of ultra-sonic test method (UT) was obtained to show the applicability of UT method for in tube access detection of defect on the Cu alloy/SS tube interface.

Key words; ITER Shielding Blanket, Separable First Wall, Large Scale Fabrication, Joining Technique, Be, DSCu, SS, Non-destructive Examination, UT

分離第一壁型ITER遮蔽ブランケットプロトタイプの製作

日本原子力研究所那珂研究所核融合工学部
古作 泰雄・黒田 敏公・榎枝 幹男・秦野 歳久・佐藤 聡・秋場 真人

(2002年5月31日受理)

ITER-FEATの遮蔽ブランケット設計では、放射性廃棄物量の低減と製作コスト低減のために分離第一壁型の構造を採用している。さらに、ディスラプションの際の渦電流を低く抑え電磁力を低減するために、多様なスリット構造を必要とする。本報告は、ITER EDA延長期間中の、分離第一壁型遮蔽ブランケットの製作技術開発を目的としたタスク合意G 16 TT 108 FJ (T420-2)に基づいて行われた製作実証試験の結果をまとめたものである。本報の製作性実証試験の目的は、
・ベリリウムアーマーと銅合金、銅合金とステンレス鋼の接合技術と第一壁及び遮蔽ブロックへのスリット施工技術等の大規模コンポーネントに対する有効性を実証すること。
・ITER-FEATにおける最新の設計に基づく遮蔽ブランケット製作技術の改良技術を開発すること。
である。

このような観点から、実機と同じ寸法の幅のベリリウムアーマー付き第一壁パネルと1/2の大きさのポロイダル方向冷却流路の遮蔽ブロックを製作し、実規模の分離第一壁型遮蔽ブランケットの製作性を実証した。また、設計の進展に従い、径方向冷却流路の遮蔽ブロックの製作を実証した。これらの実機製作性実証では、タスクT420-1において明らかにした最適な接合条件を適用し、その有効性を実規模で実証した。さらに、銅合金とステンレス鋼の接合部の非破壊検査手法として超音波探傷法(UT)の適用の可能性を明らかにした。

那珂研究所：〒311-0193　茨城県那珂郡那珂町向山801-1

Contents

目次

1 Executive Summary

Design of shielding blanket for ITER-FEAT applies the first wall which has the separable structure[1] from the shield block for the purpose of radio-active waste reduction in the maintenance work and cost reduction in fabrication process. Also, it is required to have various types of slots in both of the first wall and the shield block, to reduce the eddy current for reduction of electro-magnetic force in disruption events[1]. Fabrication technology development has been performed in the ITER EDA period to achieve the fabrication techniques for such unique structure of the shielding blanket of ITER. Within the ITER R&D Tasks for blanket fabrication development, T216+, T420-1 and T508-3, the basic fabrication techniques for the separable first wall and shield block have been developed. These included: the solid HIP technology for DSCu/SS[2,3,4] and Be/DSCu[5,6], and the prototypical blanket module mockups for integrated first wall structure[7,8,9,10] including the high heat flux testing of the first wall mockup[11] using JEBIS in JAERI[11]. The present task is to demonstrate the fabrication technique for separable FW / blanket (option B) design using above mentioned techniques. With respect to the previous fabrication technology, development of technologies for the use of CuCrZr instead of DSCu for a lower cost alternative. The basic heat treatment condition and HIP condition with SS are to be investigated in this task.

The objectives of this task are:

- to demonstrate the comprehensive fabrication technique in a large scale component (e.g the joining techniques for the beryllium armor/copper alloy and copper alloy/SS, and the slotting method of the FW and shield block);
- to develop an improved fabrication method for the shielding blanket based on the ITER-FEAT updated design.

According to the objectives, the task was divided into two subtasks. Subtask 1 demonstrates the final feasibility of the fabrication technique of separable first wall type shielding blanket. Subtask 2 develops the improved fabrication technique for the application of CuCrZr heat sink material. This report presents the results of Subtask 1.

Subtask 1 was performed for the demonstration of manufacturing methods of FW and/or shields (option B design). By subtask 1, major critical issues for the fabrication of real scale shield blanket were clarified. The major critical issues clarified in this task are as follows.

(1) Joining technique of Be armor and Cu alloy heat sink, and Cu alloy heat sink and SS base panel
(2) Slit formation for FW panels
(3) Slit formation of a shield block
(4) Thick header plate welding technique and welding deformation of shield blocks
(5) Welding technique for one quarter shield blocks
(6) Fabricability of radial cooling channel shield block
(7) Non destructive examination method development for FW Cu alloy/SS cooling channel

The specific items in subtask 1 are as follows.

1) full width of Be armored FW model fabrication
2) 1/2 poloidal channel shield block fabrication including EB welding joining
3) 1/4 radial channel shield block fabrication
4) UT testing for basic defect sensing technique development

Item of "1) full width of Be armored FW model fabrication" covered issue (1) and (2). Item of "2) 1/2 poloidal channel shield block fabrication including EB welding joining" covered issues(3), (4) and (5). Item "3) 1/4 radial channel shield block fabrication" covered issue (6). Item "4) UT testing for basic defect sensing technique development" covered issue (7).

With respect to the full width of Be armored FW model fabrication, the fabrication technique of real scale width mockup was demonstrated. Fabrication soundness was confirmed by

various tests such as, PVD Cu interlayer thickness, HIP condition control, deformation by heat treatment of HIP process final dimension inspection and destructive tests including surface roughness measurement of slit grooving surface, macroscopic observation, optical micro-graph observation, SEM observation, EPMA analysis and 4 point bending test. The followings are the conclusions.

1) Feasibility of Be HIP joining in the curvature around top and bottom of the FW panel was obtained.
2) Soundness of interlayer plasma spray on full width FW surface of heat sink. was demonstrated.
3) Clearance between larger size of Be armor tiles and Cu alloy heat sink surface was well controlled to obtain good joining.
4) Usage of larger size of Be armor tiles to minimize Be pre-HIP treatment cost was demonstrated.
5) Slit grooving and deformation due to stress release by grooving was not detected.

With respect to the 1/2 poloidal channel shield block fabrication including EB welding joining, the major basic information necessary for fabrication of the shield block for the option B blanket module were clarified. Clarified issues are as follows

(1) Slit grooving technique by water jet method
- grooving speed, nozle diameter
- jet stopper material and shape of the stopper rods

(2) EB welding of two 1/4 shield block
- Optimized EB welder operation condition and minimum slit width
- Effect of the EB welding over TIG welding of the toroidal header plugs

(3) TIG welding of header cap plates
- Shape of welding line
- Deformation after welding

All issues are common to the updated design of shield block which features radial cooling channel.

With respect to the fabrication of 1/4 radial channel shield block, it was clarified that basically, there is no additional critical issue to the fabrication technique of poloidal channel shield block. All fabrication process were carried out successfully. Critical issues are already clarified in the result of 1/2 poloidal channel shield block fabrication.

With respect to UT testing for basic defect sensing technique development, two types of UT probes (10 MHz and 30 MHz) were tested by 0.3 mm x 2 mm to 0.9 mm x 2 mm artificial defects. Test results were concluded as follows.

(1) Type 2 (30 MHz) is more sensitive than type 1(10 MHz).
(2) Side of bent part gives less effect of bending and for this reason high sensitivity is expected.
(3) Inside or outside of bent part gives lower sensitivity.
(4) Automatic defect sensing may normally require 6 dB safety factor. Incorporating this factor, 0.9 mm is the minimum defect size which can be guaranteed by detection inspection.

2 Objectives

The R&D contained in this report has been divided into two sub-tasks:
1. Demonstration of a comprehensive fabrication method for the ITER-FEAT module design by fabrication of a prototype
2. Development of the joining techniques for low cost alternative materials (e.g. investigation on suitable manufacturing process parameter and assessment of mechanical properties for the use of CuCrZr).

In order to demonstrate the manufacturing feasibility of the ITER-FEAT shielding blanket module design, a representative size prototype will be fabricated using the solid HIP method. Additionally, mechanical properties of the non-irradiated CuCrZr/SS and CuCrZr/CuCrZr HIP bonded joints will be obtained to survey the treatment condition. This report summarizes the result of Subtask 1:

Sub-Task 1 Prototype fabrication - Fabrication of prototype of separable FW blanket option B design -

Explore and demonstrate manufacturing methods for producing FW and/or shields (option B design). It will also provide information on achievable bonding quality and costs from different manufacturing procedures.

Sub-Task 1: Prototype fabrication

1) Prototype
- According to the design progress, a shielding blanket prototype mock-up will be fabricated with one first wall panel and including the penetration holes. The first wall with Be armour tiles will be attached to the shield block.
- The first wall will be manufactured with the deep slots for the minimization of the electromagnetic loads.
- Cooling pipe routing and other necessary configurations on the rear side of the shield block are featured according to the design progress.
- According to the design progress for the ITER FEAT, a mock-up of SS shield block with slots will also be fabricated. A sketch of the FW and shield block prototypes is shown in Fig. 1.
- Hydraulic tests by using water will be performed and the data of pressure drop and flow distribution will be collected.

Fabrication/Test Conditions

Size	:~ 1600 mm x 1000 mm
HIP conditions	:1050°C/150 MPa/2 hrs for DSCu/SStube/SS plate (single step) and TBD for Be/DSCu (second step),
Number of mock-ups	: one
FW configuration	: poloidally flat with slotted surface, separable structure
Number of FW	: one
Coolant flow test	: room temperature, max. 800 l/min of total flow rate

Thermo-mechanical tests will be performed on the FW prototype at a facility in Europe or other countries. This will be decided based on availability of facilities in the future. The total credit of this task will not change even if the heat load tests are performed.

3 Task Report

3.1 Fabrication of Prototype

3.1.1 Design Target and Objectives of Prototype Fabrication

Task contents of prototype fabrication

Subtask 1 is subject to explore and demonstrate manufacturing methods for producing FW and/or shields (option B design)[1]. It will also provide information on achievable bonding quality and costs from different manufacturing procedures of different cooling channel of shield blocks. Task specification for prototype fabrication is as follows.

a) According to the design progress, a shielding blanket prototype mock-up will be fabricated with one first wall panel and including the penetration holes. The first wall with Be armour tiles will be attached to the shield block.

b) The first wall will be manufactured with the deep slots for the minimization of the electromagnetic loads.

c) Cooling pipe routing and other necessary configurations on the rear side of the shield block are featured according to the design progress.

d) According to the design progress for the ITER FEAT, a mock-up of SS shield block with slots will also be fabricated. A sketch of the FW and shield block prototypes is shown in Fig. 1.1-1[1].

e) Hydraulic tests by using water will be performed and the data of pressure drop and flow distribution will be collected.

Fabrication and test conditions are as follows.

Size	:	~ 1600 mm x 1000 mm
HIP conditions	:	1050°C/150 MPa/2 hrs for DSCu/SStube/SS plate (single step) and TBD for Be/DSCu (second step),
Number of mock-ups:		one
FW configuration:		poloidally flat with slotted surface, separable structure
Number of FW	:	one
Coolant flow test	:	room temperature, max. 800 l/min of total flow rate

The possibility of thermo-mechanical tests of the Be armored FW prototype at a facility in Europe or other countries were investigated, however, for scheduling reason, the plan of HHF test was abandoned.

Design basis of shielding blanket

Figure 1.1-1 shows the schematic configuration of option B shield blanket with poloidal cooling channels for shield block. The characteristic features of the shield blanket are as follows.

1) Be armor, Cu alloy heat sink and SS base panel
2) Separable first wall panel cooled by parallel cooling channel
3) Center shaft support of FW panel
4) Shield block consists of welded 4 SS blocks
5) Two options of shield block cooling channel directions, poloidal direction, and radial direction

Figure 1.1-2[1] shows the illustration of the FW panel with center shaft support. Figure 1.1-3 shows cross sectional view of one of 4 unit shield blocks for one shield block. In this case, the cooling channels are poloidal direction. The coolant headers are on top and bottom of shield blocks. Figure 1.1-4[1] shows the another option of shield block design which features radial direction cooling channels with front headers. In this design, the main header in on the front plane of the shield block and coolant flow is achieved by coaxial structure, as shown in Fig. 1.1-5[1].

Fabrication procedure and critical fabrication techniques

Figure 1.1-6 and 1.1-7 show the proposed fabrication procedure for first wall panel[1]. Figure 1.1-8 and 1.1-9 show the procedure for poloidal channel shield block. Primary critical issues of the fabrication are as follows.

(1) Joining technique of Be armor and Cu alloy heat sink, and Cu alloy heat sink and SS base panel. (HIP conditions for Be/Cu alloy, Cu alloys/SS plate are already
(2) Slit formation for FW panels
(3) Joining of FW panel and support legs and welding deformation of FW panel
(4) Slit formation of a shield block
(5) Thick header plate welding technique and welding deformation of shield blocks
(6) Welding technique for one quarter shield blocks
(7) Attachment of center shaft FW panel to shield block by rear connection

Figure 1.1-10 shows the task execution schedule. The task of prototype fabrication is devided into three essential parts, full width of Be armored FW model fabrication (section 1.2), 1/2 poloidal channel shield block fabrication including EB welding joining (section 1.3) and 1/4 radial channel shield block fabrication (section 1.4). Item of "full width of Be armored FW model fabrication" covers task contents a) and b). Item of "1/2 poloidal channel shield block fabrication including EB welding joining" covers task content c) and e). Item "1/4 radial channel shield block fabrication" covers d).

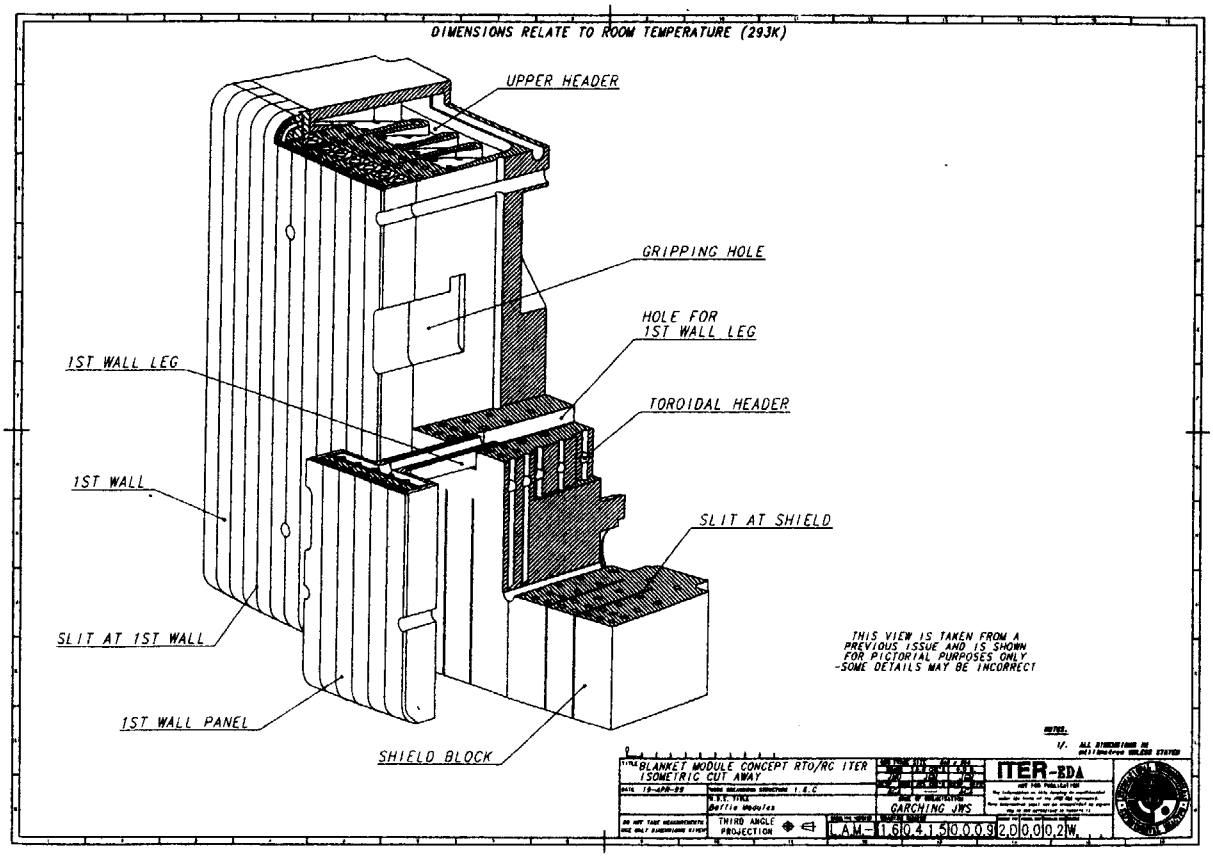

Fig. 1.1-1 Cutaway view of poloidal coolant channel shield blanket with separable first wall panels

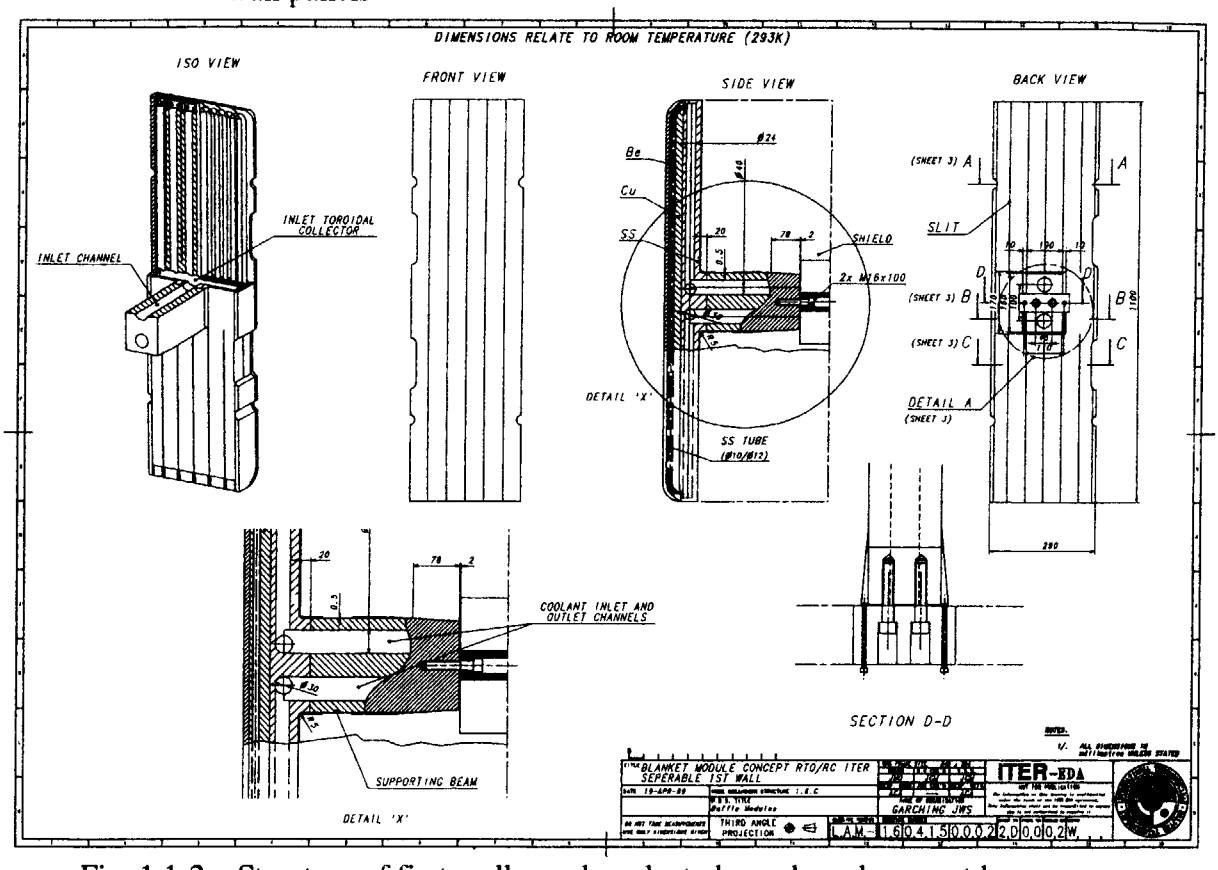

Fig. 1.1-2 Structure of first wall panel coolant channels and support leg

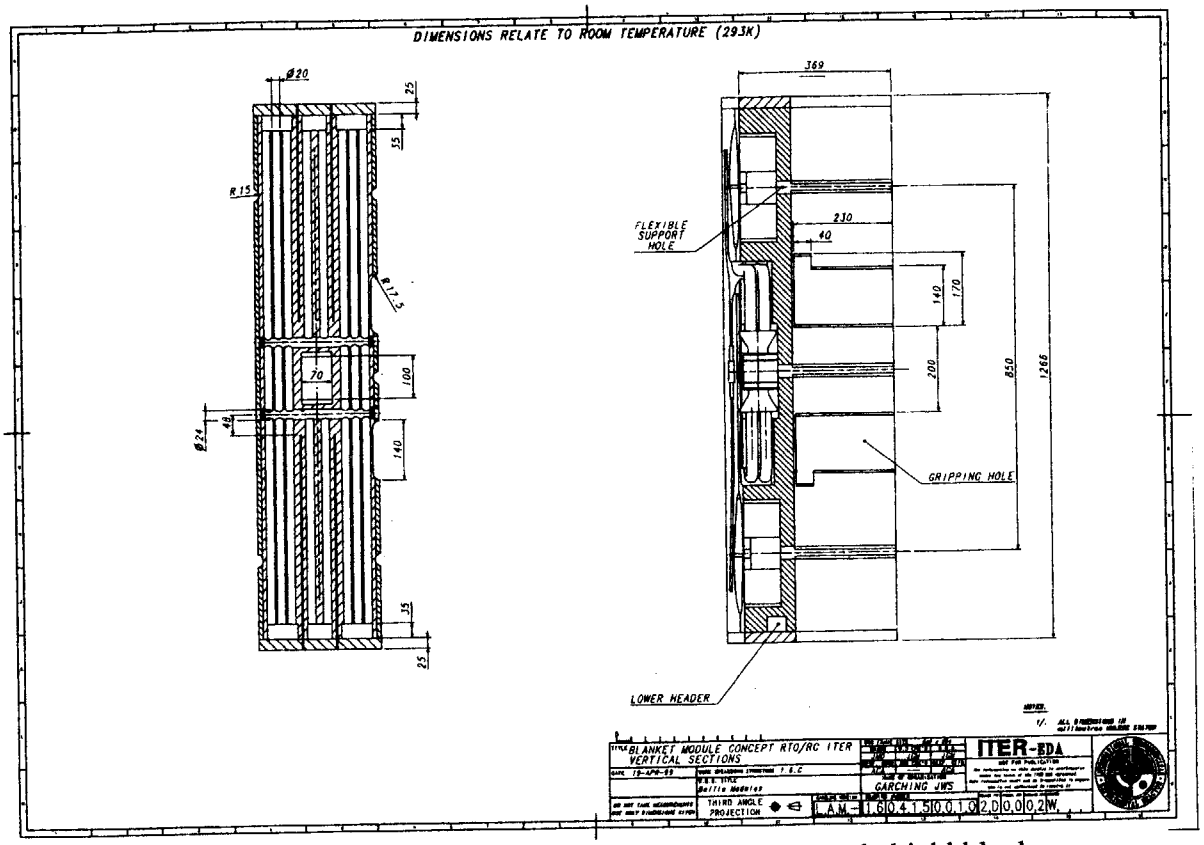

Fig. 1.1-3 Poloidal cross section of poloidal channel shield block

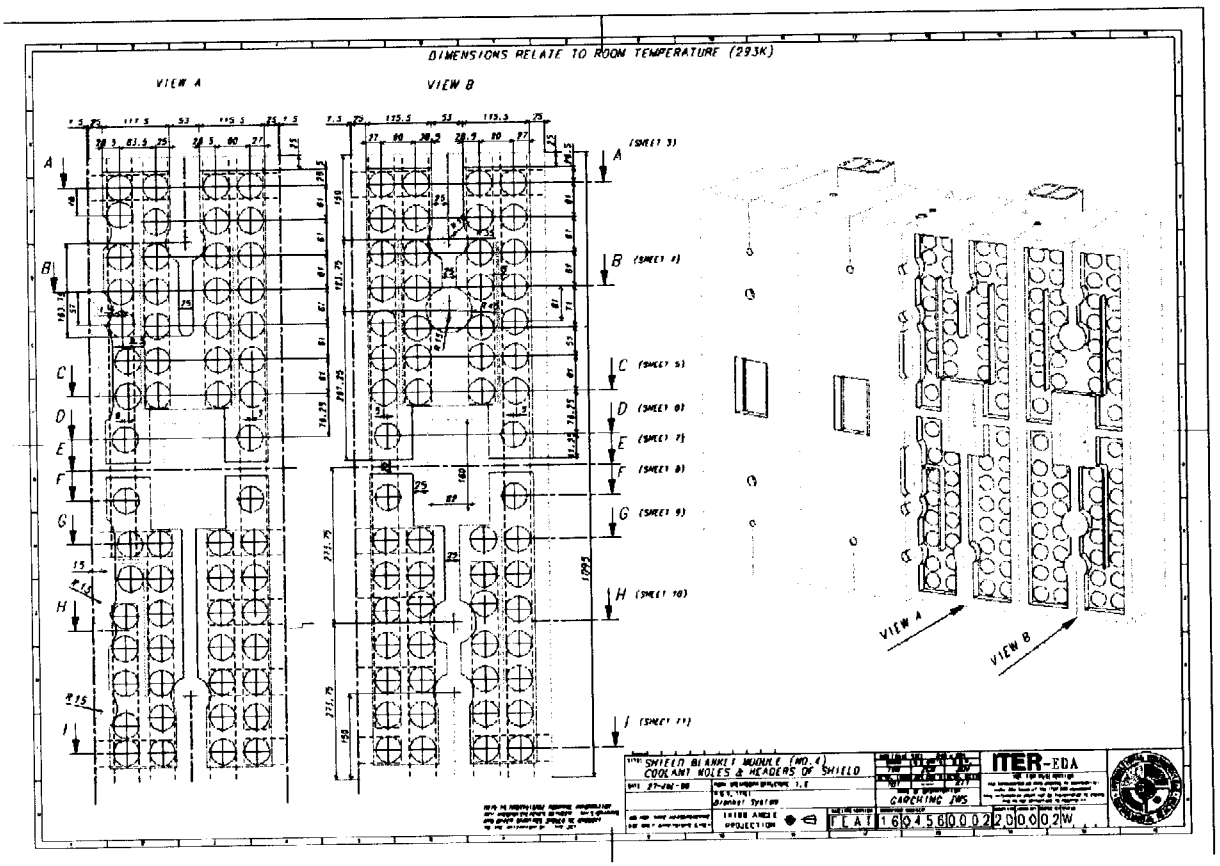

Fig. 1.1-4 Shield block with radial coolant channels

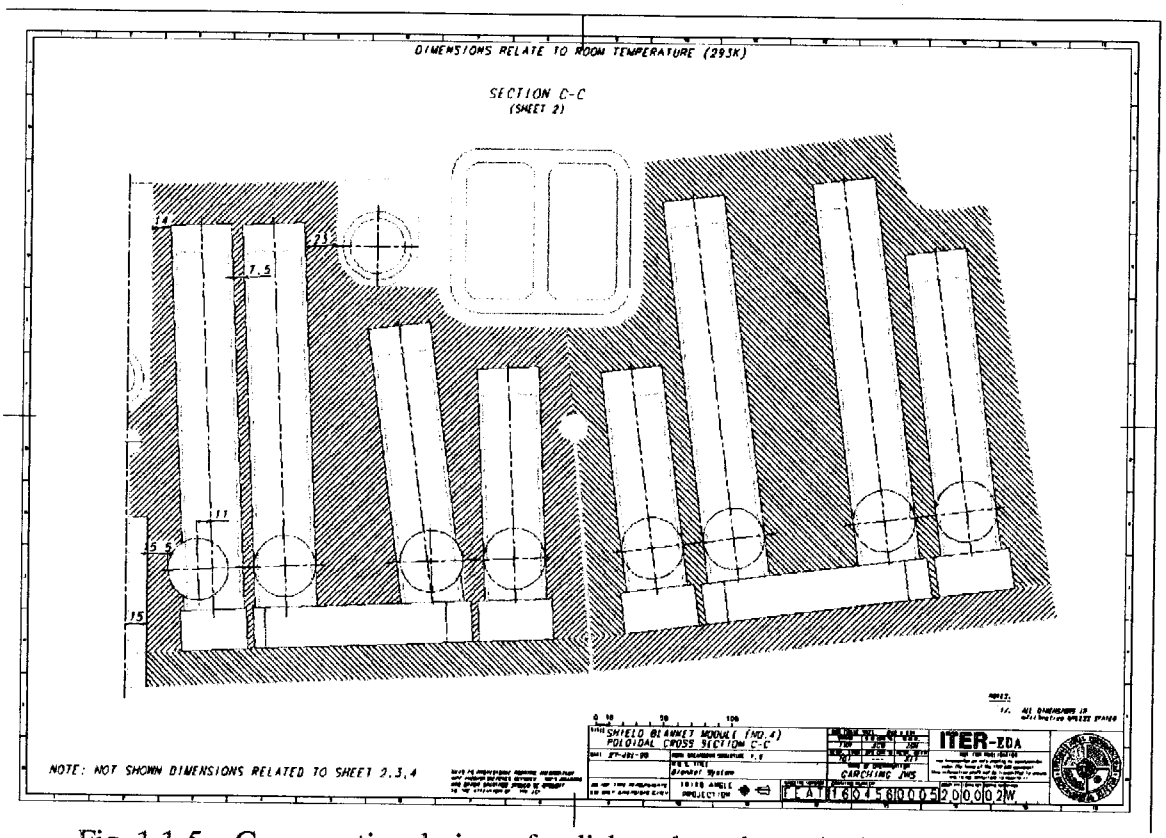

Fig. 1.1-5 Cross sectional view of radial coolant channel with co-axial flow

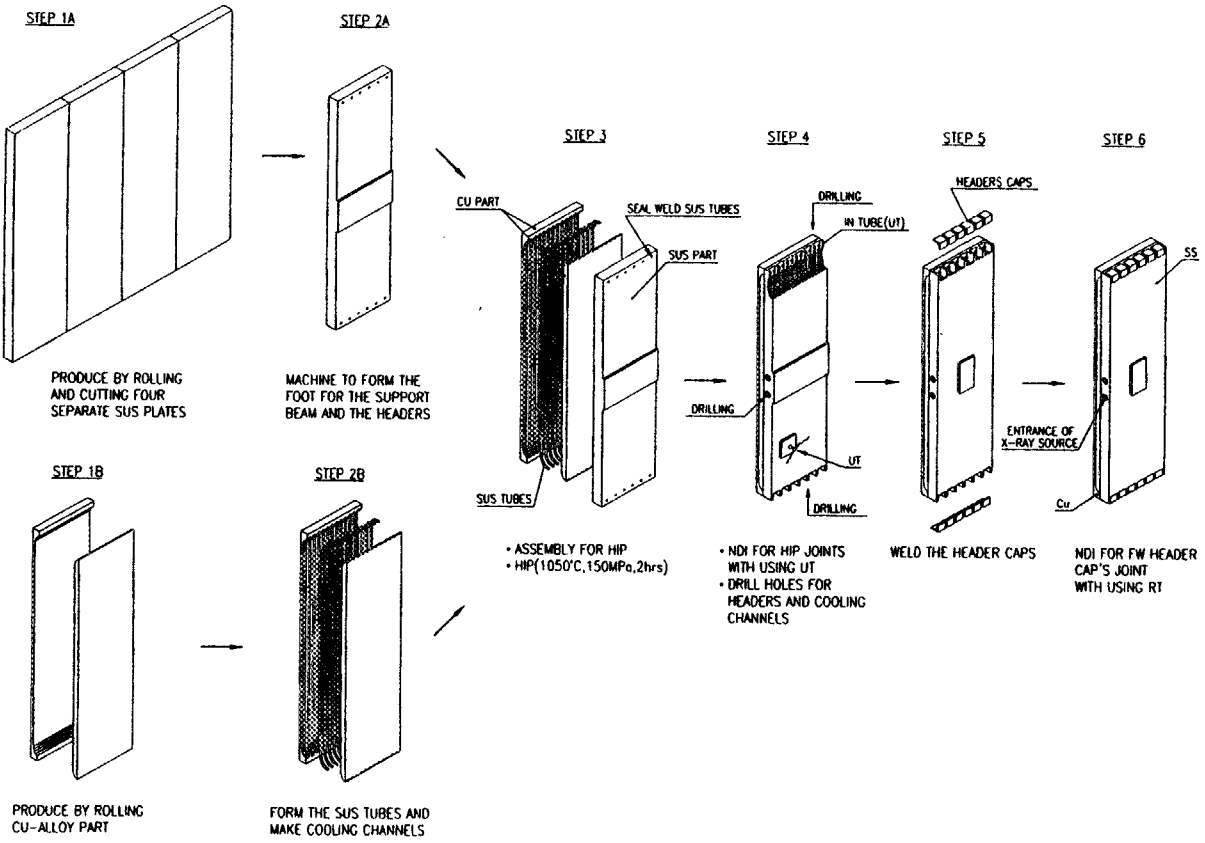

Fig. 1.1-6 Fabrication procedure of first wall panel (1/2)

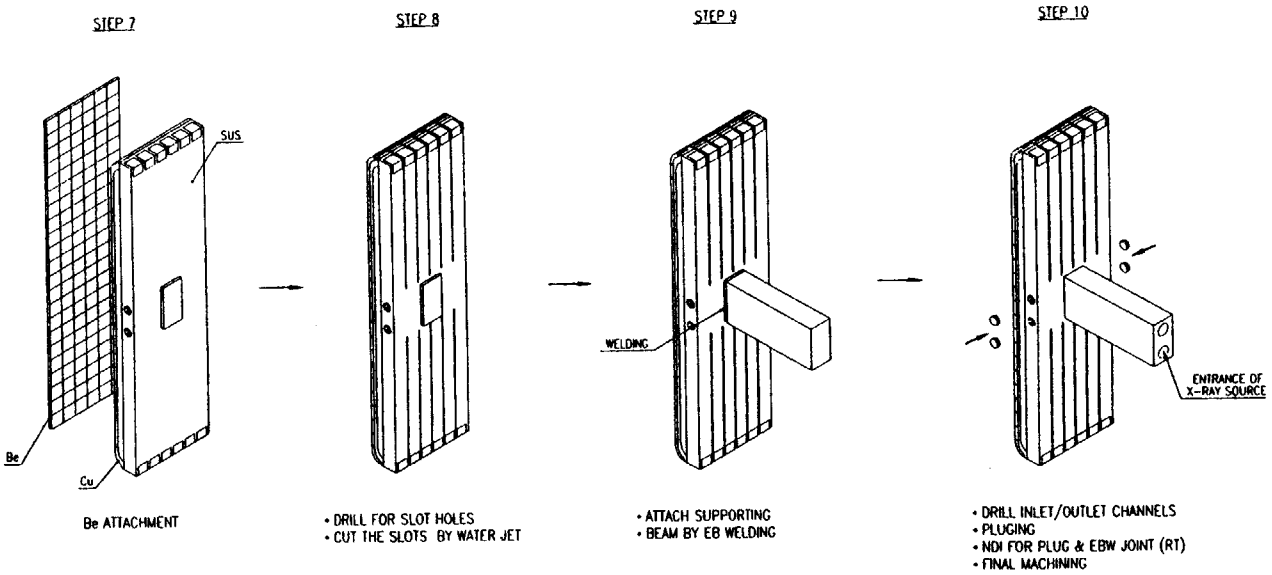

Fig. 1.1-7 Fabrication procedure of first wall panel (2/2)

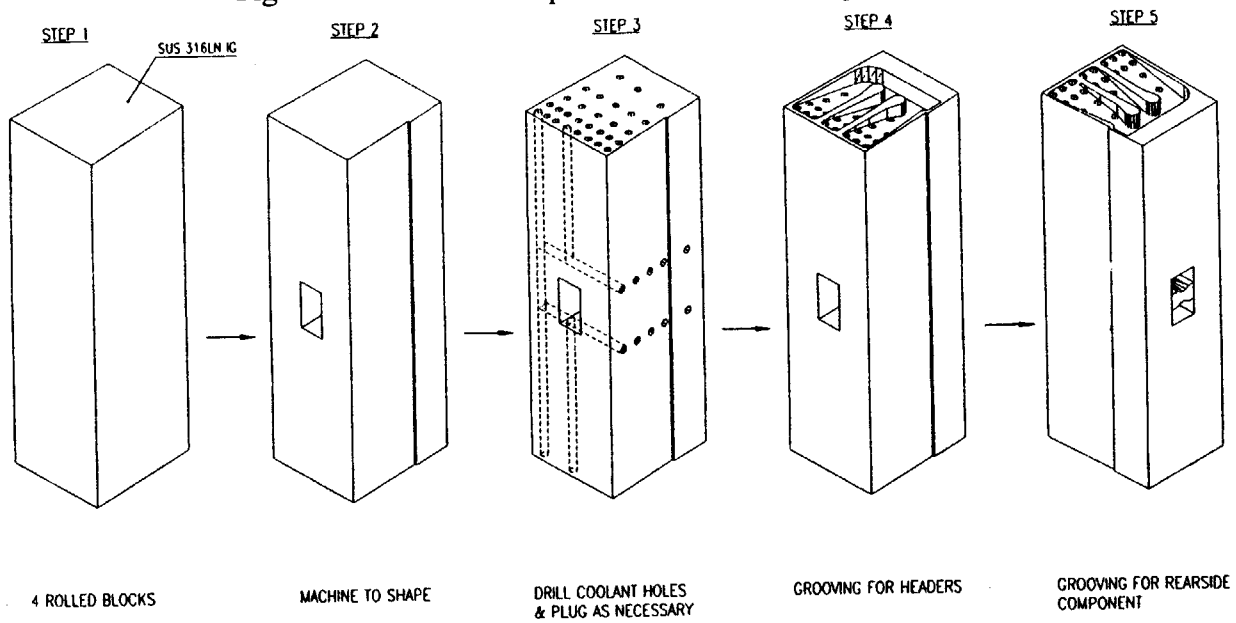

Fig. 1.1-8 Fabrication procedure of poloidal channel shield block (1/2)

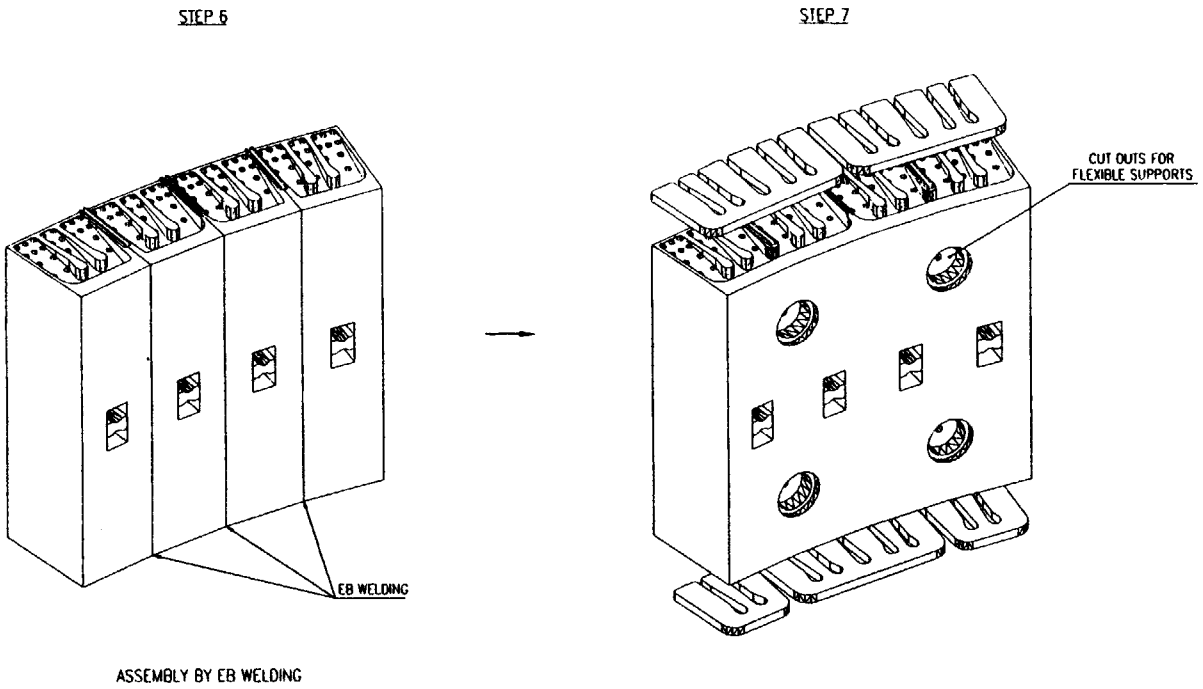

Fig. 1.1-9 Fabrication procedure of poloidal channel shield block (2/2)

Item#		2000									2001						
		4	5	6	7	8	9	10	11	12	1	2	3	4	5	6	7
#1-1	Prototype with a Be/DSCu/SS FW panel																
	MAterial purchase																
	DSCu																
	SS																
	FW panel machining before HIP																
	HIP																
	header welding, shaft machin																
	Be HIP																
	center shaft welding																
	Shield block 1/4 block drilling, header weld																
	WJ slit machining																
	EBW between blocks																
	final machining																
	Total assembly																
	Inspection																

Fig. 1.1-10 Task execution schedule for T420-2 Sub-task 1 " Prototype Fabrication"

3.1.2 Be Armored FW Model Fabrication

3.1.2.1 Design of Be Armored FW Model

Figure 1.2.1-1 shows the design sketch of Be armored FW partial model, which is dedicated to show feasibility of Be HIP joining technique in real scale width of FW panel (about 39 cm). Figure 1.2.1-2 shows the overall flow diagram of fabrication procedure. Figure 1.2.1-3 to 1.2.1-6 shows the detailed fabrication steps of each fabrication processes with important control values. Fabrication technique of DSCu/SS first wall was well developed in task T420-1. This task followed the optimized procedure and the condition in T420-1 for the basic part of the FW mockup. With respect to the basic Be/DSCu HIP condition, task T508-3 was already completed and justified the feasibility of two kinds of joining condition and interlayer composition. One is the Al base interlayer with HIP temperature of 555 °C. The other is PVD Cu interlayer with HIP temperature of 625 °C. Both cleared the representative high heat flux tests conducted by OHBIS facility in Japan[5,6]. From fabrication cost point of view, the technique using Cu interlayer is simpler and cont reductive than the technique using Al base interlayer. Also, consideration of avoiding frequent disruption event, which gives the peaking of high temperature to Be armor, higher HIP temperature was selected for demonstration of fabrication technique. One can say demonstration of Cu interlayer technique can be extrapolated to Al base technique because the major difference is only the material of PVD interlayer. Critical points to be confirmed in this section are summarized as follows.

1) Feasibility of Be HIP joining in the curvature around top and bottom of the FW panel.
2) Soundness of interlayer plasma spray on full width FW surface of heat sink
3) Clearance control between larger size of Be armor tiles and Cu alloy heat sink surface to obtain good joining
4) Usage of larger size of Be armor tiles to minimize Be pre-HIP treatment cost
5) Slit grooving and deformation due to stress release by grooving

3.1.2.2 Fabrication Process Control

Material

DSCu

As the heat sink material, DSCu GlidCop AL25 was used. The material of DSCu was purchased from OMG. Table 1.2.2-1 sows the material data sheet.

Stainless steel

For the base plate of the FW, stainless steel SUS 316L was used. SUS 316L was manufactured by NKK corporation. Table 1.2.2-2 shows chemical composition of the raw material.

Be

For Be armor material, grade "S-65" was used. Material block was purchased from Brush Wellman, Ltd. Table 1.2.2-3 shows the material data.

Fabrication process

Figure 1.2.2-1 to 1.2.2-14 show the photographs of the mockup during major fabrication process. Figure 1.2.2-1 to 1.2.2-6 show the fabrication process of the first wall panel basement fabricated by HIP joining of SS basement and Cu alloy heat sink by using established fabrication technique in task T420-1. Figure 1.2.2-7 shows the basement coated by interlayer, OFCu, by plasma spray method (PVD). Figure 1.2.2-8 shows preparation process of Be tiles before assembly. Figure 1.2.2-9 shows the assembled set of Be pre-HIP processed Be tiles on the Cu alloy heat sink after interlayer processing step. Figure 1.2.2-10 shows the mockup

canned by TIG welding and baking for Be HIP process. Figure 1.2.2-11 shows Be armored FW mockup immediately after HIP decanning before slitting process. Figure 1.2.2-12 shows slit forming process by wire sew. Figure 1.2.2-13 shows the slit forming process by EDM and used EDM electrode element. Figure 1.2.2-14 shows the final product of Be armored FW mock up after slitting and honing

3.1.2.3 Inspections and Destructive Examinations

In the course of the fabrication progress, important critical processes of fabrication was inspected to control the soundness of fabrication. The critical points are PVD Cu interlayer thickness, HIP condition control, deformation by heat treatment of HIP process final dimension inspection and destructive tests as the post fabrication test.

a) PVD Cu thickness and Be HIP surface roughness

PVD Cu thickness was measured to confirm thickness is thick enough more than 10 micro-m as the target value. Measurement was done by the Carotest in toroidal direction and poloidal direction. Measurement results are sown in Figs. 1.2.3-1 and 1.2.3-2 for poloidal and toroidal direction, respectively. As can be seen from Fig. 1.2.3-1, interlayer thickness is thick enough for sound HIP joining, however, thickness deviates around the rounded curvature. This is due to the small angular of PVD spray to the surface of the DSCu. Deviation was 5 to maximum 10 micro-m. This value is to be incorporated to the setting of interlayer spray thickness. As can be seen from Fig. 1.2.3-2, PVD thickness distribution in toroidal direction has small deviation.

HIP surface of Be is required to be less than 1.6 micro m roughness finish to obtain sound HIP joining. Table 1.2.3-1 shows the measured value of surface roughness on 5 raw material Be tiles which were joined by HIP. All measurement values satisfied the roughness criteria of less than 1.6 micro m.

b) HIP temperature and pressure control

In the course of Be HIP process, the temperature and the pressure in the HIP furnace was controlled to 620 ± 10 C and 1500 ± 10 kgf/cm^2. Figure 1.2.3-3 shows the record of a representative temperature of the mockup in HIP process (not the control history). As can be seen from this figure, control was successfully achieved. Also the post-HIP heat treatment was recorded to show the 430 C for 4 hours were given.

c) Deformation measurement after slit grooving

Deformation by HIP

After HIP heat treatment, one of the major concern was the deformation by residual stress relief by slitting because of the difference of thermal expansion rate of DSCu and Be. The measurement was performed with laser location meter by the following procedure.

1) In the de-canning process, the bottom of the SS basement was machined to determine the standard plane.

2) The dimension was measured after de-canning before slitting first, which gives the standard dimension before residual stress relief.

3) Slitting without changing the standard SS basement.

4) Measurement of the Be armor surface shape.

The absolute deviation of the height of Be surface was less than 10 - 20 micro-m. This value is nearly equal the surface roughness. The direct comparison of the height distribution before and after slitting gives too large error to determine the real deformation only by the stress release by slitting. Thus, the comparison of the relative shapes along the measurement lines obtained by

the best fitting in each cases were used to identify the deformation. By this method, the deformation was determined no larger than 0.1 mm.

Deformation after slit grooving

Table 1.2.3-2 summarizes measured deformation. The total width of the open slit edge was enlarged in 0.2 mm. Be armor tiles became concaved shape in 0.058 mm.

d) Dimension inspection

Final dimension of major important location of the mockup was measured to show the soundness of finish dimension. All dimensions are in the range of less than 2% even for the slit width (2 mm). Incorporating the deformation of the mockup after Be HIP process, the dimensional soundness was demonstrated very well.

e) Destructive tests

Destructive tests consists of six kinds of tests, surface roughness measurement of slit grooving surface, macroscopic observation, optical micro-graph observation, SEM observation, EPMA analysis and 4 point bending test. Test piece of the destructive tests was cut along the A-A line shown in Fig. 1.2.1-1.

Surface roughness measurement of slit grooving surface

Surface roughness of the Slit grooved surface was measured on the Be slit and penetration slit from Be to SS base. Figure 1.2.3-4 shows the specific points of measurement. Measurement were performed on the surface of Be, DSCu and SS of a penetration slit (poloidal direction), and Be surface of toroidal and poloidal Be slits. Measured values are listed in Table 1.2.3-3. As can be seen from the table, surface roughness is less than 3 micro-m, which value is not such large that it will affect to the function of armor tile.

Macroscopic observation

Figure 1.2.3-5 shows the location of macroscopic photograph. Each location was selected to show representative part of Be/DSCu HIP joint of both sides of penetration slit and toroidal Be slit. Figure 1.2.3-6 shows the photogarphs.

Optical micro-graph observation

Optical observation were performed to show the soundness of Be/DSCu HIP joints and slit bottom finish. Figure 1.2.3-7 shows the location for the observation. Observation locations for slit finish were selected to observe both of penetration slit and Be slit. In case of penetration slit, observation point is in the SS part. While, in case of Be slit, slit bottom is in DSCu part near by HIP joint. Figure 1.2.3-8 (a) shows the observation of 4 different locations of HIP joints. As can be seen from this figure, sound joining is still preserved even after slit grooving process. Also, bottom finish of both slits are well rounded and especially Be HIP joining kept soundness for Be slit grooving which stops near by HIP joint. Figure 1.2.3-8 (b) shows the observation of the slit bottom parts in 2 different locations. As can be seen from this figure, the soundness of the slit grooving finish was confirmed.

SEM/EPMA observation

SEM observation and EPMA analysis were performed to verify the chemical species distribution near HIP joint. Figure 1.2.3-9 shows the locations for the observation. Figure 1.2.3-10(a) and (b) shows the SEM image and EPMA analysis for Be, O, Al, and Cu at locations 1, 2, 3 and 4.

The distribution showed the typical chemical form for Be/DSCu joint with Cu interlayer.

Four point bending test

Figure 1.2.3-11 shows the location of the sampling of 4 point bending test pieces. Also, the dimension of the test piece is shown in the same figure. The measured value of the 4 point bending were compared with the typical values of Be/DSCu HIP joints by Cu interlayer, obtained in the screening test of HIP condition. Table 1.2.3-4 shows the obtained bending strength. In the table, typical 4 point bending strength were shown for room temperature, 200 C and 400 C. Tests were performed in room temperature, however, the destructive surface didn't show brittle fracture. The value of strength were almost the same. Thus, Be HIP joining showed soundness.

3.1.2.4 Section Conclusions

The fabrication technique of the Be armor HIP joining for real scale width mockup was demonstrated in this work from the aspect of the following issues by PVD Cu interlayer thickness, HIP condition control, deformation by heat treatment of HIP process final dimension inspection and destructive tests including surface roughness measurement of slit grooving surface, macroscopic observation, optical micro-graph observation, SEM observation, EPMA analysis and 4 point bending test.

1) Feasibility of Be HIP joining in the curvature around top and bottom of the FW panel.
2) Soundness of interlayer plasma spray on full width FW surface of heat sink
3) Clearance control between larger size of Be armor tiles and Cu alloy heat sink surface to obtain good joining
4) Usage of larger size of Be armor tiles to minimize Be pre-HIP treatment cost
5) Slit grooving and deformation due to stress release by grooving

Table 1.2.2-1 Material data sheet of DSCu

LOT number	04910902
Heat number	C-8973
Dimension	plate 1.25 inch x 11 inch x 24 inch
Chemical composition	
Copper	99.46 %
Aluminum	0.25 %
Iron	0.0013 %
Lead	0.0006 %
Boron	0.02 %
Mechanical properties	
UTS	441 MPa
YS	353 MPa
Elongation	27 %
Apparent hardness	72
Conductivity	91 %IACS

Table 1.2.2-2 Material mill sheet of SUS 316L

Chemical composition	%
Iron	Balance
C	0.006 %
Si	0.006 %
Mn	0.008 %
P	0.0003 %
S	0
Ni	12.26 %
Cr	17.37 %
Mo	2.09 %

Table 1.2.2-3 Material data sheet of Be (S-65)

LOT number	5063
Dimension	block 2.874" x 6.14174" x 6.9685"
Chemical composition	
Beryllium assay	99.60 %
Beryllium oxide	0.5 %
Carbon content	0.020 %
Iron content	0.0600 %
Aluminum	0.02 %
Magnesium content	< 0.0100 %
Silicon content	0.0200 %
Other metallic-Ea.	< 0.0400 %
Mechanical properties	
Ftu (Top Long.)	55.00 ksi
Fty (Top Long.)	39.40 ksi
Elongation (Top Long.)	4.40 %
Ftu (Top Trans.)	58.60 ksi
Fty (Top Trans.)	40.00 ksi
Elongation (Top Trans.)	6.40 %
Grain size	9.2 micro m
Theoretical density	100.3 %

Table 1.2.3-1 Surface roughness data of Be tiles for HIP

Tile #	Parallel to polishment direction [micro m]		Perpendicular to polish direction [micro m]	
#1-1	0.28	0.27	0.32	0.41
#1-2	0.28	0.40	0.36	0.53
#2-1	0.74	0.49	0.69	0.51
#2-2	0.33	0.40	0.39	0.54
#3	0.39	0.37	0.67	0.65

Table 1.2.3-2 Deformation after slit grooving

Location	Before slit grooving			After slit grooving		
Width A	299.13			299.33		
Width B	299.10			299.08		
	X	Y	Z	X	Y	Z
Height #1*	10.004	12.004	-0.001	9.999	12.005	0.000
Height #2	10.004	62.005	-0.008	10.014	62.016	-0.044
Height #3	10.007	111.997	-0.012	10.002	112.001	-0.070
Height #4	10.007	161.995	-0.012	10.005	162.002	-0.069
Height #5	10.007	212.006	-0.011	10.013	212.016	-0.046
Height #6*	10.006	261.995	-0.001	10.011	261.996	0.003
Height #7	90.002	262.004	0.006	90.014	262.007	0.025
Height #8	90.001	211.994	-0.010	90.014	212.008	-0.031
Height #9	90.002	161.996	-0.008	90.007	162.000	-0.051
Height #10	90.002	111.994	-0.008	90.007	112.006	-0.054
Height #11	90.000	61.995	-0.007	90.006	62.000	-0.039
Height #12*	90.002	11.999	-0.002	90.010	12.016	0.003

*: Vartual plane was defined.

Table 1.2.3-3 Measured value of surface roughness on slit surface

Location #	Be	DSCu	SS
1	1.6	2.1	2.6
2	1.7	2.1	2.2
3	1.6		
4	3.1		
5	2.5		

Table 1.2.3-4 Observed values of 4 point bending strength of Be/DSCu HIP joint by Cu interlayer.

	room temperature	200 C	400 C
Results from screening	231.2, 258.1 MPa	141.4, 145.3 MPa	131.3, 135.3 MPa
This work	211.2, 233.5, 229.6 MPa	---	---

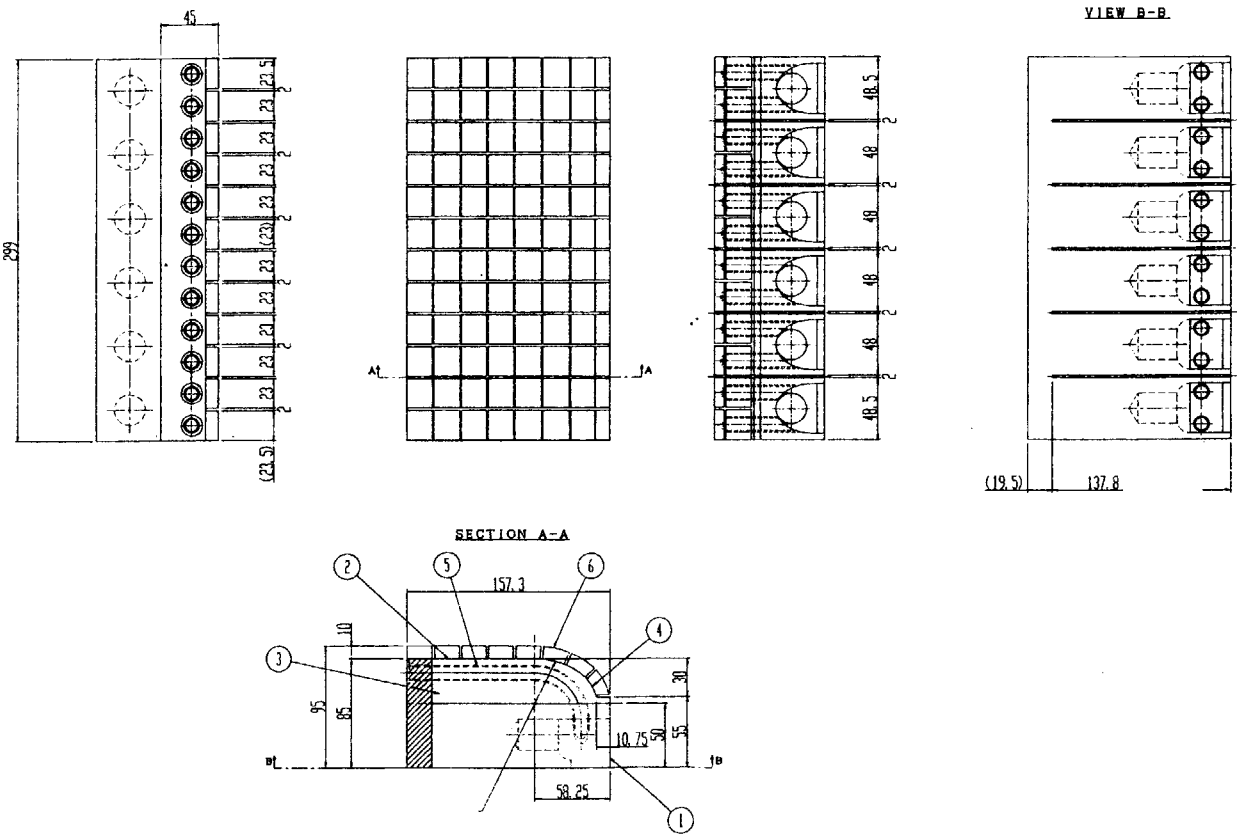

Fig. 1.2.1-1 Design of full width Be armored first wall mockup

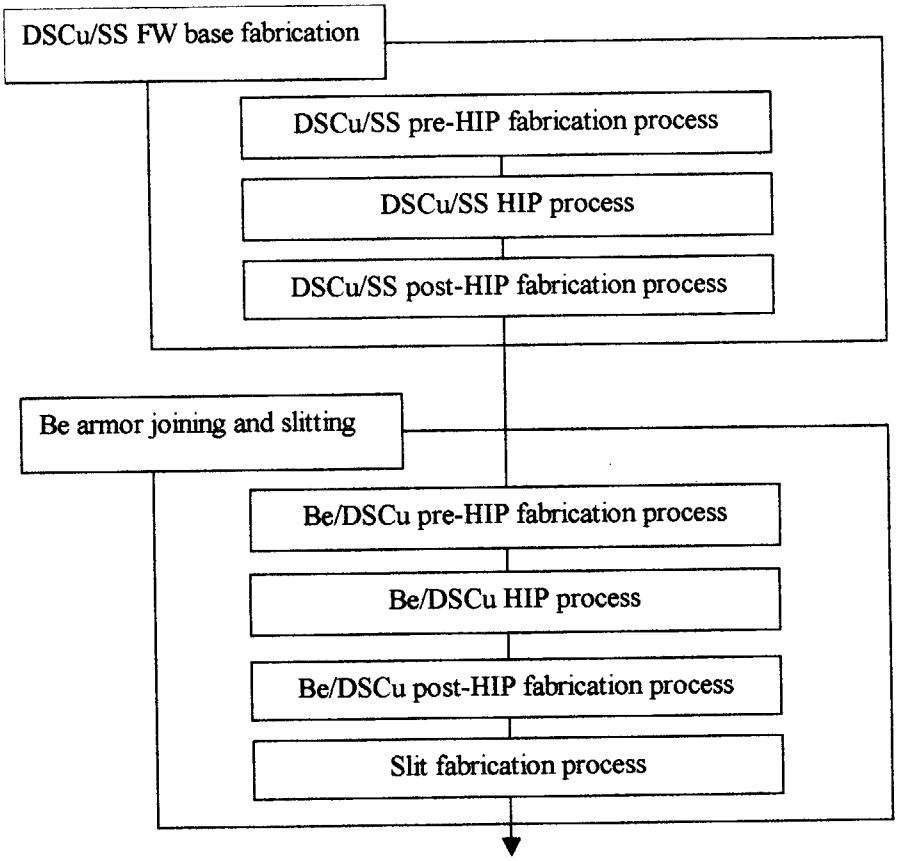

Fig. 1.2.1-2 Overall flow diagram of fabrication of Be armored first wall mockup

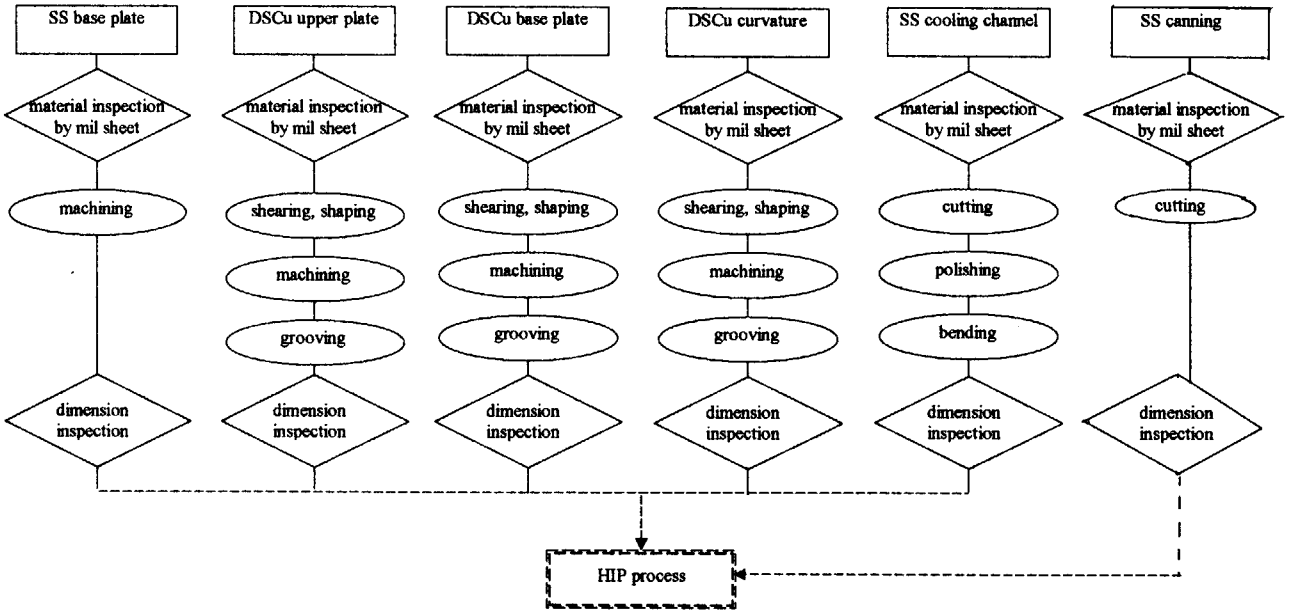

Fig. 1.2.1-3 Fabrication procedure before HIP of DSCu/SS of Be armored first wall mockup

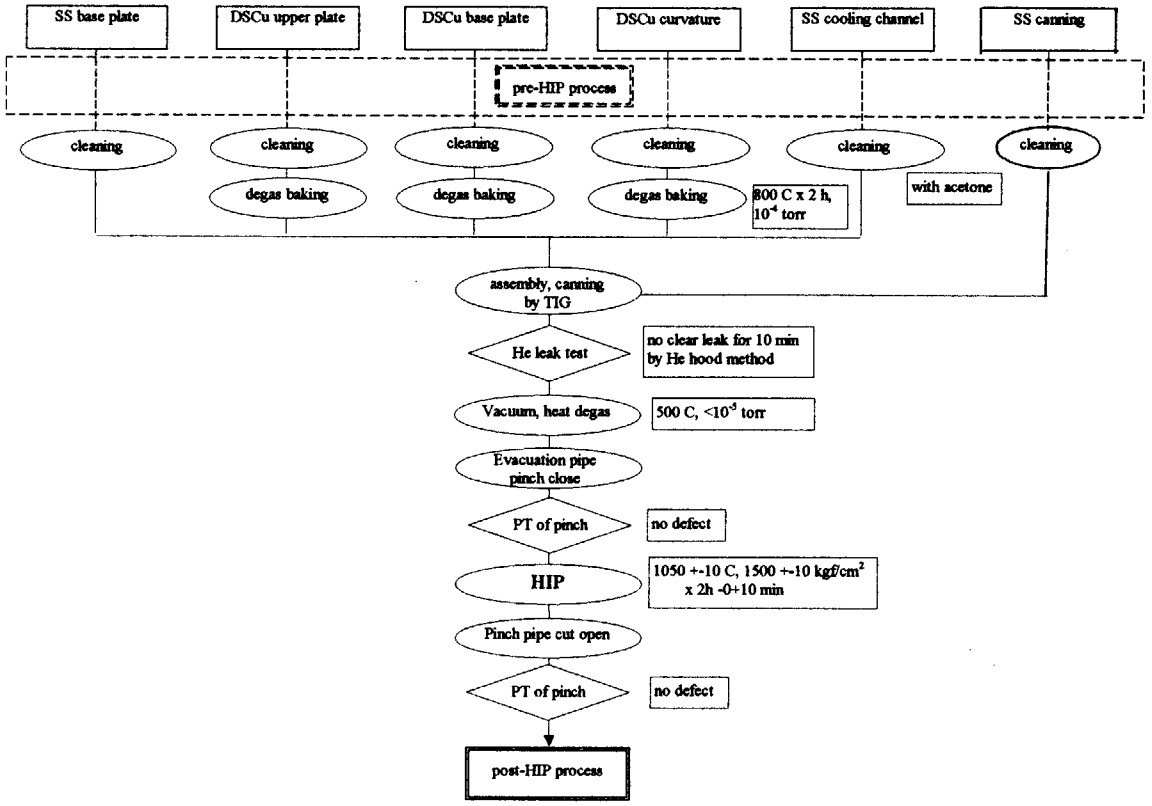

Fig. 1.2.1-4 Fabrication procedure of HIP process of DSCu/SS of Be armored first wall mockup

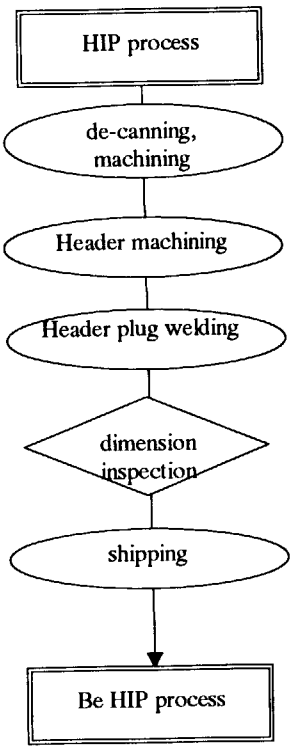

Fig. 1.2.1-5 Fabrication procedure of post-HIP process of DSCu/SS of Be armored first wall mockup

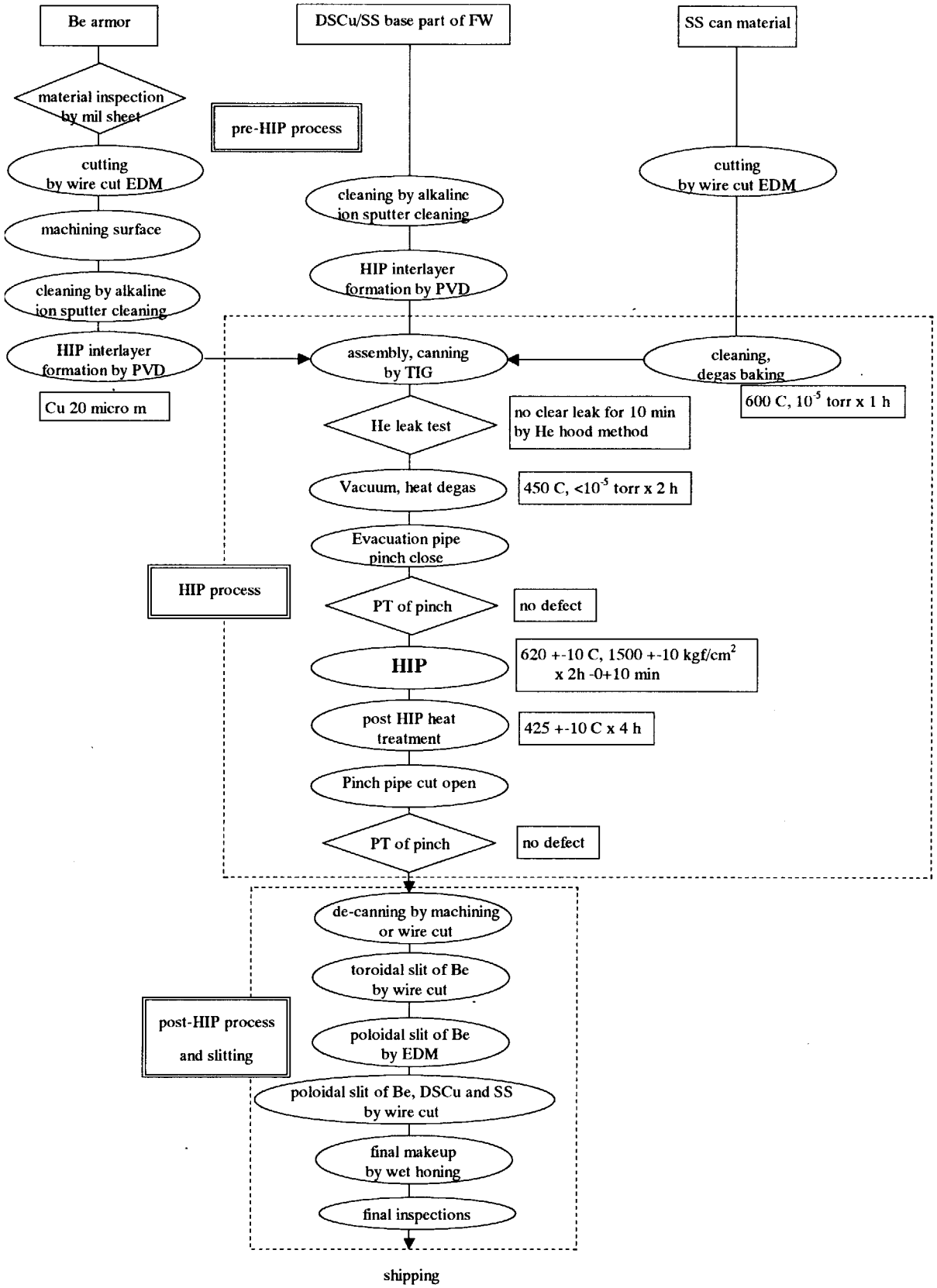

Fig. 1.2.1-6 Fabrication procedure of Be HIP and final makeup of Be armored first wall mockup

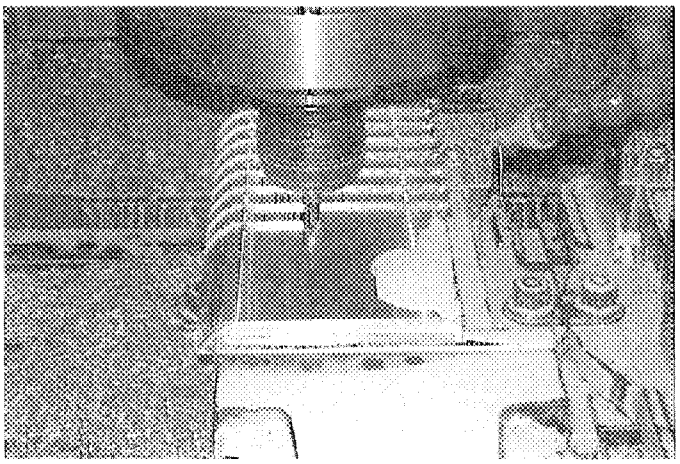

Fig. 1.2.2-1 Machining of DSCu heat sink plate for preparing HIP process of SS cooling channels

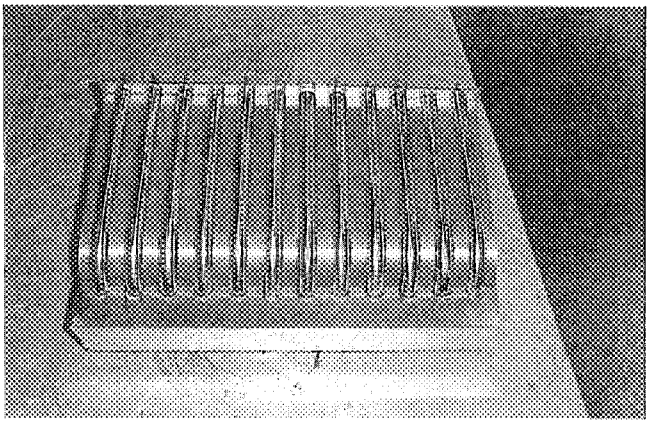

Fig. 1.2.2-2 Assembly of SS backing plate, DSCu heat sink plate and SS cooling channel tubes before HIP process

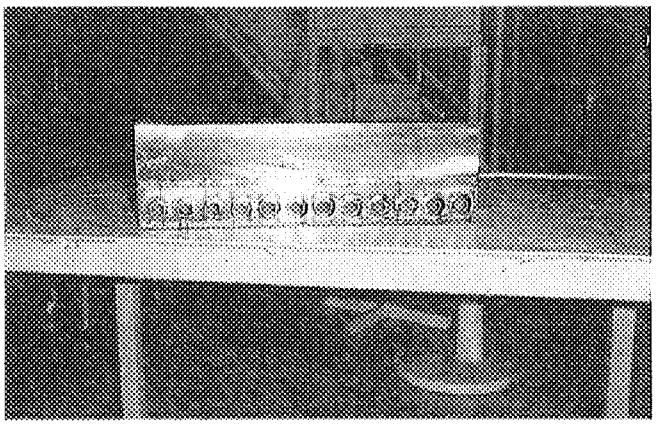

Fig. 1.2.2-3 Canning of DSCu/SS HIP process

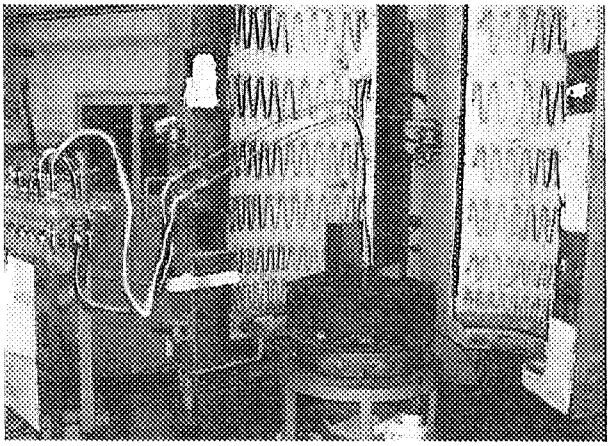

Fig. 1.2.2-4 Set up of HIP furnace

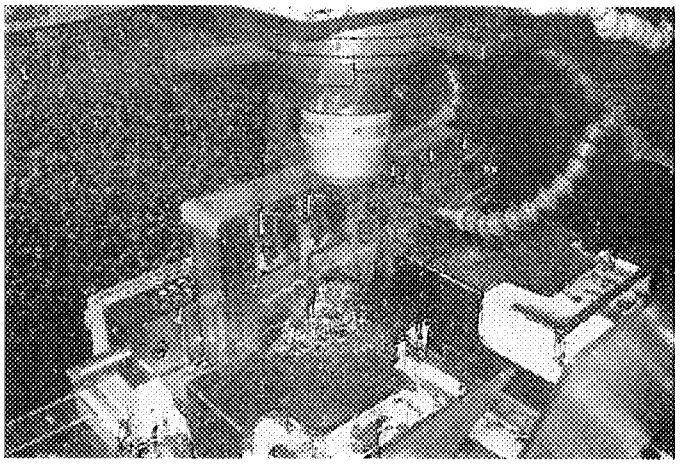

Fig. 1.2.2-5 Pealing HIP cannning

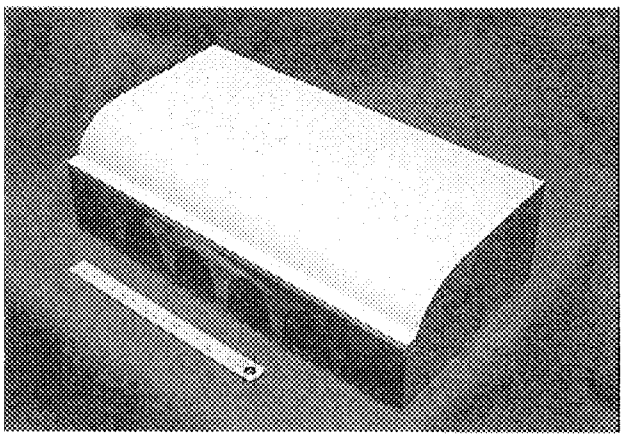

Fig. 1.2.2-6 First wall panel basement (HIP bonded SS basement and Cu alloy heat sink) prepared for feasibility study of Be armor joining technique on real scale width with Cu interlayer

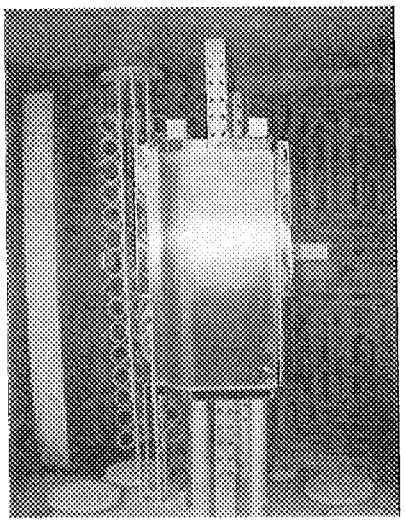

Fig. 1.2.2-7 HIP interlayer, OFCu, coating by PVD

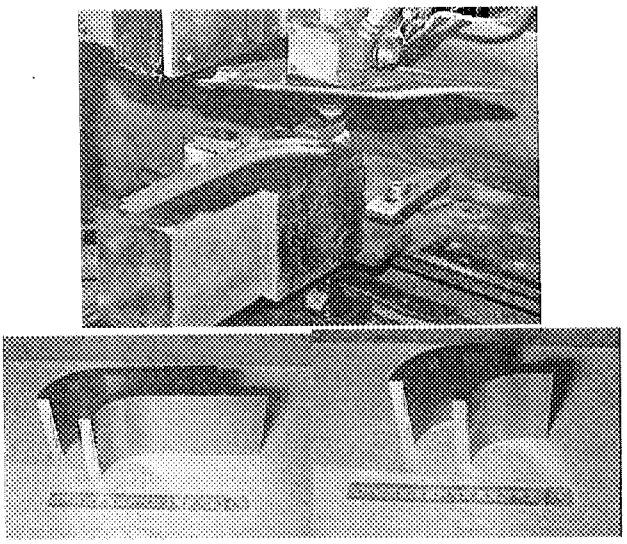

Fig. 1.2.2-8 Machining Be material block to form Be armor tiles

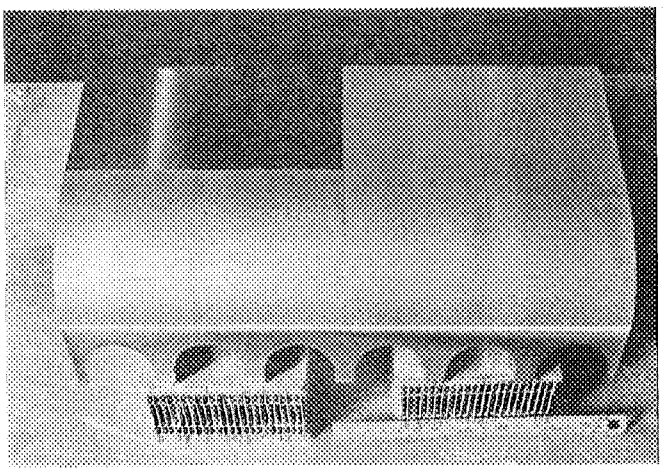

Fig. 1.2.2-9 Set up of Be pre-machined tiles on the Cu alloy heat sink

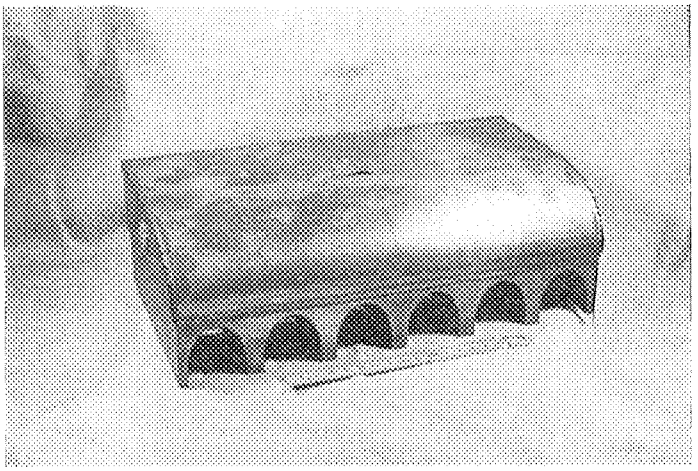

Fig. 1.2.2-10 Welded canning for Be HIP joining process

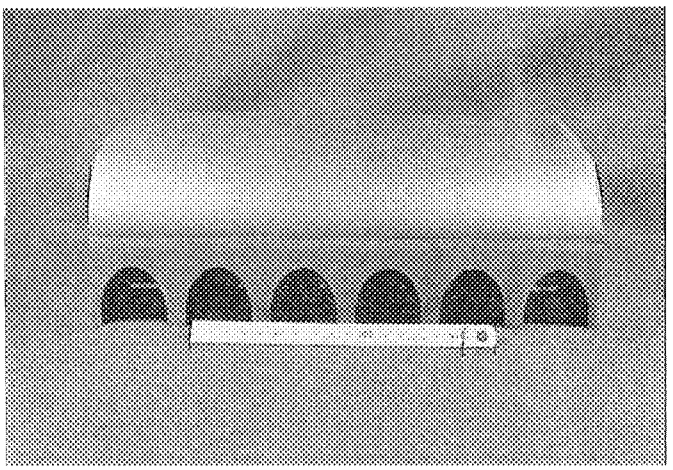

Fig. 1.2.2-11 Be armored FW mock after HIP decanning before slitting

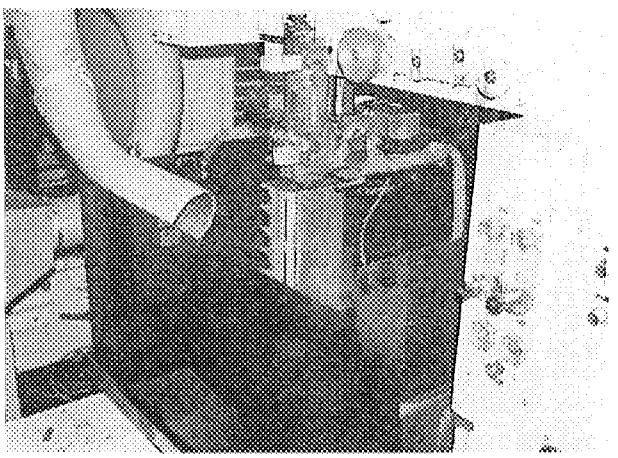

Fig. 1.2.2-12 Slit forming by wire sew

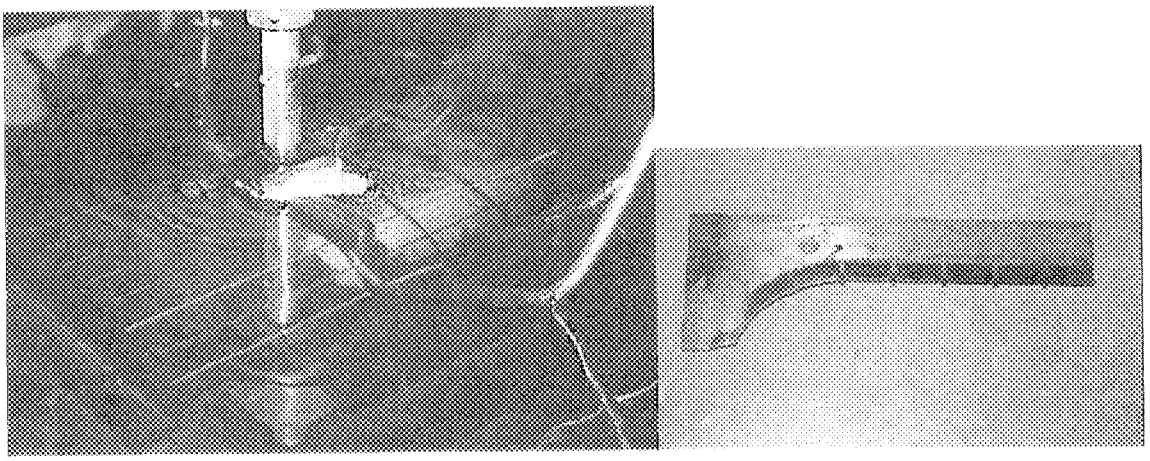

Fig. 1.2.2-13 Slit forming by EDM and used electrode element

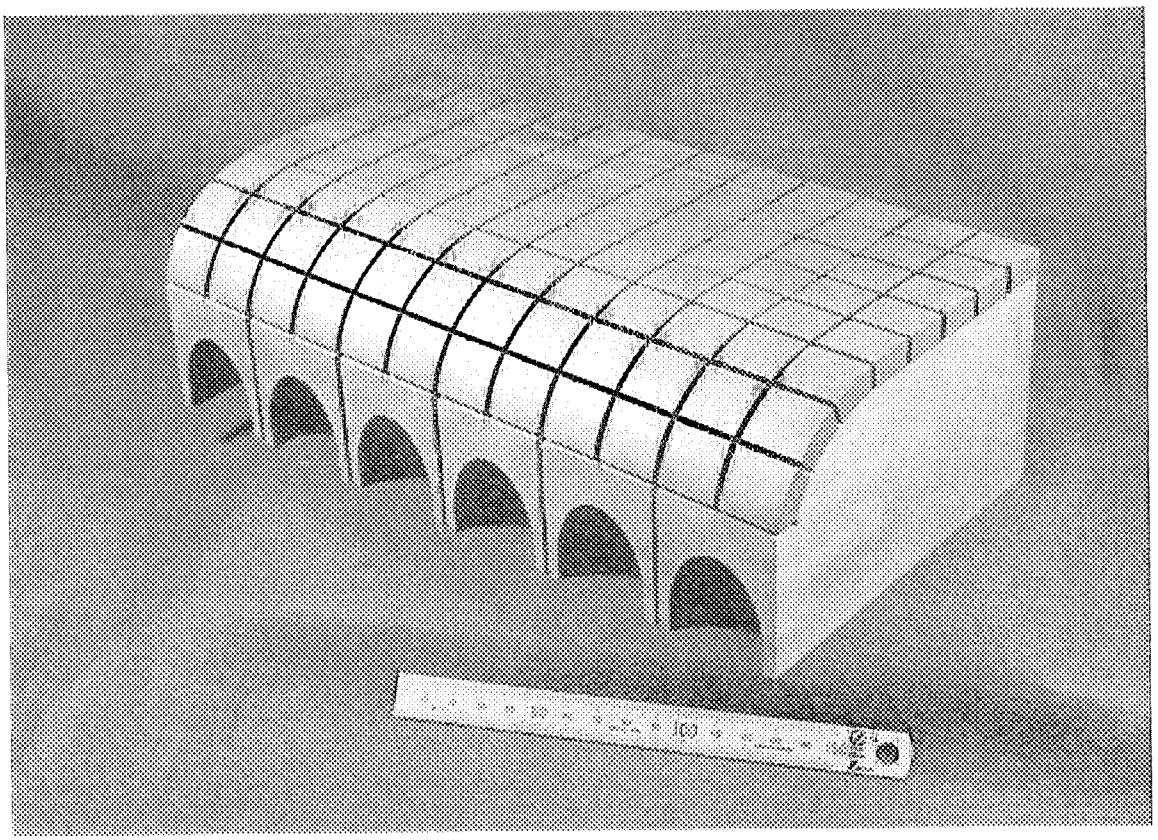

Fig. 1.2.2-14 Final product of Be armored FW mock up after slitting and honing

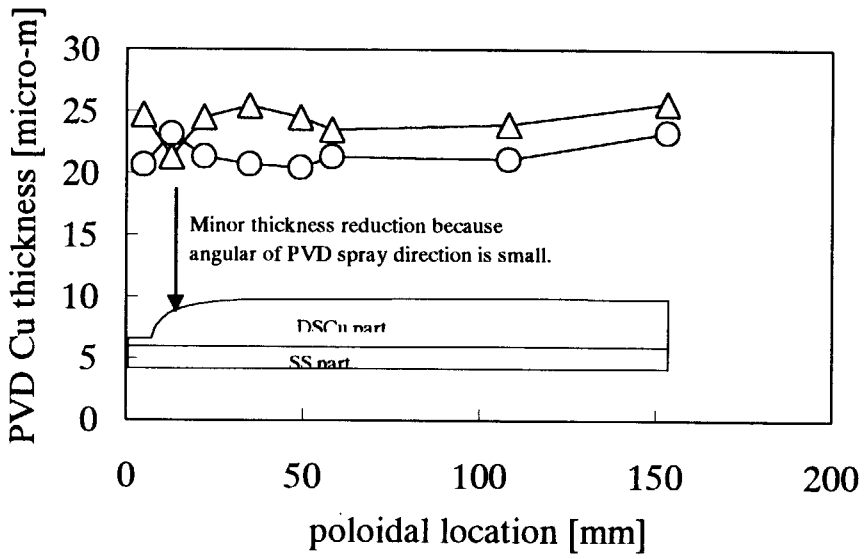

Fig. 1.2.3-1 Measurement result of PVD Cu interlayer thickness in poloidal direction

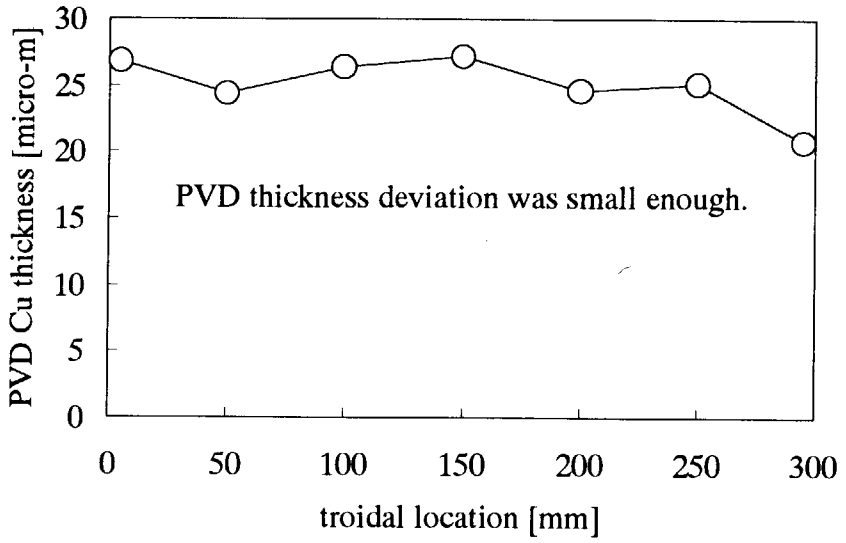

Fig. 1.2.3-2 Measurement result of PVD Cu interlayer thickness in toroidal direction

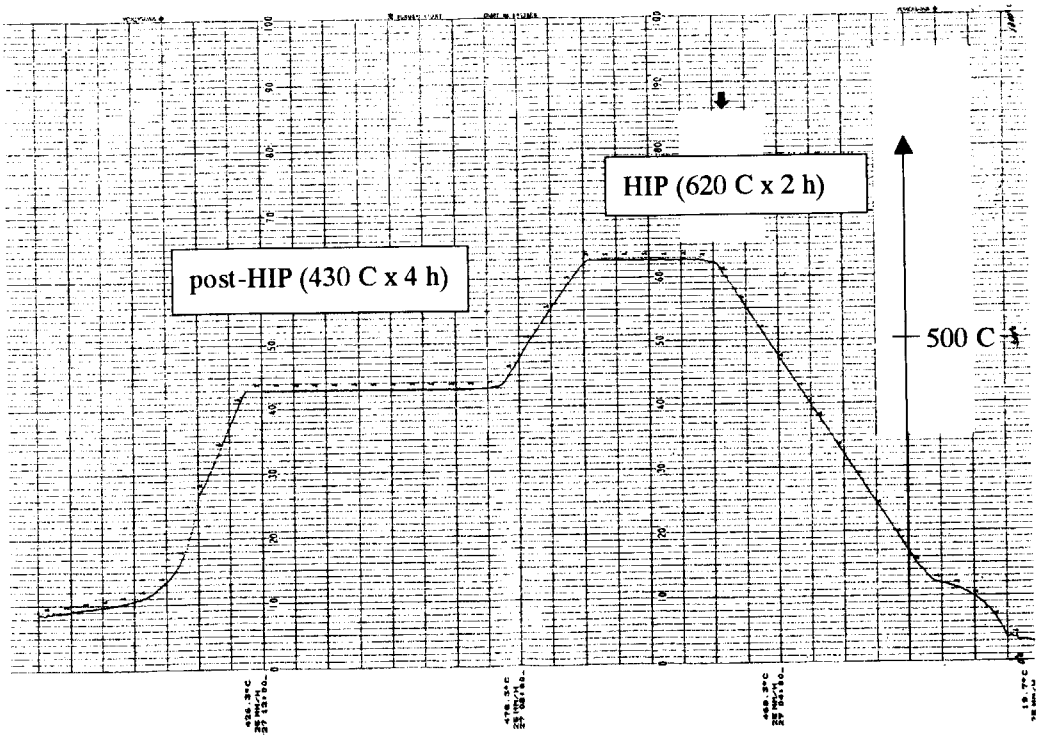

Fig. 1.2.3-3 Temperature history in HIP process

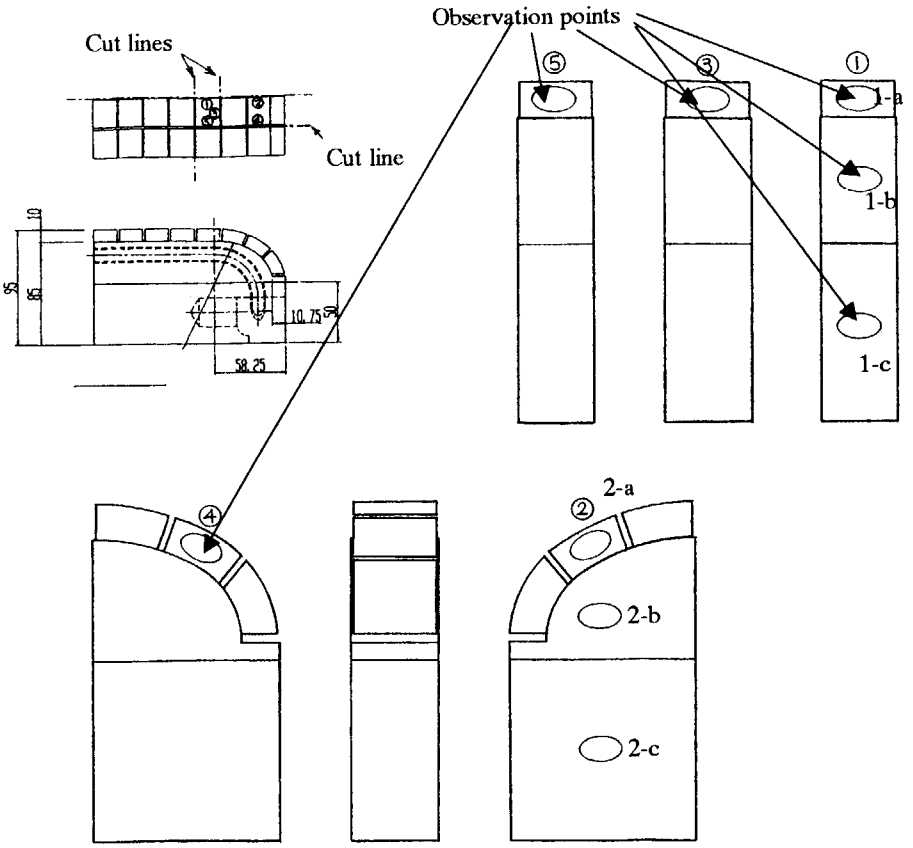

Fig. 1.2.3-4 Observation location of slit surface roughness

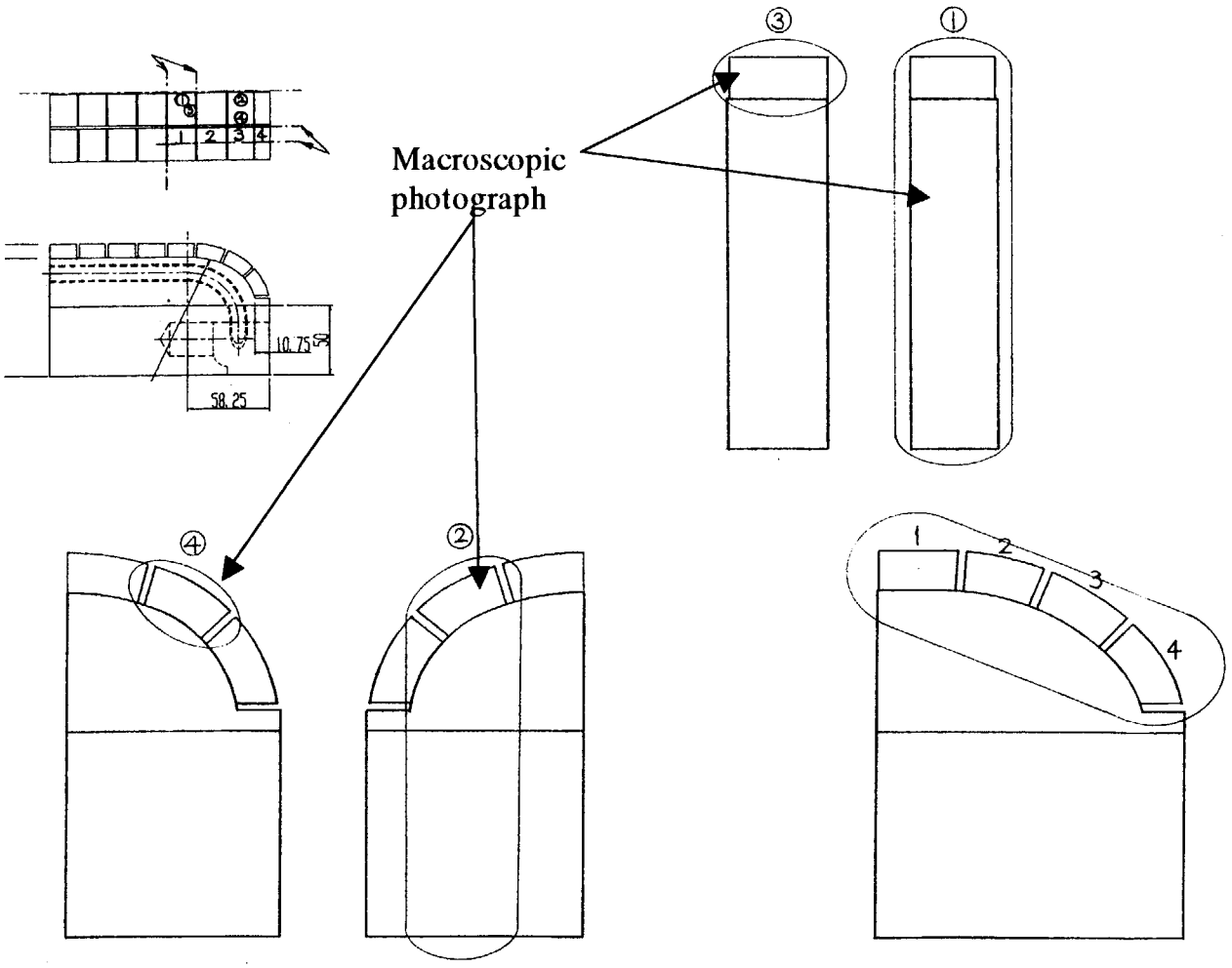

Fig. 1.2.3-5 Location of macroscopic photographs.

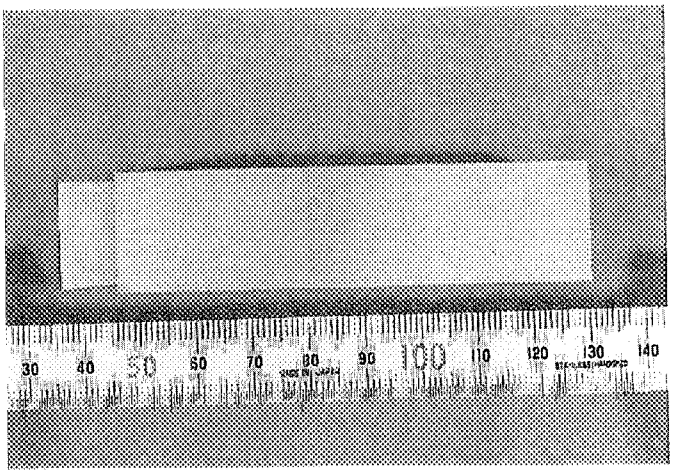

(a)

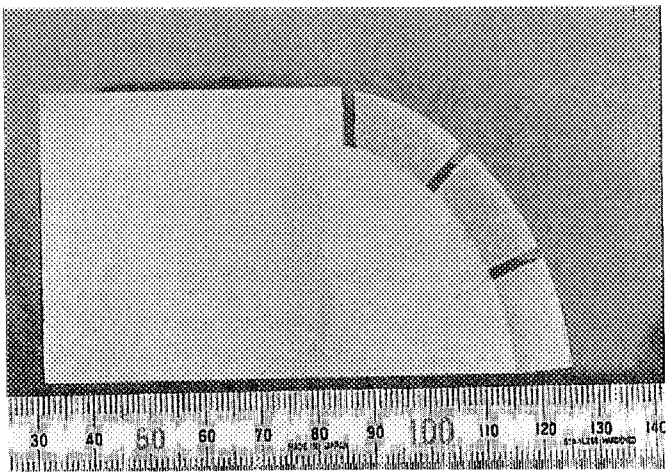

(b)

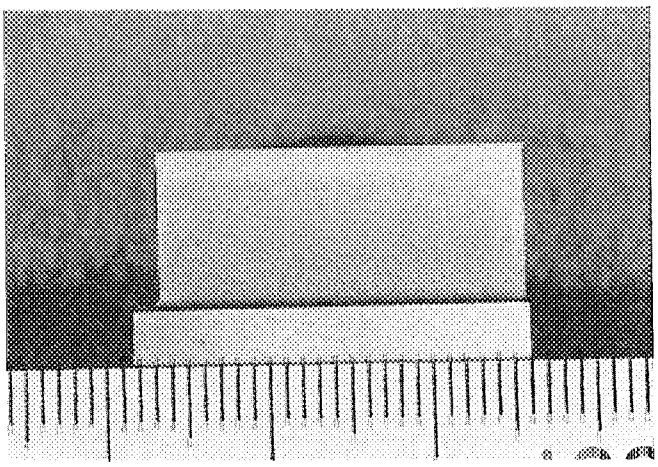

(c)

Fig. 1.2.3-6(a), (b), (c) Macroscopic photograph of No1, 2 and 3 location

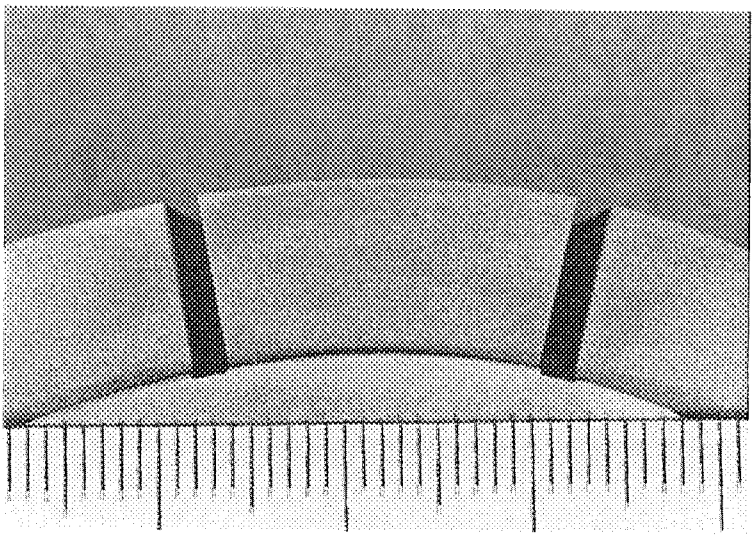

(d)

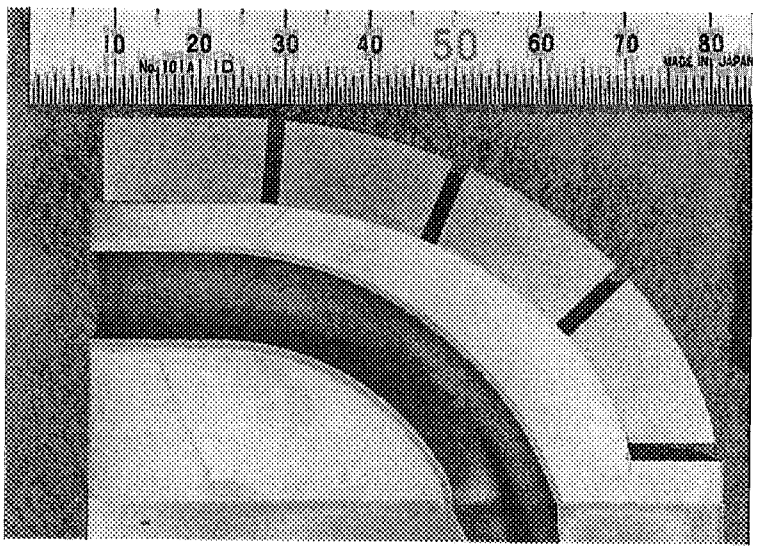

(e)

Fig. 1.2.3-6(d), (e) Macroscopic photograph of No 4 and 5 location

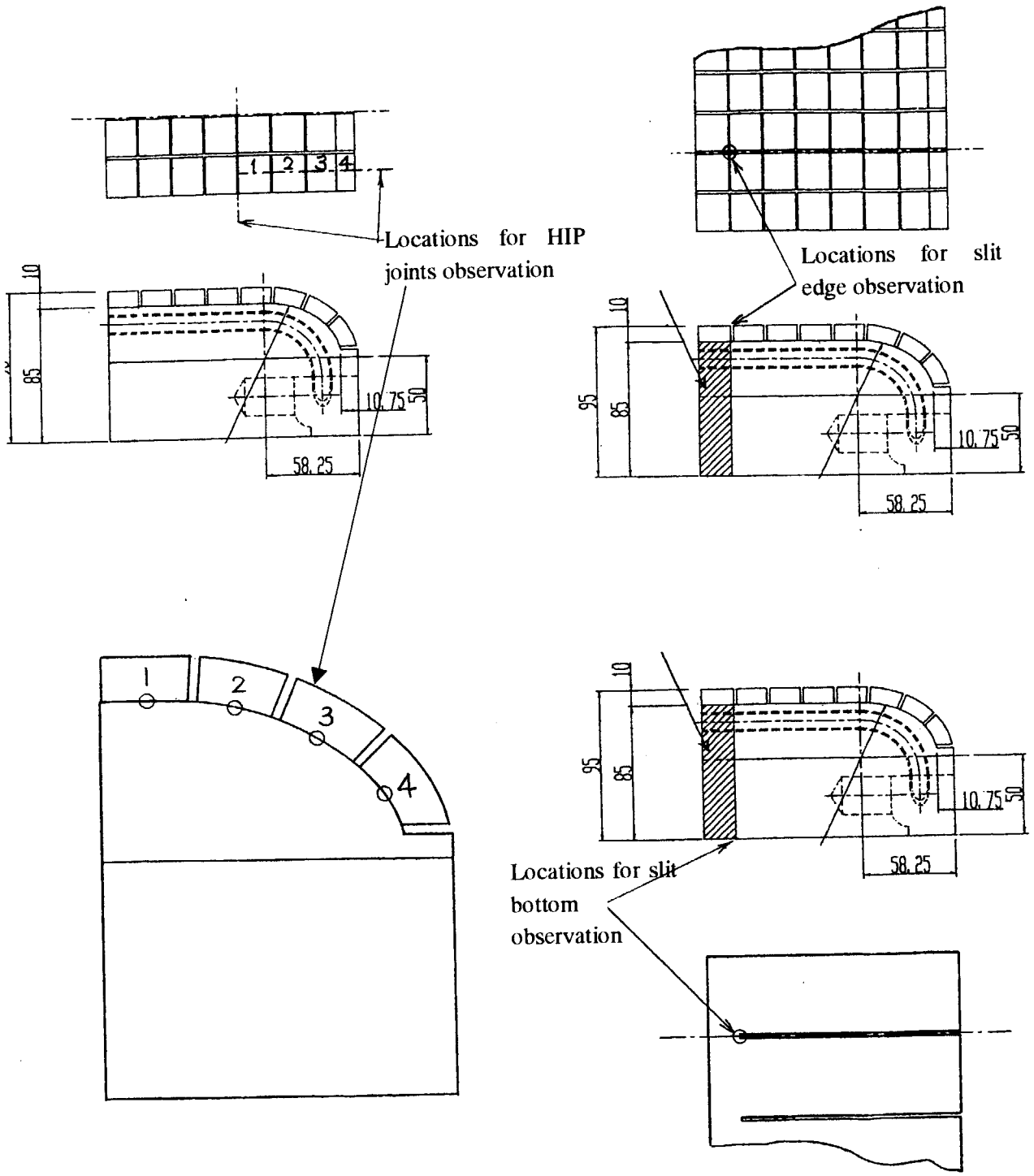

Fig. 1.2.3-7 Locations for optical microscopic observation of Be/DSCu HIP joints and slit

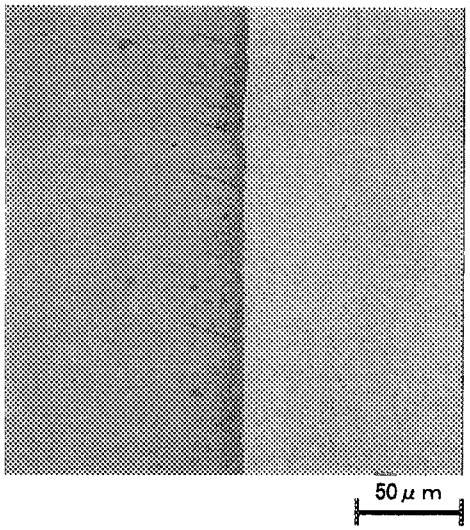

Location 1

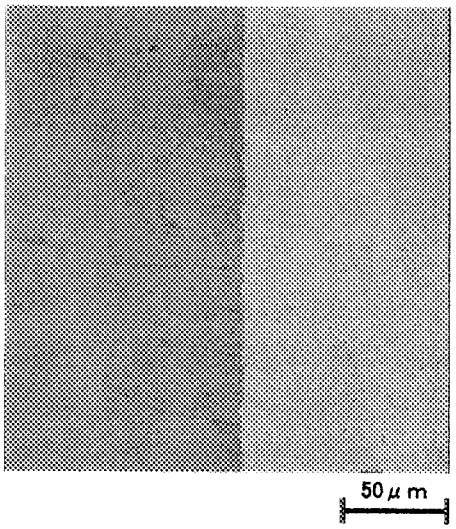

Location2

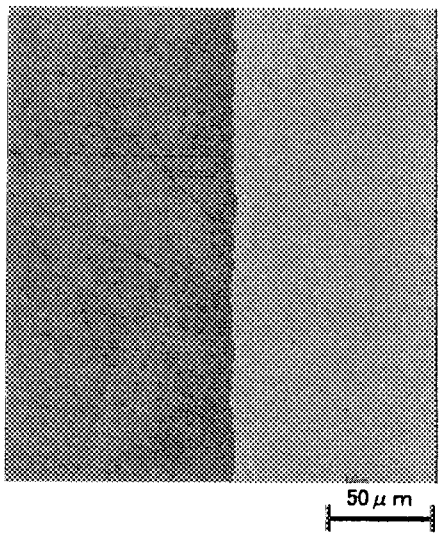

Location 3

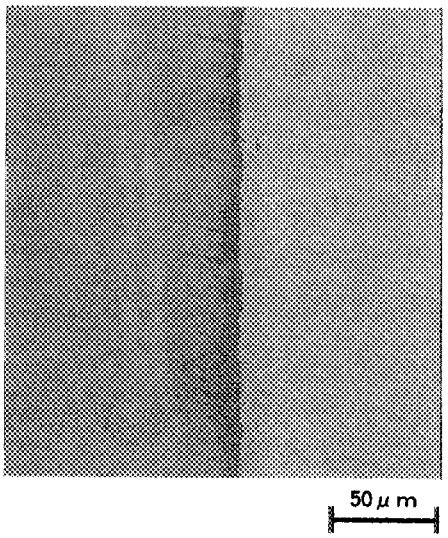

Location 4

Fig. 1.2.3-8 (a) Optical microscopic photograph of representative Be/DSCu HIP joints at location 1, 2, 3 and 4

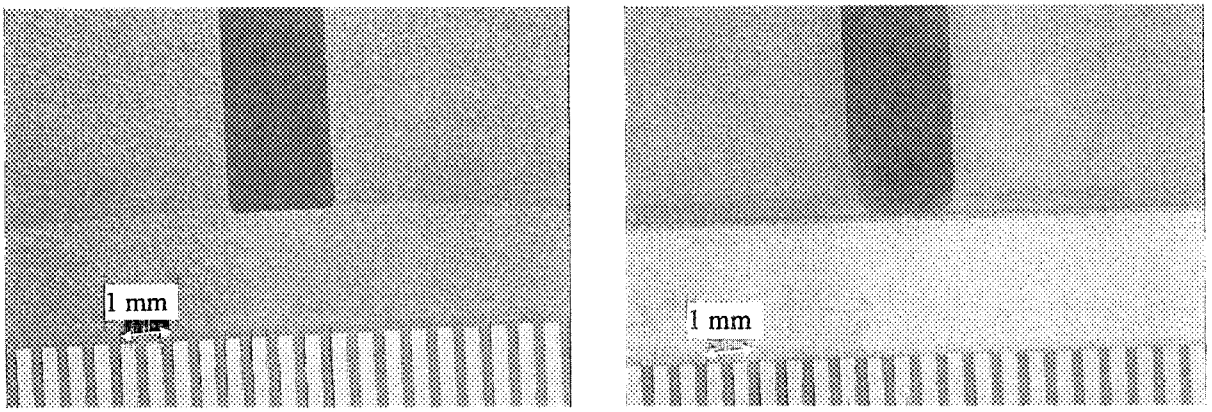

Fig. 1.2.3-8 (b) Optical microscopic photograph of penetration slit bottom (SS) and Be slit

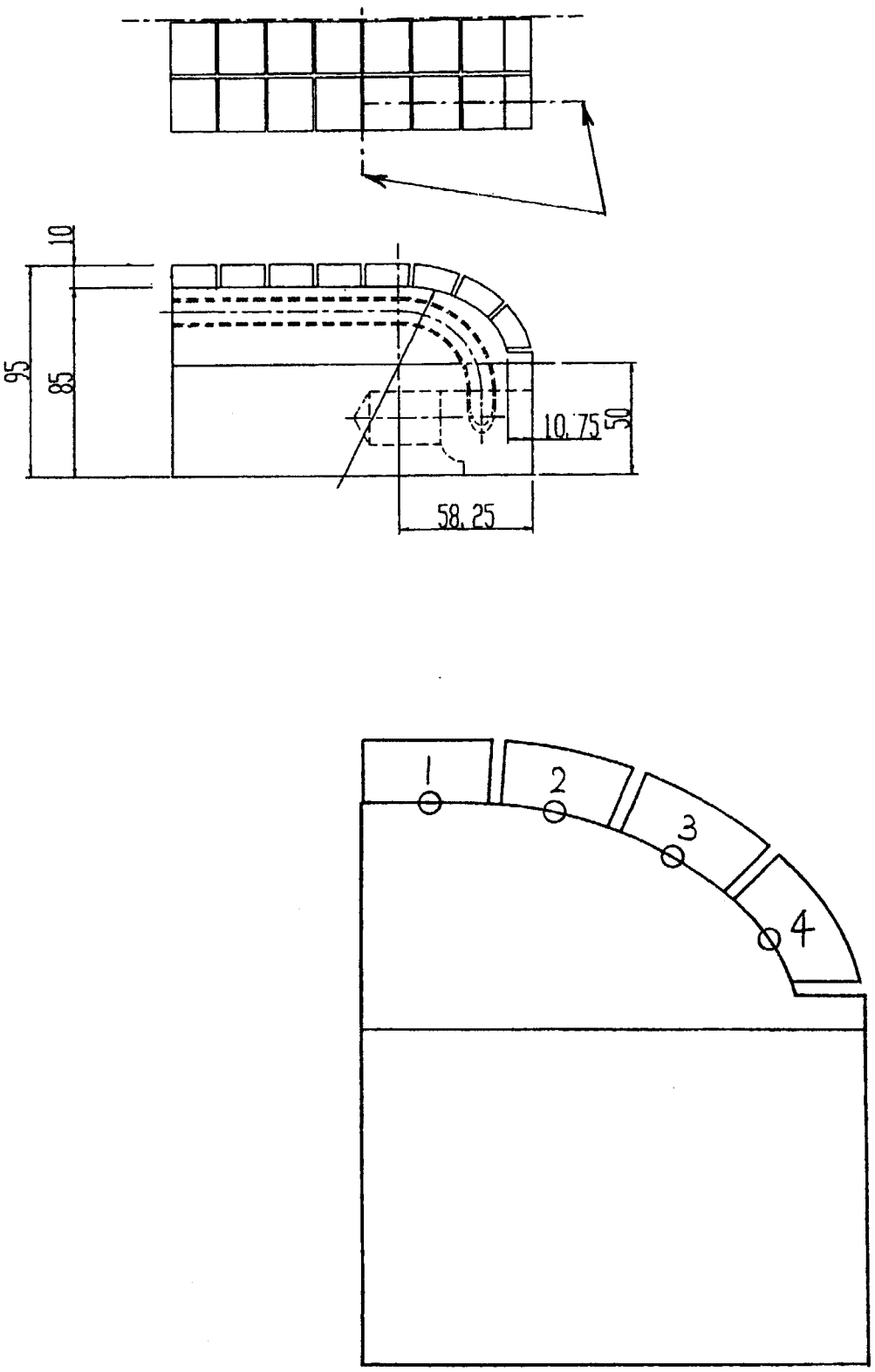

Fig. 1.2.3-9 Locations for SEM and EPMA observation

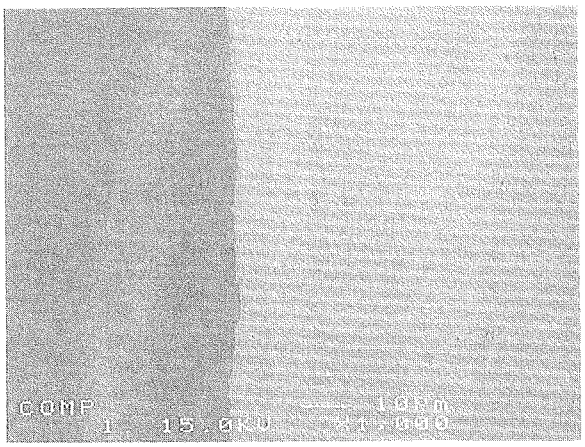

Location 1

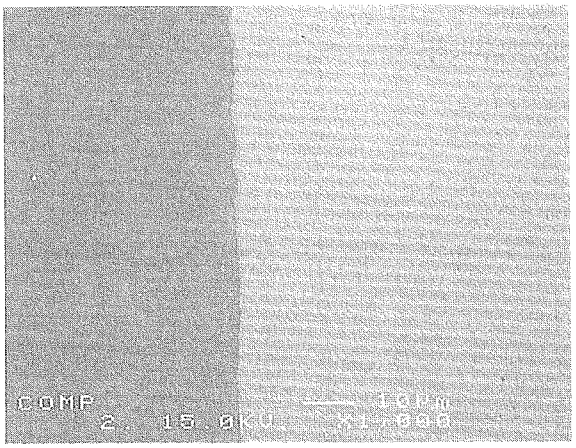

Location 2

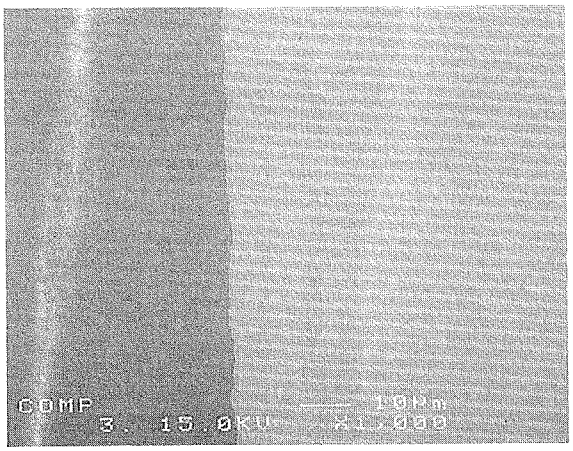

Location 3

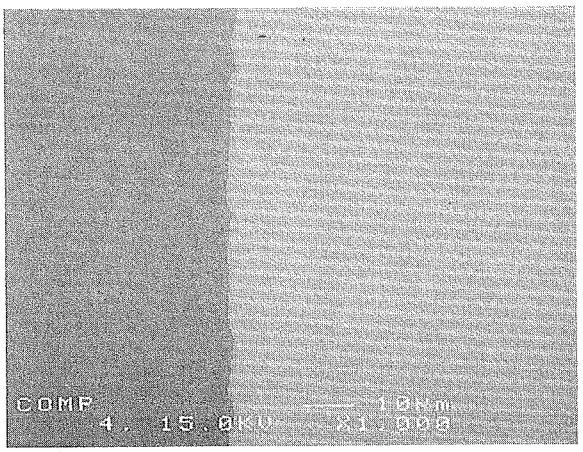

Location4

Fig. 1.2.3-10 (a) SEM observation of Location 1,2 3 and 4

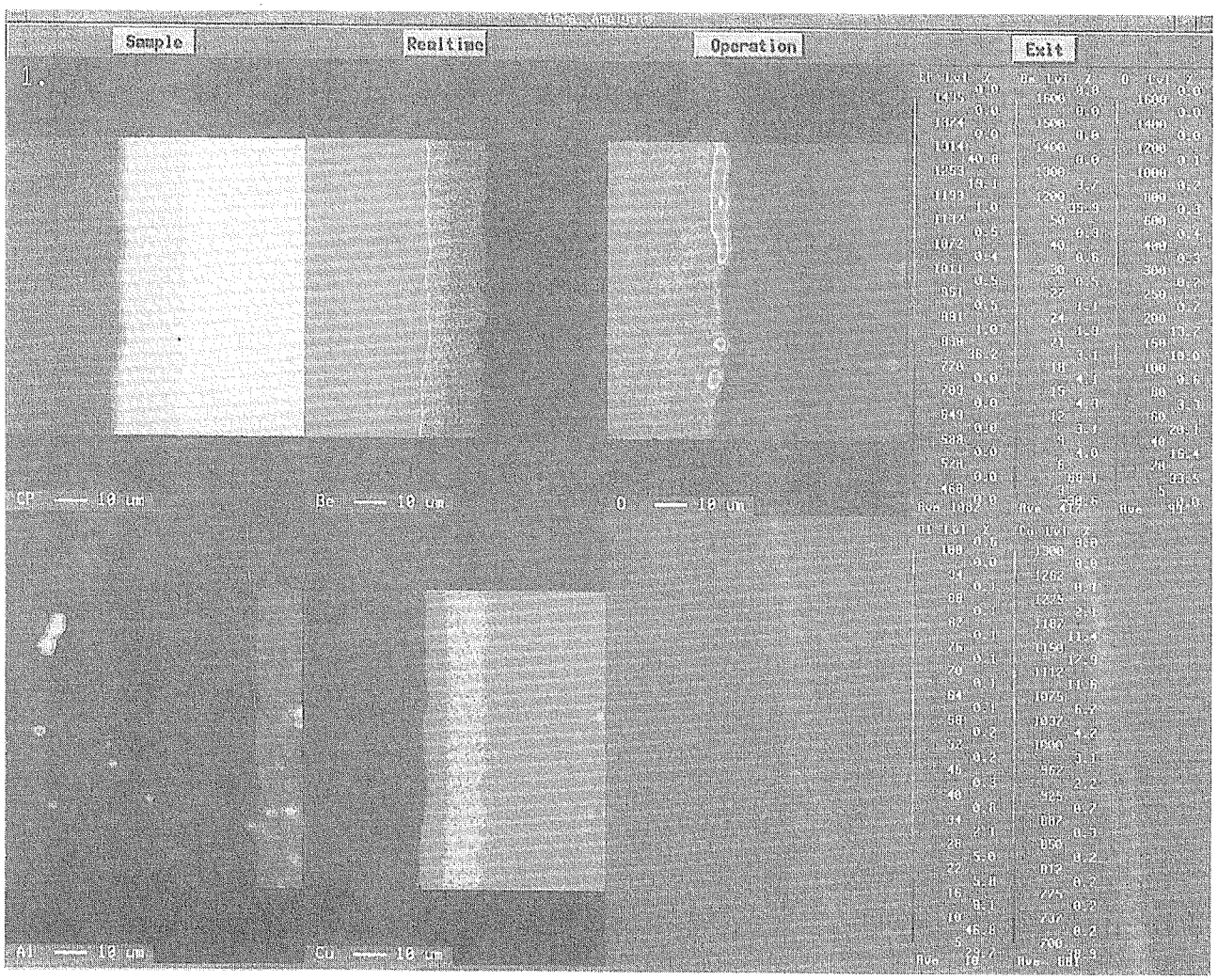

Fig. 1.2.3-10 (b-1) SEM image and EPMA analysis result distribution images for Be, O and Al and Cu at Location 1.

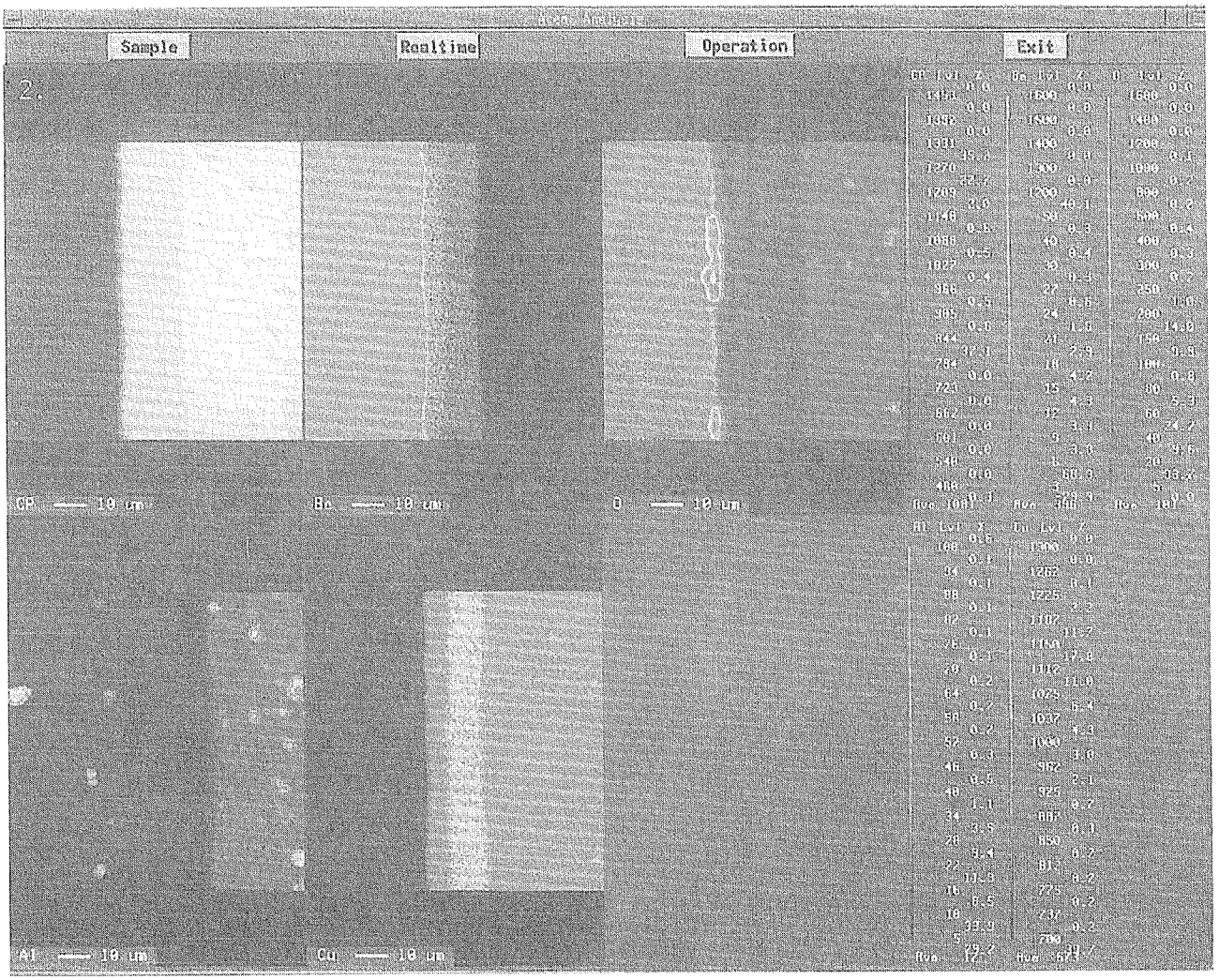

Fig. 1.2.3-10 (b-2) SEM image and EPMA analysis result distribution images for Be, O and Al and Cu at Location 2.

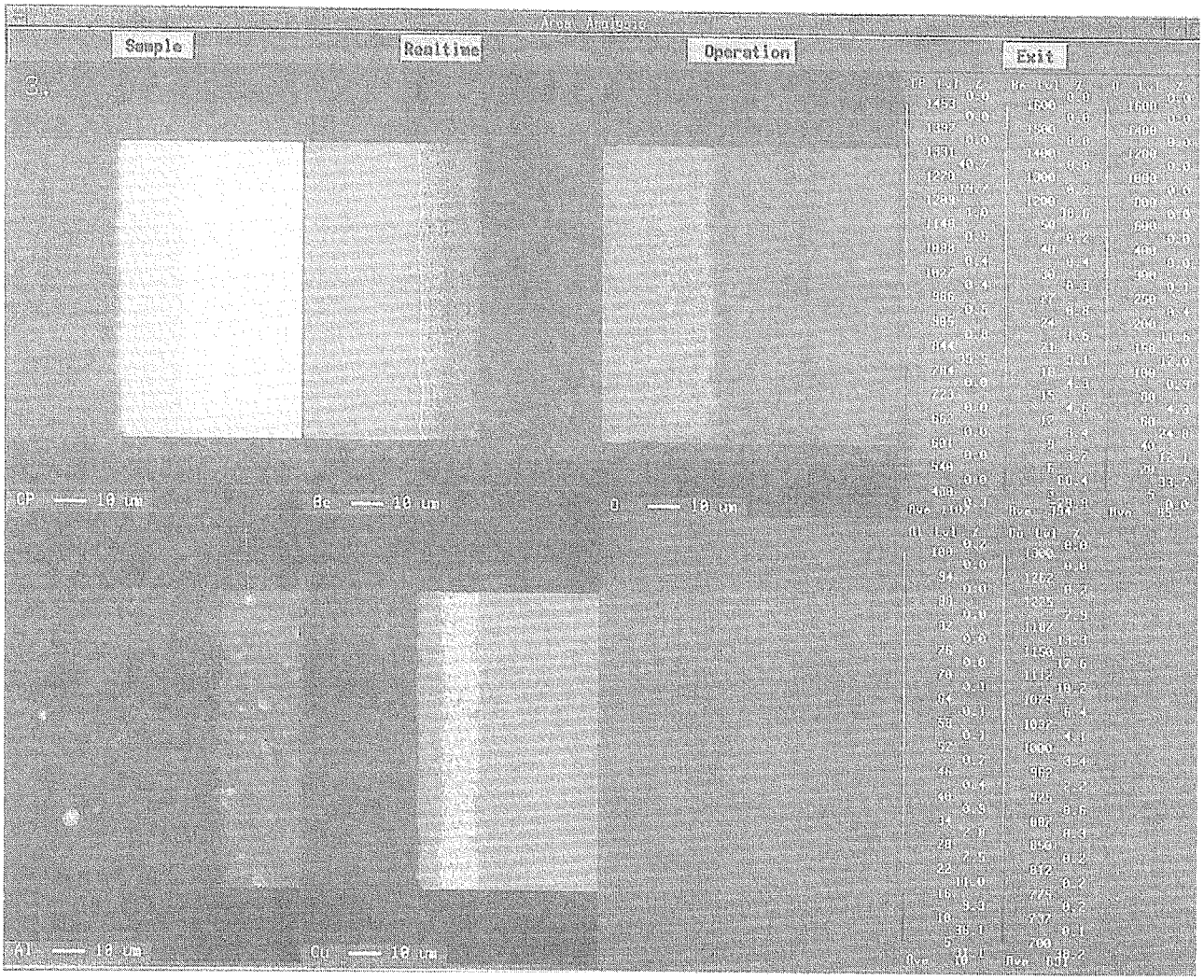

Fig. 1.2.3-10 (b-3) SEM image and EPMA analysis result distribution images for Be, O and Al and Cu at Location 3.

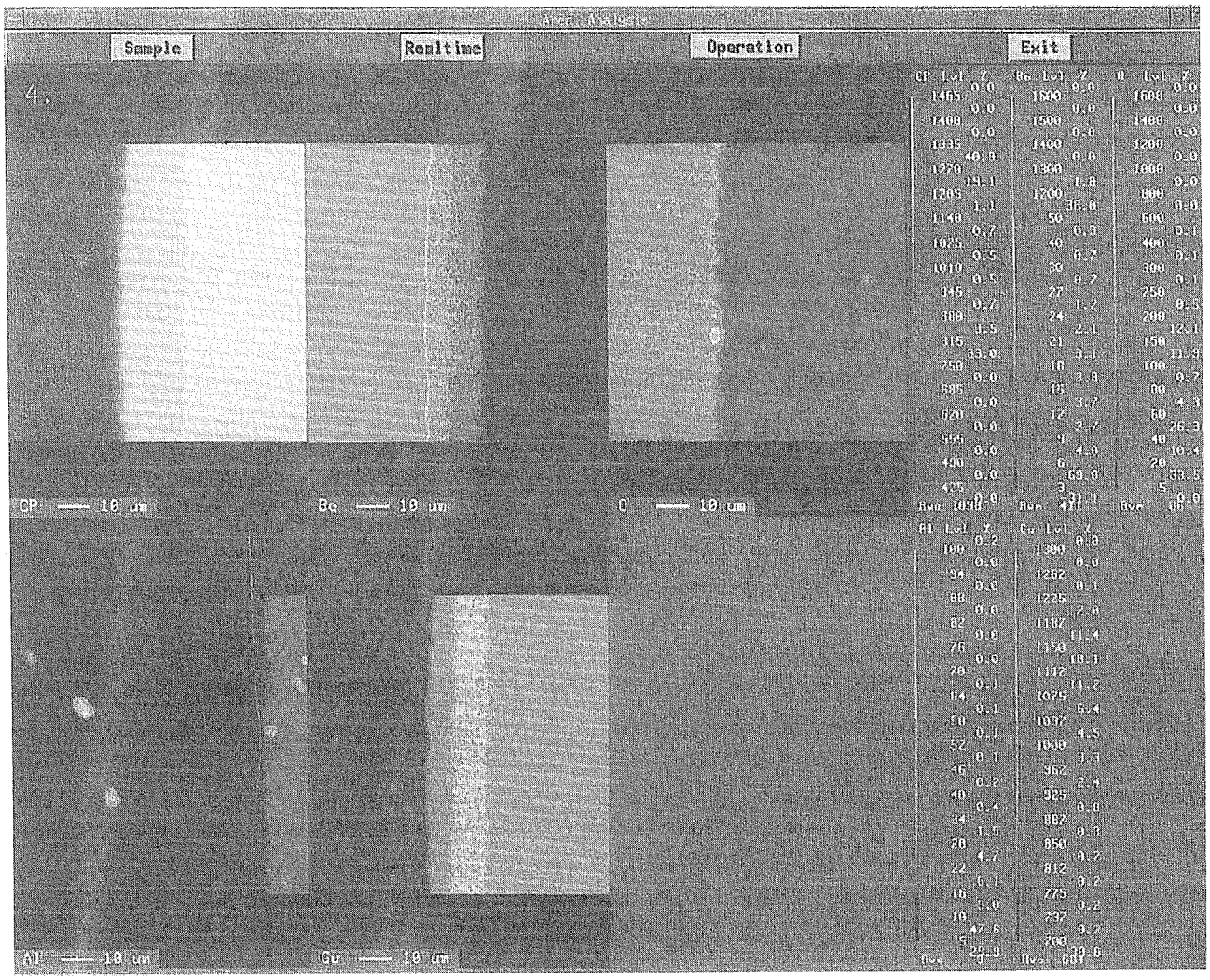

Fig. 1.2.3-10 (b-4) SEM image and EPMA analysis result distribution images for Be, O and Al and Cu at Location 4.

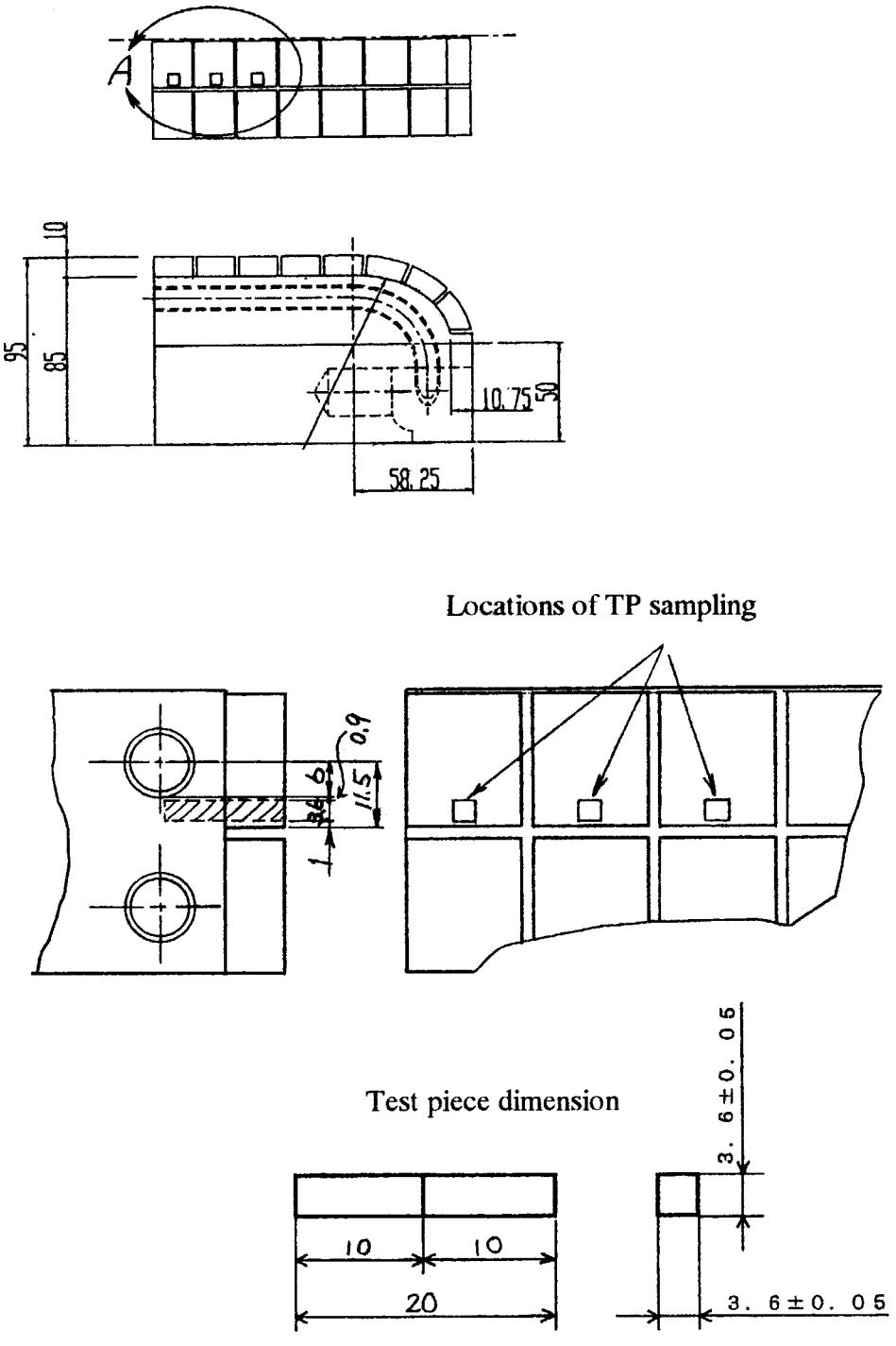

Fig. 1.2.3-11 Locations of test pieces sampling and dimension of test piece.

3.1.3 1/2 Poloidal Channel Shield Block Fabrication

3.1.3.1 Design of 1/2 Poloidal Channel Shield Block Model

Based on the detailed design of poloidal channel shield block shown in Fig. 1.1-3, the rough breakdown of the fabrication steps are summarized in Fig. 1.1-8. Further detailed fabrication procedure study resulted that the major critical fabrication processes are cleared by fabrication of 1/2 shield block Figure 1.3.1-1 shows the configuration of the 1/2 scale poloidal channel shield block model.

3.1.3.2 Fabrication Procedure

The detailed procedure of the fabrication of the mockup in Fig. 1.3.1-1 was shown in Fig. 1.3.2-1 (1) to (15). The steps are listed as follows.

(1) Slit grooving by water jet method
(2) Coarse machining of outer surface
(3) Shaping of support leg hole by wire cut EDM
(4) Drilling of toroidal headers
(5) Drilling of poloidal channels
(6) Drilling of front access holes
(7) Machining outer surface and prepare EB welding of blocks
(8) TIG welding of FW-SB coolant connectors and plugs of toroidal header holes
(9) Machining of upper headers
(10) Machining of lower header
(11) EB welding of two 1/4 shield blocks
(12) Drilling of slit ends at EB welding ends
(13) Shaping and finish machining of header cap plates
(14) TIG welding of header cap plates
(15) TIG welding of plugs of toroidal header holes

Critical fabrication steps are (1), (11) and (14). Preliminary R&D were performed to ensure the feasibility of these 3 critical fabrication steps.

3.1.3.3 Preliminary R&D for Fabrication

(a) Slit grooving by water jet method

With respect to "(1) Slit grooving by water jet method", the previous R&D demonstrated that the water jet method is the inexpensive technique for non-penetrating slit grooving such as that of shield block. In case of the water jet method, stopper of water jet is necessary. In the previous R&D, 30 mm diameter stopping holes was used to set water jet protecting material for obtaining sound slit of 200 mm depth. Also, the progress speed of the jet was optimized. In this work, the possibility of the 20 mm diameter stopping holes are researched by using real scale 1/4 shield blocks. Points of research is the selection of water jet protecting material. The criteria of selection is the deviation and roughness of the grooving surface near the bottom of the slit.

Table 1.3.3-1 summarizes the water jet condition. All condition was optimized by teh previous R&D. Table 1.3.3-2 summarizes the materials used in this test. Table 1.3.3-3 summarizes the combination of the stopping materials in this test. The selection was done by the measurement of slit width dimension and deviation height. The measurement of the deviation was performed after cutting the grooved block into 2 pieces. In the tests, two different kinds of shape of the stopping stick is also tested. One is the reversed rail-shaped stick and the other is the L shape stick. Both shape is expected to relax the splash of the water jet and give the outlet path for the water.

Figure 1.3.3-1 (1) to (7) shows the photographs of grooving surface and stopping materials

corresponding to case (1) to (7). The observation showed that there are two types of slit shape deviation, one is the widening of the slit width near by the bottom stopper hole (=L1), another is the failure of the stopping hole (=L2). The measured values of L1 and L2 are listed in Table 1.3.3-4. As can be seen from the table, case 7 was the best. By the observation of Fig. 1.3.3-1 (1) to (7), simple stick stoppers caused the strong splash of the water jet. The splash seemed to made deviation of the shape of the bottom part of slit. Also, case (6), which tried the reversed rail shape, made splash of the water jet inside the stopping hole and resulted the failure of the stopping hole itself. Case (7), which applied two L shape sticks for the upper stopping material, seemed to have given smooth path for water jet outlet and resulted relatively sound slit shape even at the bottom part. As can be seen from the photograph in Fig. 1.3.3-1, case 7 gave the most sound slit surface. Thus, stopping material and shape of the stopping stick was selected as in case 7.

(b) EB welding of two 1/4 shield block

Optimization of EB welder operation condition and minimum slit width

In the Electron Beam welding process for joining multiple 1/4 shield blocks, it is required that 120 mm of the welding thickness with sound bead and minimum deformation. The welding also requires the EB injection through narrow slit from the plasma side, too. Thus, the selected welding method is two path method. Front side EB is required to pass through narrow slit with high convergence ability of the beam. On the other hand, the EB from rear side is required the deep melting ability. Thus, high voltage type machine (Schteigerwald, 15kW output) was selected for front side EB and the low voltage type (MELCO 30kW) was selected for rear side EB. Table 1.3.3-5 summarizes the specification of the EB welder. Points to be optimized in the preliminary R&D are convergence lens current for both EB welders and minimum slit width which avoids failure of the slit surface for front EB welder. With respect to the tested slit width, 4 mm, 6 mm and 8 mm are applied. Table 1.3.3-6 summarizes the welder conditions and convergence lens currents applied in this tests. Figure 1.3.3-2 (a) and (b) show the test pieces used in the bead depth test by the low voltage type welder and the slit width tests by high voltage welder. Figure 1.3.3-3 and 1.3.3-4 show the macroscopic photograph of the cross sectional view of the welding bead generated by high voltage type welder tests and low voltage type welder, respectively. Surface width and the penetration depth of the welding bead were measured to select the optimized condition. Table 1.3.3-7 shows the measured results. As can be seen from Table 1.3.3-7, case 3 was the best condition for high voltage type welder and case 3 for low voltage type welder. Figure 1.3.3-5 shows the test result observation of the slit width optimization tests. In this figure, the cases of 4mm and 6 mm width are shown. As can be seen from this figure, both of 4 and 6 mm slit width was not sufficient because the melting failure was observed at the front part of the slit. In case of the slit width of 8 mm, no remarkable melting was observed on slit surface as seen in Fig. 1.3.3-6. Thus, it was concluded that 8 mm width is necessary as the slit width between 1/4 shield blocks.

Effect of the EB welding over TIG welding of the toroidal header plugs

Another issues to be confirmed is if EB welding over TIG welding of the toroidal header plugs causes any failure of TIG welding line of the plugs, because the order of fabrication step for EB welding to join shield blocks should always be after the plugging of the toroidal header is completed. For clarifying this issue, trial welding tests which simulate EB welding over 24 diameter plug and 45 mm diameter plug welded to the SS plates by TIG welding were performed. EB welding was performed exactly the same condition and manner as optimized and expected in the real fabrication process by using both of the High Voltage Type and Low Voltage Type EB welder from both side of 120 mm thickness plates which have the welded plugs of 24 mm and 45 mm diameters. Figure 1.3.3-7 (a) and (b) shows the test piece sketches for the tests of 45 mm and

24 mm diameter plugs, respectively. Figure 1.3.3-8 shows the outer surface of both side of welding line, front side by high voltage welder in top picture and rear side by low voltage welder in bottom picture. Figure 1.3.3-9 shows the cross-sectional observation of the welded plugs (24 mm diameter left, 45 mm diameter right) over welded by EB welding. As can be seen from this figure, there is no remarkable failure on both welding lines. This tests made confirmation of the EB welding technique for joining 1/4 shield blocks.

(c) TIG welding of header cap plates

The thick ness of the header plug is selected to withstand high pressure of coolant water (15 MPa). Thus, the TIG welding of the plug is one of the issues to be tested before fabrication. As the preliminary confirmation test, the simulating header and header cap plate were welded by TIG. After welding, sampling of TP were performed. Figure 1.3.3-10 shows the location of the sampling points. Typical picture of the TP is shown in Fig 1.3.3-11 by TP #1. There is a tendency that the header cap plate sinks during TIG welding, because of its heavy weight.

3.1.3.4 Fabrication of 1/2 poloidal channel shield block

After obtaining sound results of preliminary R&D explained in the previous section, the fabrication was carried out. Figure 1.3.4-1 to 1.3.4-6 shows major important fabrication processes of the 1/2 poloidal shield block. The followings are the corresponding fabrication steps described in section 1.3.2.

Fig. 1.3.4-1	Slit grooving by water jet method	step (1)
Fig. 1.3.4-2	Slit grooving finish at the bottom of the slit and jet stopping holes	step (1)
Fig. 1.3.4-3	Set up of gun-drill for cooling channels	step (5)
Fig. 1.3.4-4	Appearance of the cooling channels and toroidal headers	step (5)
Fig. 1.3.4-5	Machining of the top and bottom headers	step (10)
Fig. 1.3.4-6	Preparation of EB welding of two 1/4 shield blocks	step (11)
Fig. 1.3.4-7	Appearance of the front part of the slit where the EB go through	step (11)
Fig. 1.3.4-8	Appearance of the rear part of the slit where the EB go through	step (11)
Fig. 1.3.4-9	Close up of the rear part of the slit where the EB go through	step (11)
Fig. 1.3.4-10	Set up for TIG welding of top and bottom header plates	step (14)
Fig. 1.3.4-11	Appearance after TIG welding of the top header plates	step (14)

3.1.3.5 Section Conclusions

The work performed in this chapter clarified major basic information necessary for fabrication of the shield block for the option B blanket module. Obtained information are as follows

(1) Slit grooving technique by water jet method
- grooving speed, nozle diameter
- jet stopper material and shape of the stopper rods

(2) EB welding of two 1/4 shield block
- Optimized EB welder operation condition and minimum slit width
- Effect of the EB welding over TIG welding of the toroidal header plugs

(3) TIG welding of header cap plates
- Shape of welding line
- Deformation after welding

All issues are common to the updated design of shield block which features radial cooling channel.

Table 1.3.3-1 Water jet condition

Parameter	Set value
Water pressure	3000 kgf/cm^2
Water nozzle diameter	0.33 mm
Abrasive nozzle	1.2 mm dia. x 70 mm
Abrasive material	Garnet #80
Flow rate of abrasive material	0.4 kg/min
Stand off length	2 mm
Jet progress speed	1 mm/min
Jet angular (nozzle/TP)	85 degree

Table 1.3.3-2 Materials used in the tests

Part	Material	Specification
Test block	SS	SS304 (100 x 40 x 240)
Jet sopping material	Super-Hard Steel KD10 by Barloy Co.Ltd.	HRA91, HB>940
	Alumina	HS97, HRA85.6
	High Cr Steel	HS70, HRA77
	High Carbon Steel	HS50, HRA69

Table 1.3.3-3 Combinations of the jet stopping materials

Case #	Combination of stopping materials and cross section	position
1	Soft Steel/ Super-Hard Steel, 9 mm square	simple stick, top/bottom
2	Super-Hard Steel / Alumina, 9 mm square	simple stick, top/bottom
3	Super-Hard Steel / High Cr Steel, 9 mm square	simple stick, top/bottom
4	Super-Hard Steel / High Carbon Steel, 9 mm square	simple stick, top/bottom
5	Super-Hard Steel / High Cr Steel / Super-Hard Steel, 2 mm, 6 mm, 12 mm thick x 9 mm width	simple stick, top/mid/bottom
6	Super-Hard Steel / Super-Hard Steel, 9 mm square top = 5 mm width grooved	top/bottom
7	Super-Hard Steel / Super-Hard Steel, top = 2 mm width L shape, bottom square	two top sticks / bottom

Table 1.3.3-4 Measurement results of the slit form deviation near bottom of slits

Case #	L1 [mm]	L2 [mm]
1	2	9
2	1.5	13
3	1	6
4	2	8
5	2	6
6	4	7
7	0.5	3

Table 1.3.3-5 Major specifications of the EB welder

	Front EB	Rear EB
Type	High voltage type	Low voltage type
Nominal output power	15 kW	30 kW
Maximum Acceleration Voltage	150 kV	70 kV
Max. Beam current	100 mA	429 mA

Table 1.3.3-6 Welder conditions in this tests

Case No	Accel Voltage	Beam current	Welding speed	Convergence lens current
High Voltage type (Front EB)				
1	150 kV	100 mA	180 mm/min	2060 mA
2	150 kV	100 mA	180 mm/min	2100 mA
3	150 kV	100 mA	180 mm/min	2140 mA
4	150 kV	100 mA	180 mm/min	2180 mA
5	150 kV	100 mA	180 mm/min	2220 mA
Low Voltage type (Rear EB)				
1	70 kV	350 mA	200 mm/min	800 mA
2	70 kV	350 mA	200 mm/min	820 mA
3	70 kV	350 mA	200 mm/min	825 mA
4	70 kV	350 mA	200 mm/min	830 mA
5	70 kV	350 mA	200 mm/min	840 mA

Table 1.3.3-7 Observed value of EB welding bead dimension

Case No	Bead depth	Bead surface width
High Voltage type (Front EB)		
1	53 mm	17 mm
2	54 mm	17 mm
3	55 mm	13 mm
4	54 mm	17 mm
5	50 mm	17 mm
Low Voltage type (Rear EB)		
1	63 mm	20 mm
2	73 mm	20 mm
3	75 mm	18 mm
4	73 mm	21 mm
5	70 mm	21 mm

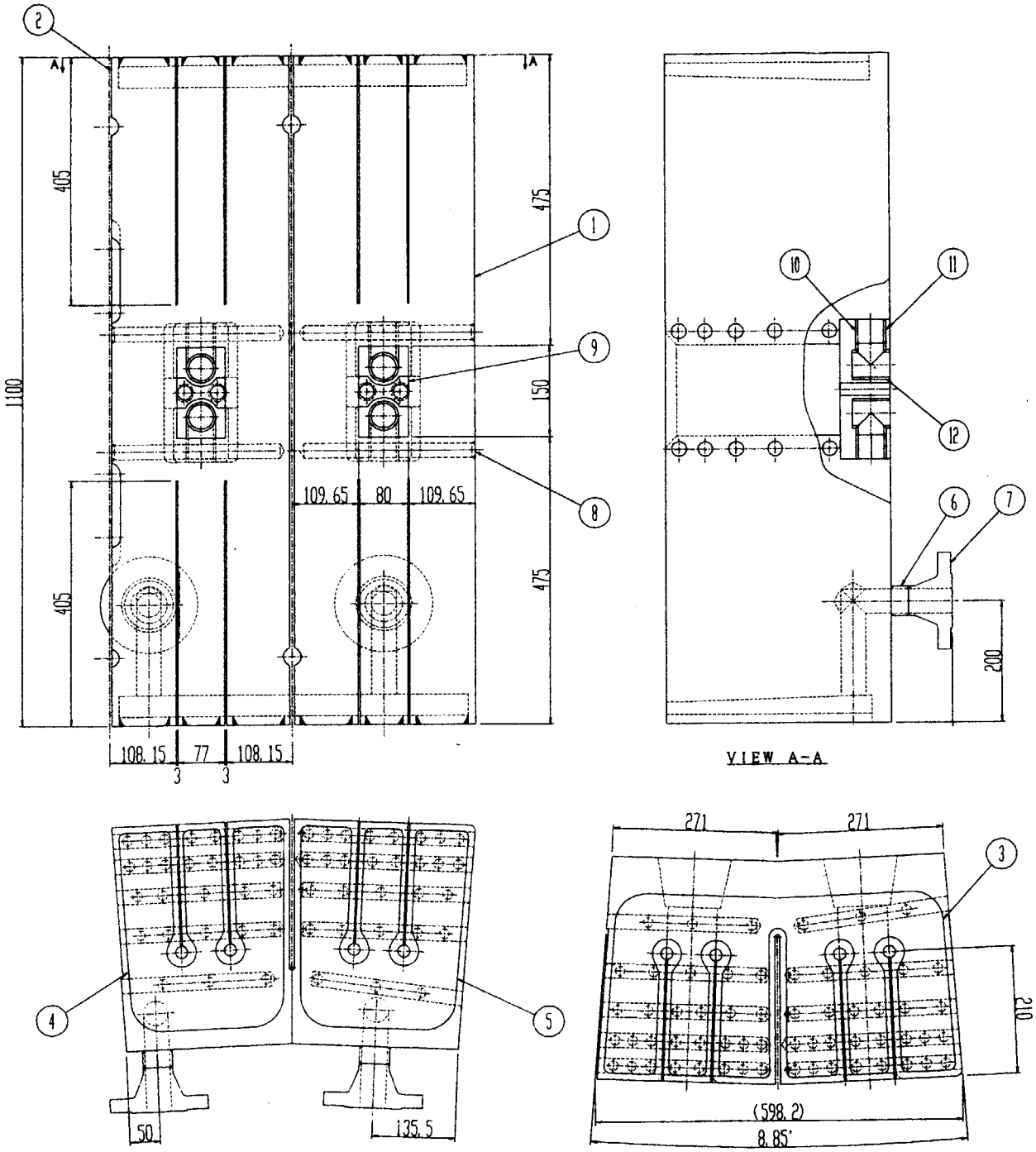

Fig. 1.3.1-1 Configuration of the 1/2 poloidal channel shield block model

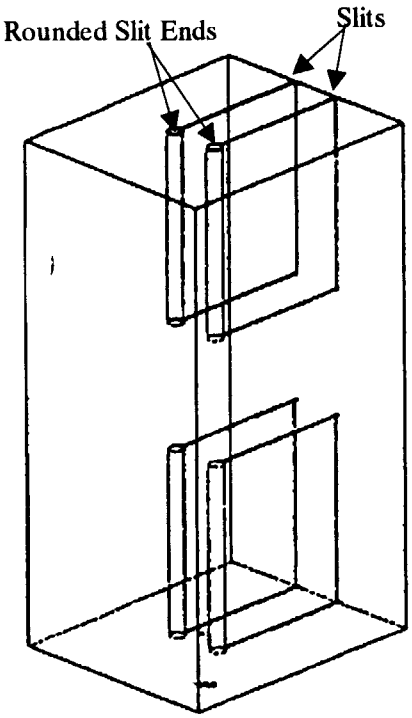

Fig. 1.3.2-1 (1) Slit grooving by Water Jet method

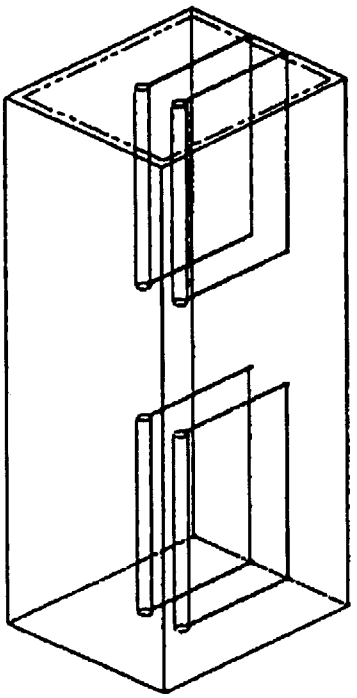

Fig. 1.3.2-1 (2) Coarse Machining of Surface

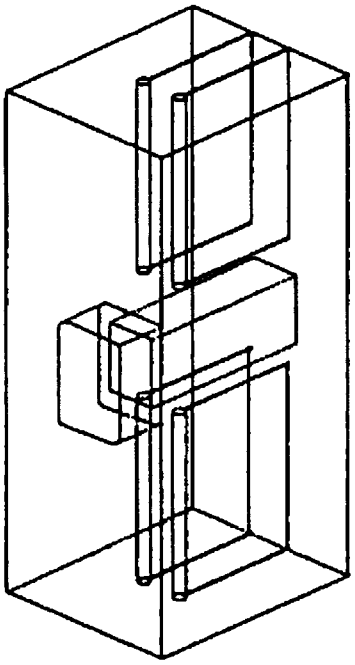

Fig. 1.3.2-1 (3) Shaping of the support leg hole by Wire Cut (EDM)

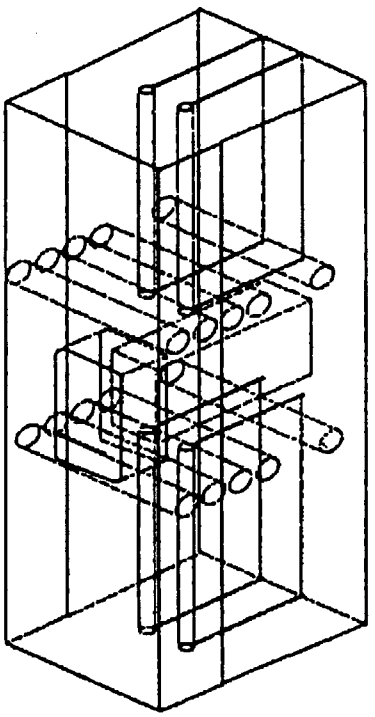

Fig. 1.3.2-1 (4) Drilling of toroidal headers

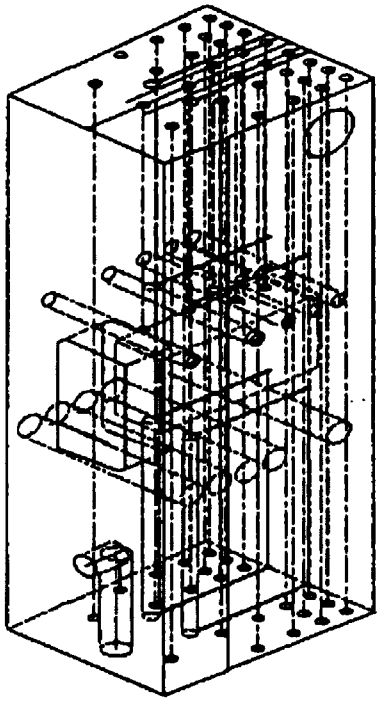

Fig. 1.3.2-1 (5) Drilling of poloidal channels

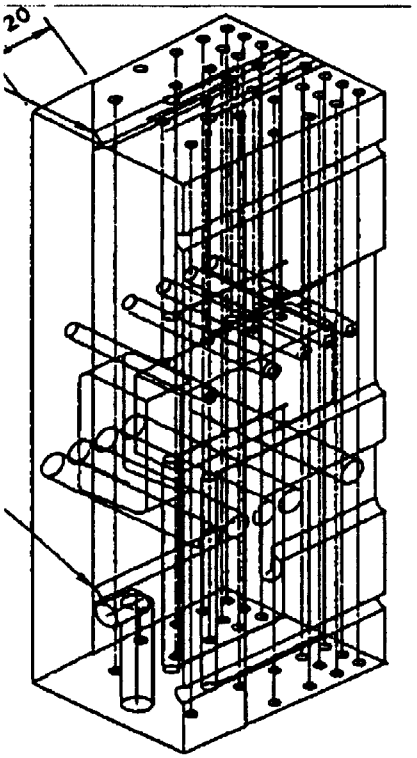

Fig. 1.3.2-1 (6) Drilling of Front Access Holes

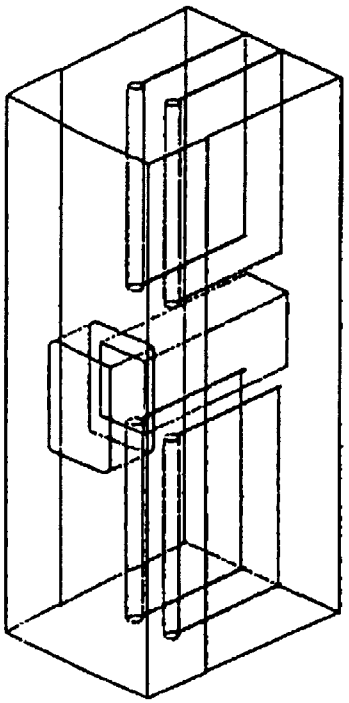

Fig. 1.3.2-1 (7) Machining of outer surface prepare EB welding of SB

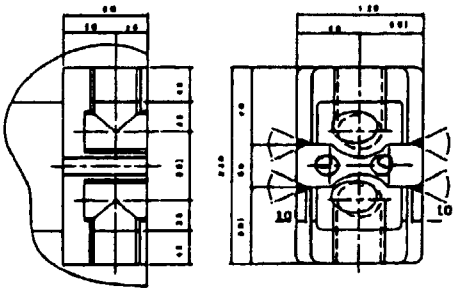

Fig. 1.3.2-1 (8) TIG welding of FW-SB coolant connnectors

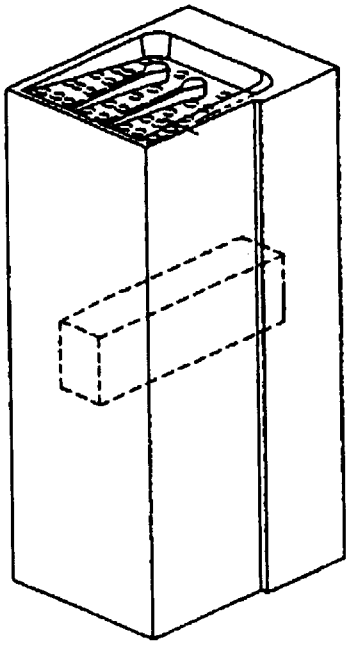

Fig. 1.3.2-1 (9) Machining of upper header

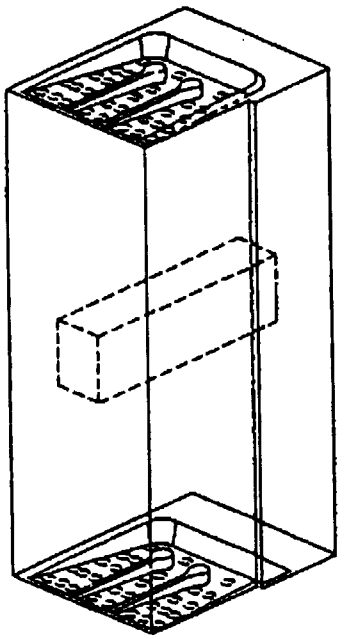

Fig. 1.3.2-1 (10) Machining of lower header

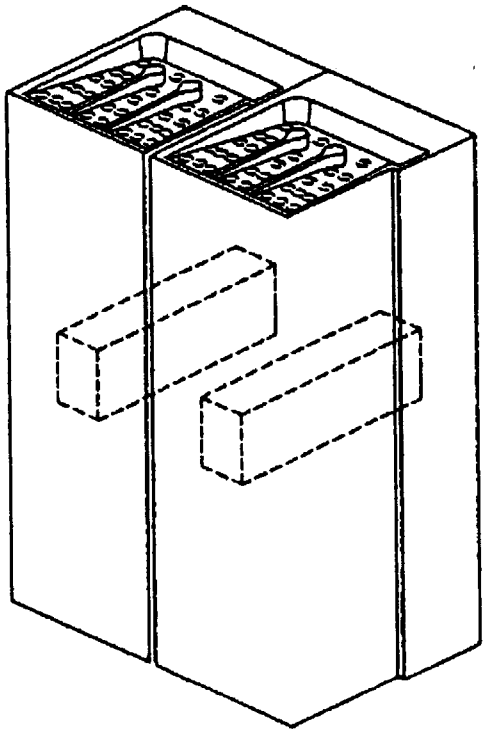

Fig. 1.3.2-1 (11) EB welding of two 1/4 blocks

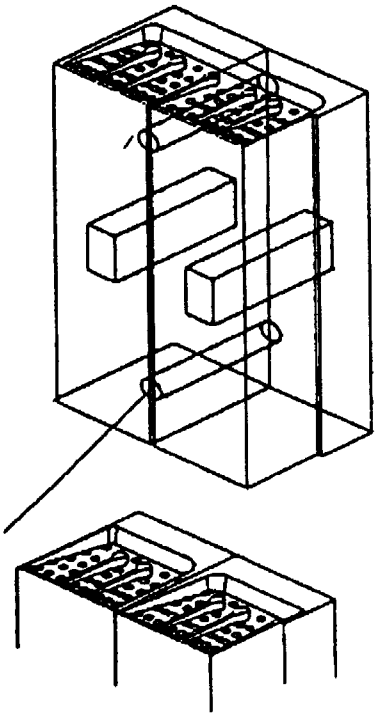

Fig. 1.3.2-1 (12) Drilling of slit ends and finish machining of headers

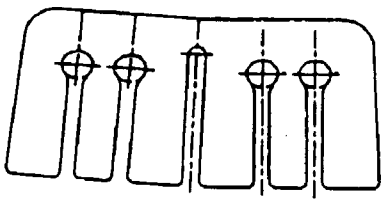

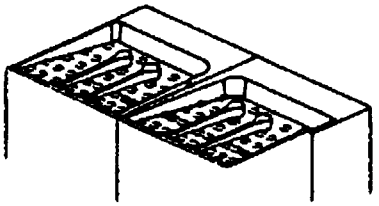

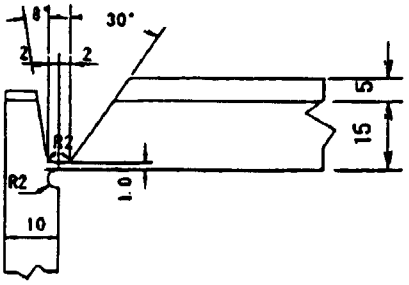

Fig. 1.3.2-1 (13) Shaping and machining finish of header cap plates

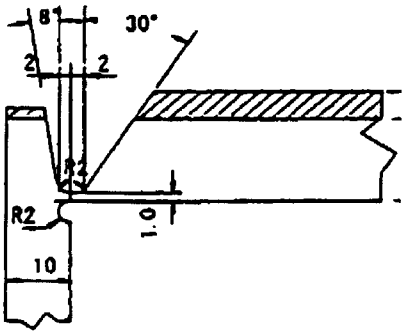

Fig. 1.3.2-1 (14) TIG welding of header cap plates

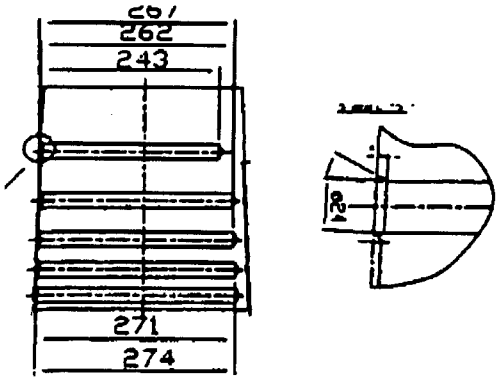

Fig. 1.3.2-1 (15) TIG welding of Plugs for toroidal header holes

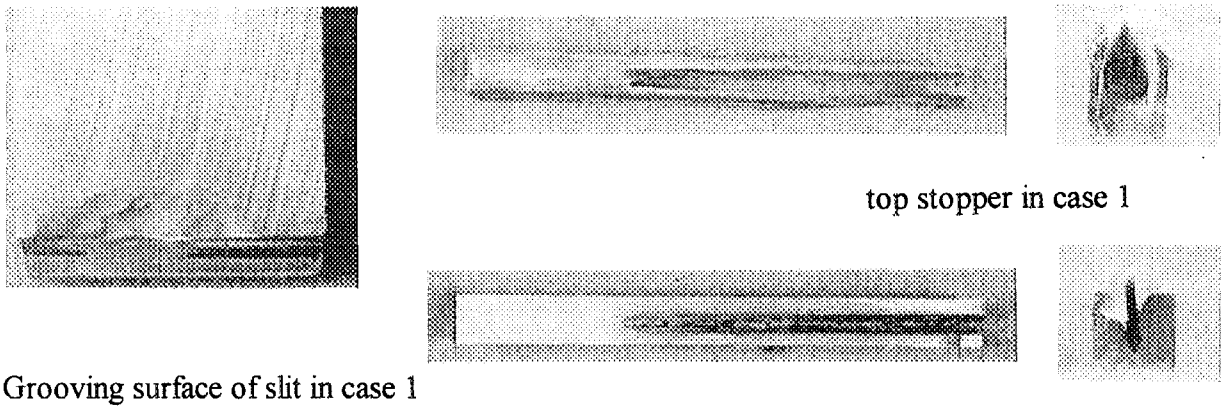

top stopper in case 1

Grooving surface of slit in case 1

bottom stopper in case 1

Fig. 1.3.3-1 (1) Observation of grooving surface and stopping material after test of case 1

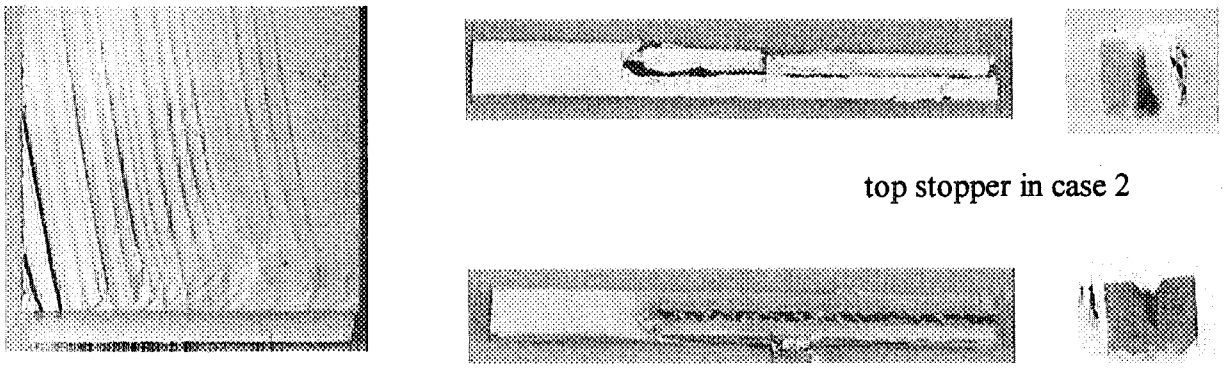

top stopper in case 2

Grooving surface of slit in case 2

bottom stopper in case 2

Fig. 1.3.3-1 (2) Observation of grooving surface and stopping material after test of case 2

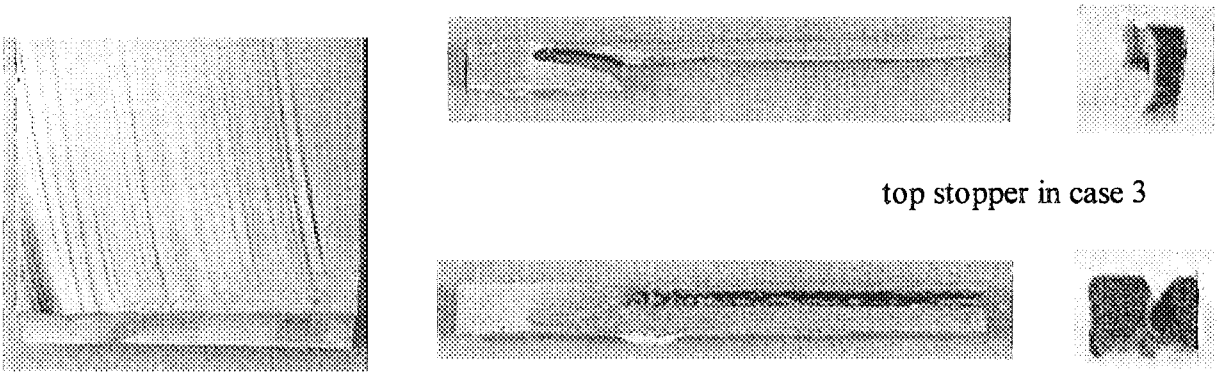

top stopper in case 3

Grooving surface of slit in case 3

bottom stopper in case 3

Fig. 1.3.3-1 (3) Observation of grooving surface and stopping material after test of case 3

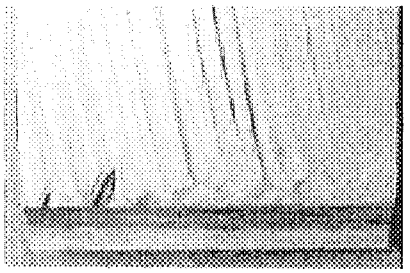

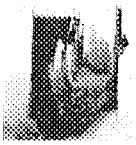

top stopper in case 4

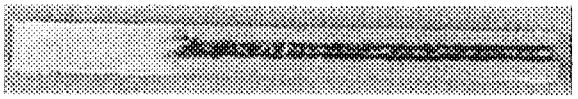

Grooving surface of slit in case 4

bottom stopper in case 4

Fig. 1.3.3-1 (4) Observation of grooving surface and stopping material after test of case 4

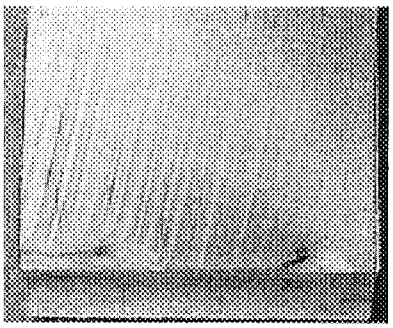

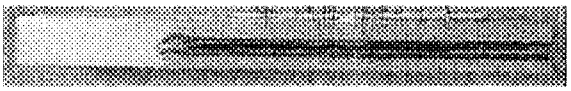

top stopper in case 5

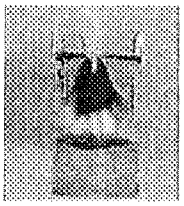

Grooving surface of slit in case 5

bottom stopper in case 5

Fig. 1.3.3-1 (5) Observation of grooving surface and stopping material after test of case 5

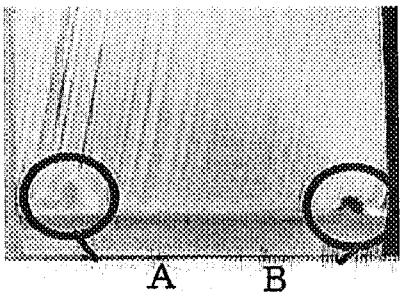

top stopper in case 6

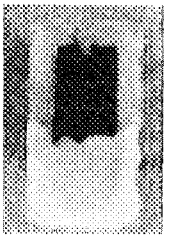

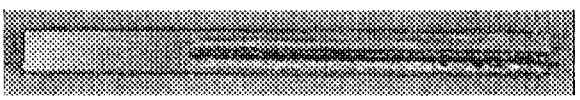

Grooving surface of slit in case 6

bottom stopper in case 6

Fig. 1.3.3-1 (6) Observation of grooving surface and stopping material after test of case 6

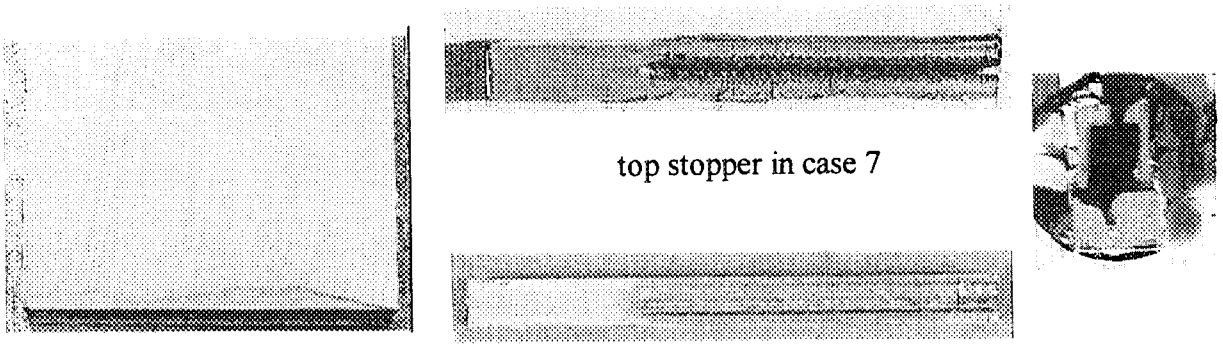

top stopper in case 7

Grooving surface of slit in case 7

bottom stopper in case 7

Fig. 1.3.3-1 (7) Observation of grooving surface and stopping material after test of case 7

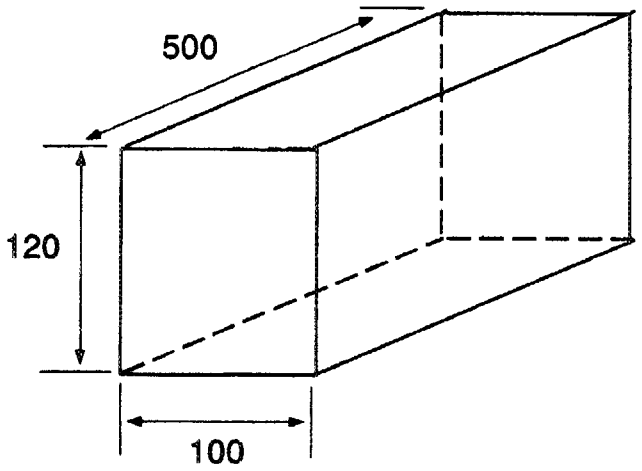

(a) Test piece sketch for Low Voltage type (rear EB) test (penetration depth)

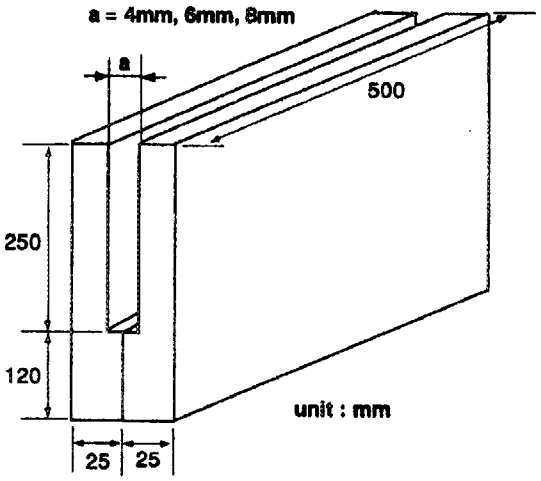

(b) Test piece sketch for high Voltage type (Front EB) test (slit width optimization)

Fig. 1.3.3-2 (a), (b) Test pieces dimension and shapes

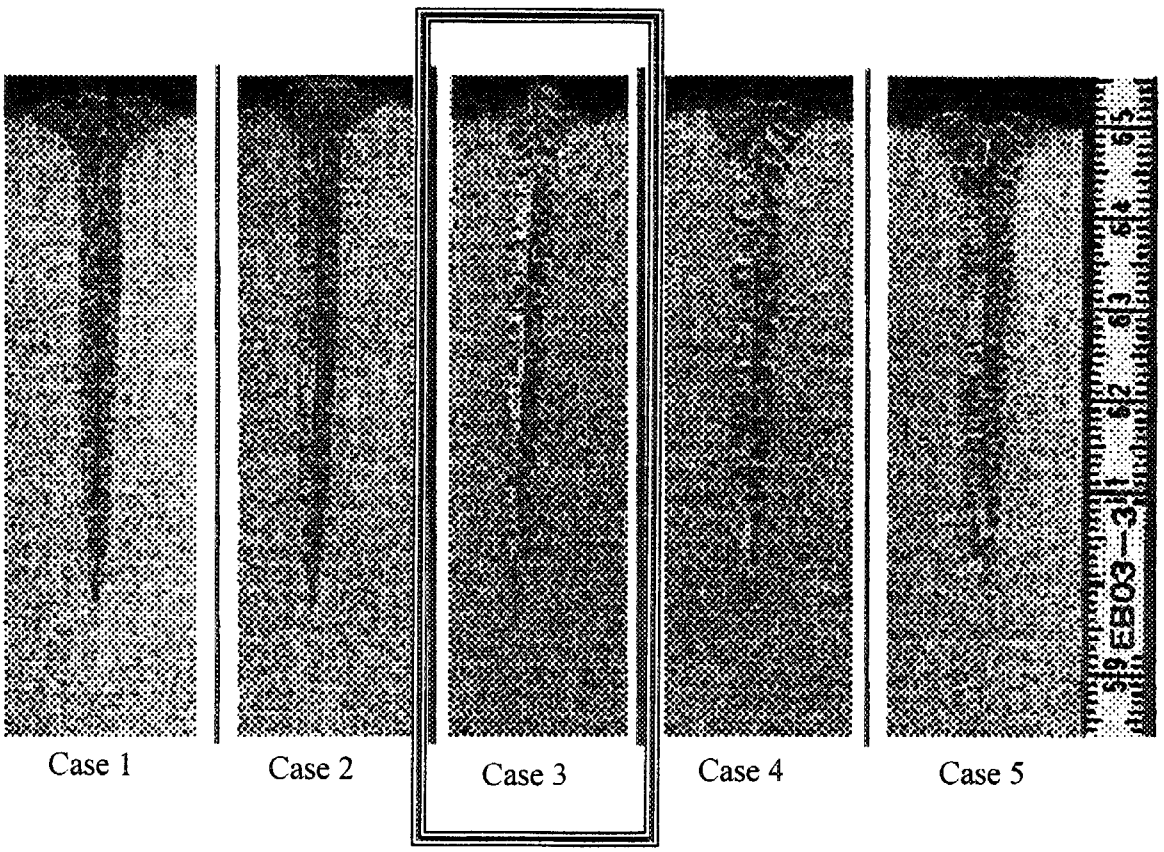

Fig. 1.3.3-3 Macroscopic photographs of cross sectional view of welding bead by high voltage welder tests

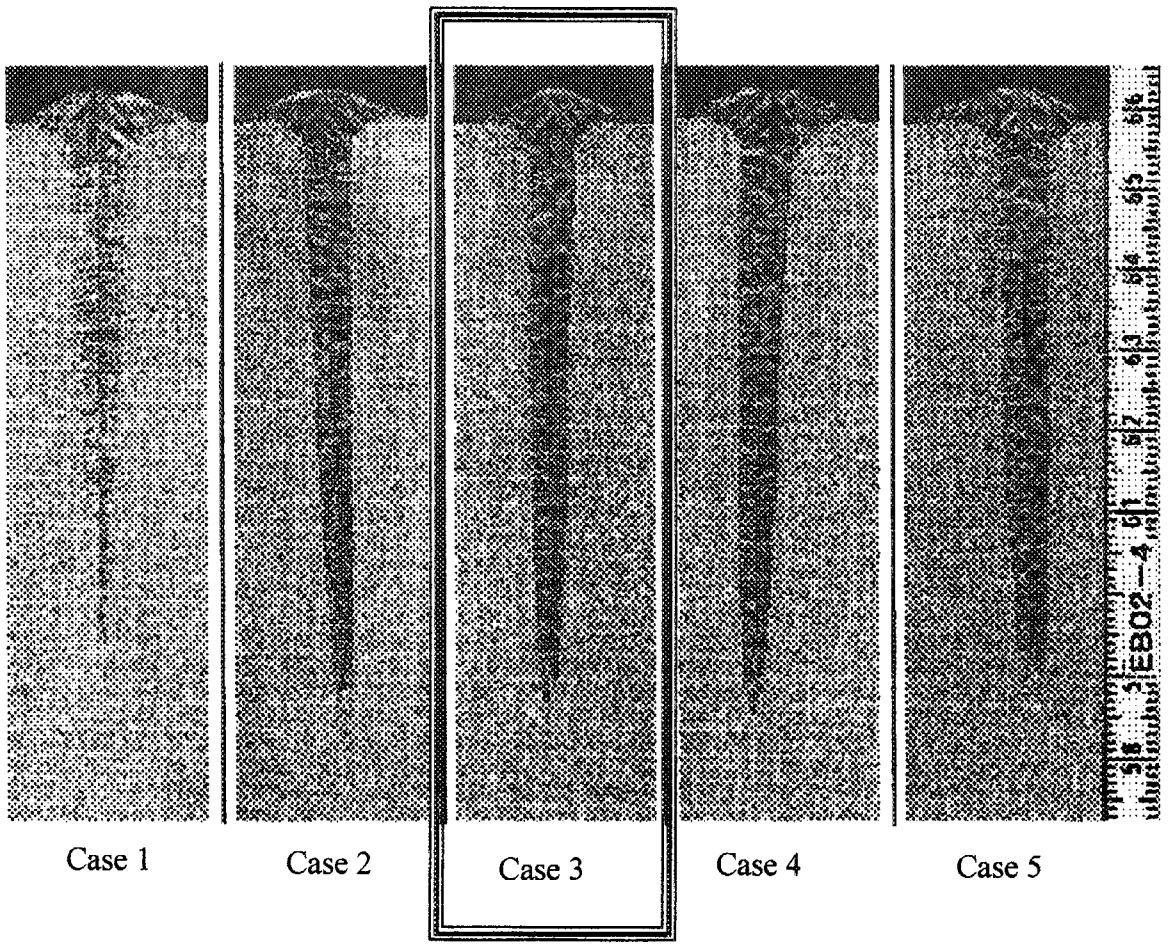

Fig. 1.3.3-4 Macroscopic photographs of cross sectional view of welding bead by high voltage welder tests

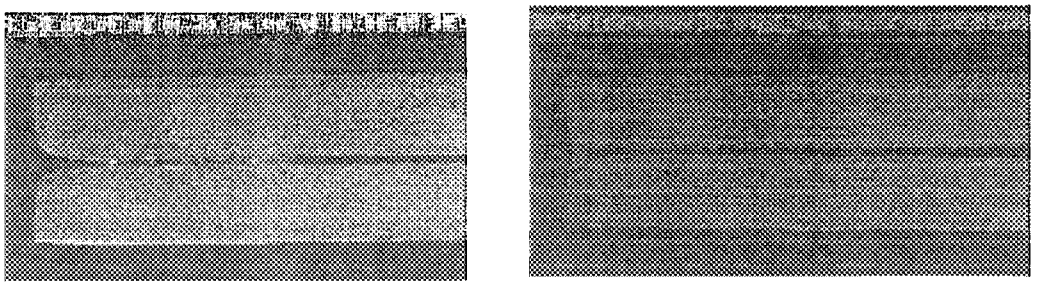

Fig 1.3.3-5 Cross-sectional view of the welding bead obtained for 4 and 6 mm slit width by high Voltage type welder (both showed failure on the plasma side surface of the slit melting

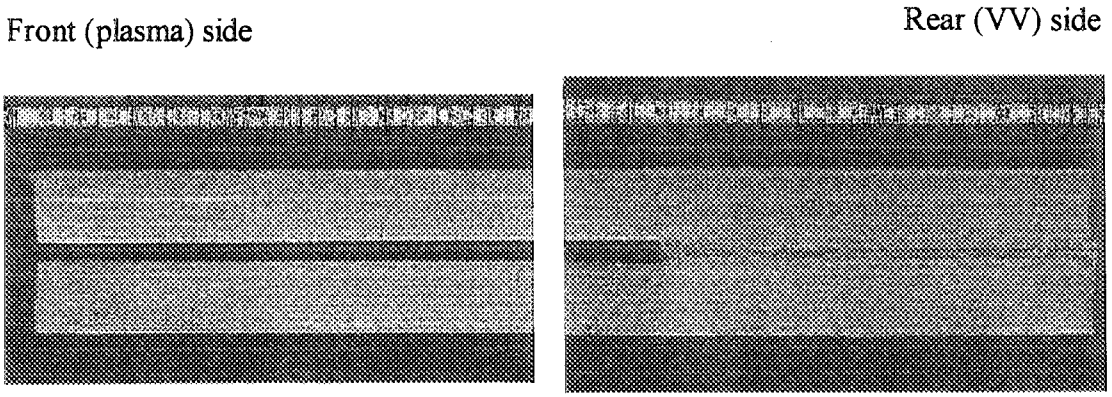

8 mm slit width, by high voltage type welder

Fig 1.3.3-6 Cross-sectional view of the welding bead obtained for 8 mm slit width by high Voltage type welder

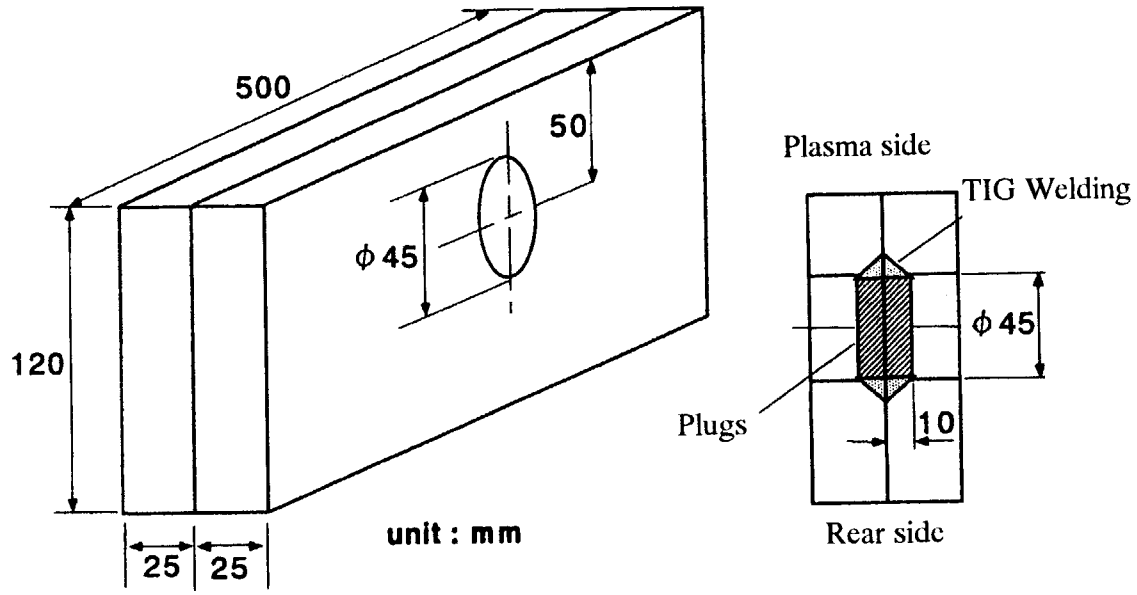

Fig. 1.3.3-7 (a) Test piece dimension for testing effect of the EB welding over TIG welding of the toroidal header plugs of 45 mm diameter

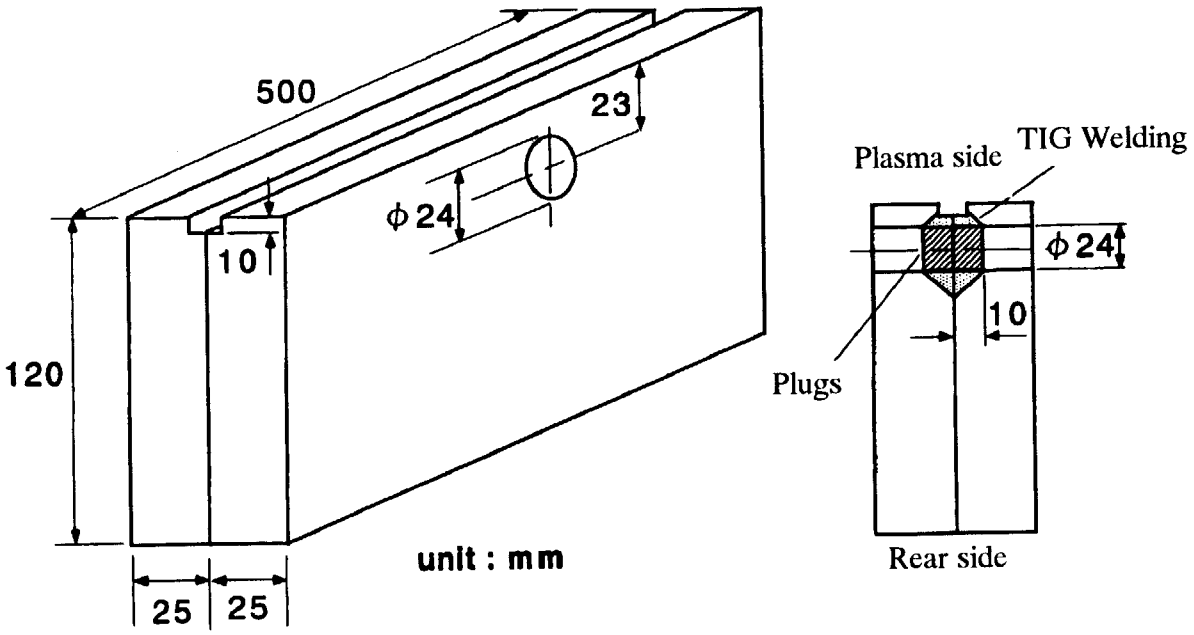

Fig. 1.3.3-7 (b) Test piece dimension for testing effect of the EB welding over TIG welding of the toroidal header plugs of 24 mm diameter

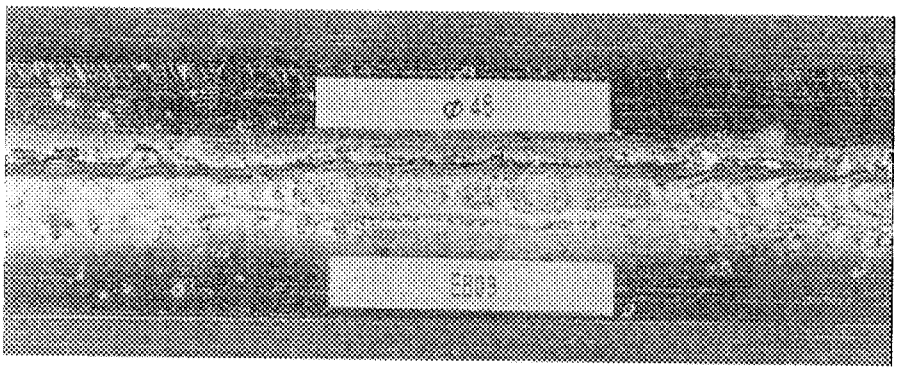

Front side (Bead surface of the High Voltage Type EB welder)

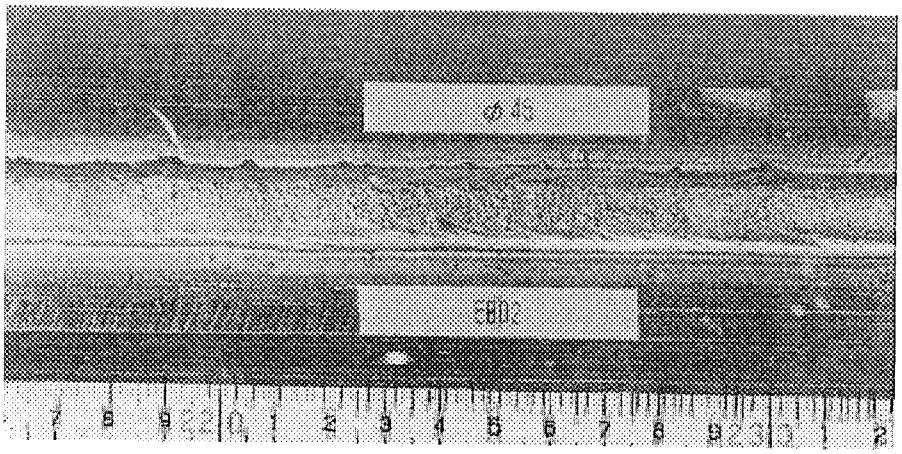

Rear side (Bead surface of the Low Voltage Type EB welder)

Fig. 1.3.3-8 Example of surface photographs of both side of welding line

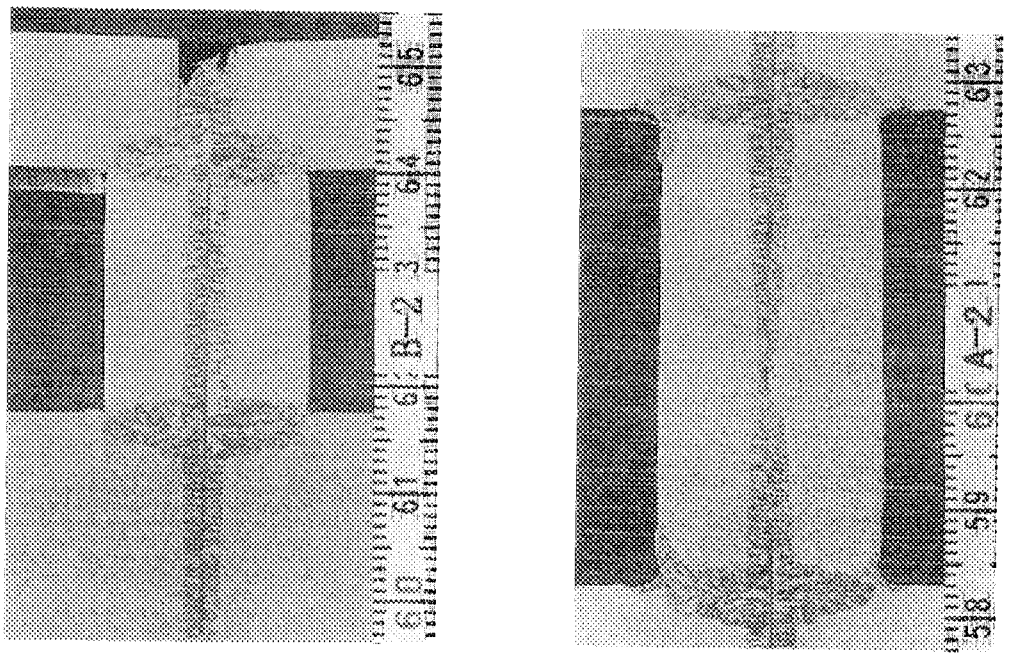

Fig. 1.3.3-9 Cross section observation of the welded plugs (24 mm diameter left, 45 mm diameter right) over welded by EB welding

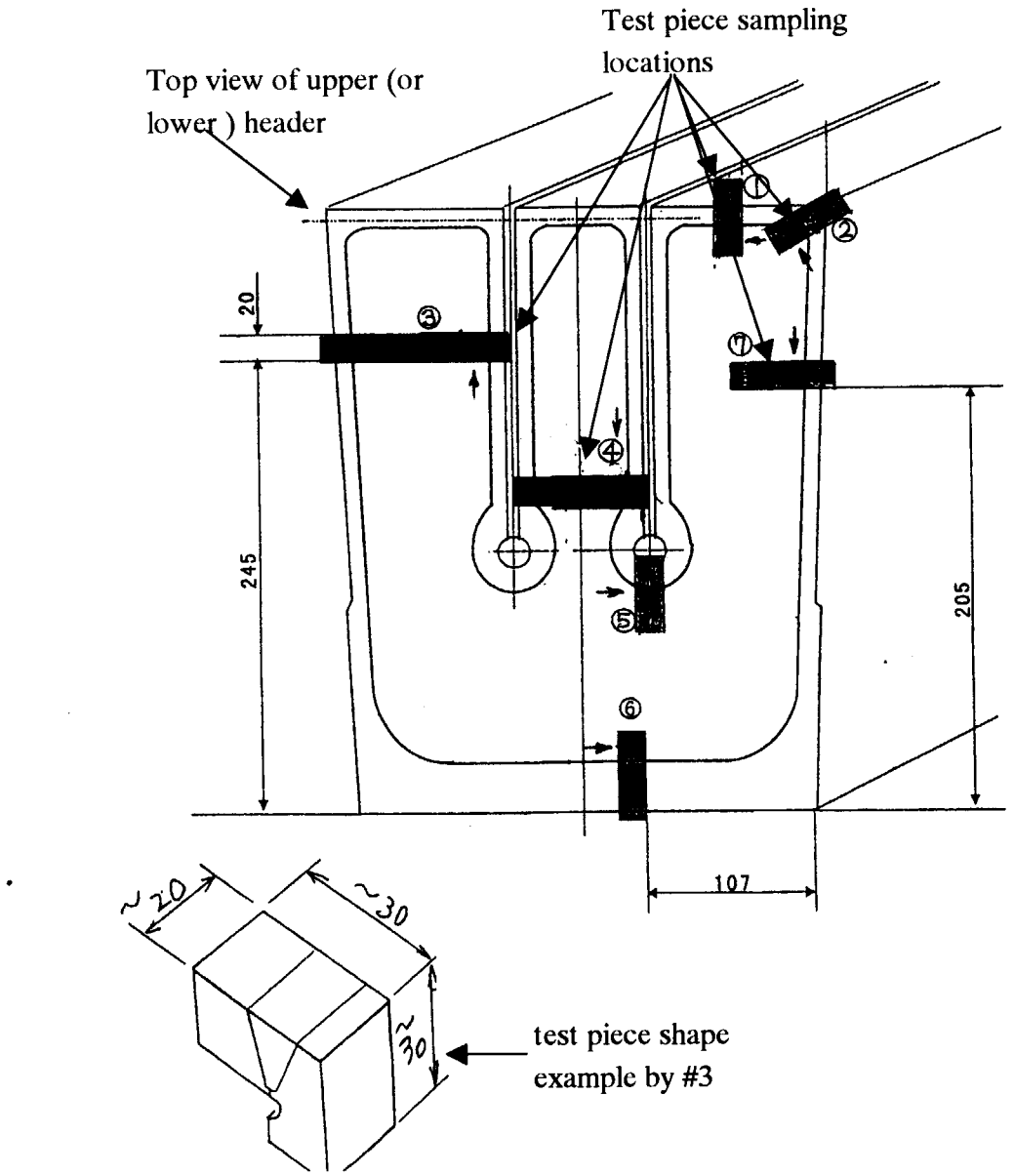

Fig. 1.3.3-10 Test piece sampling location for confirmation test of TIG welding of Header cap plate

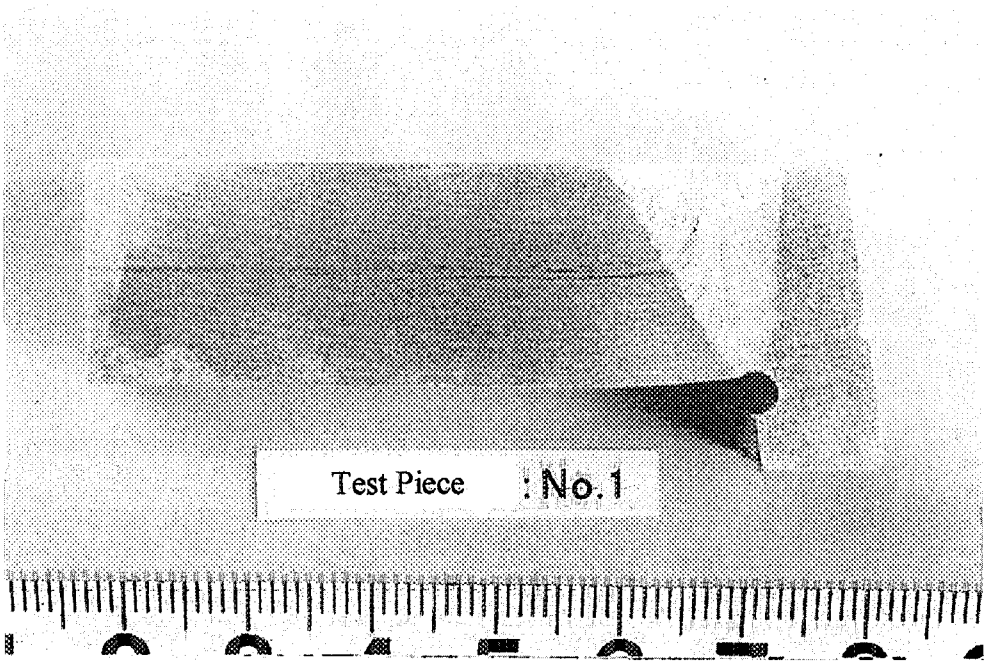

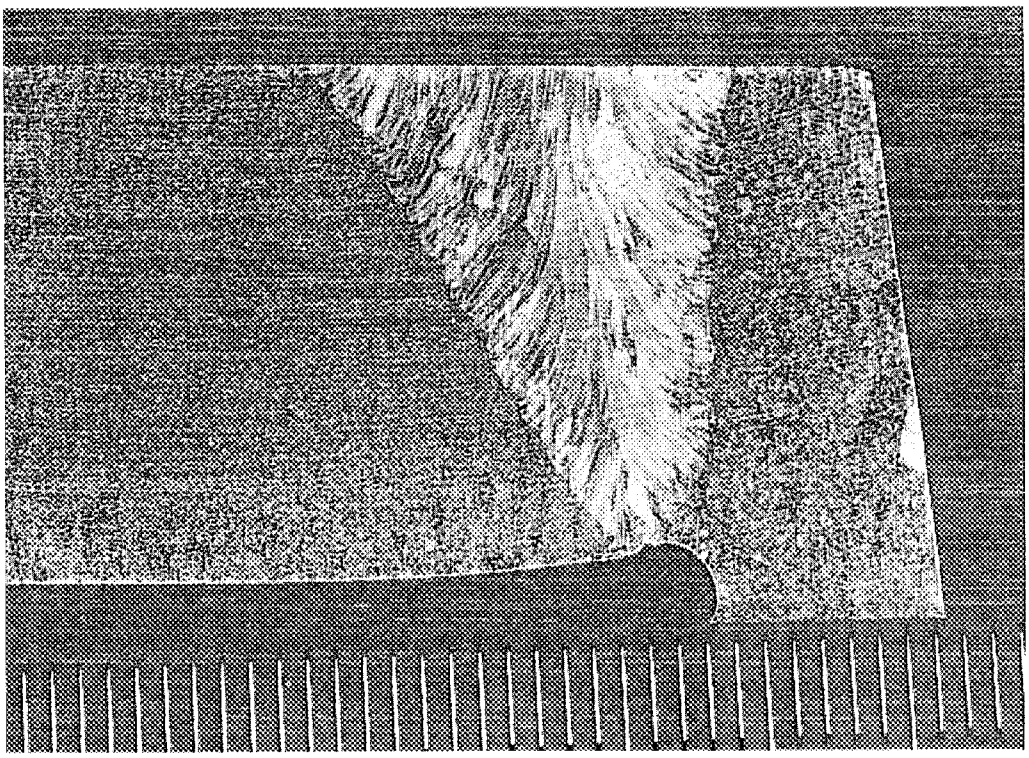

Fig. 1.3.3-11 Macroscopic photograph of the test piece showing TIG welding bead from TP #1

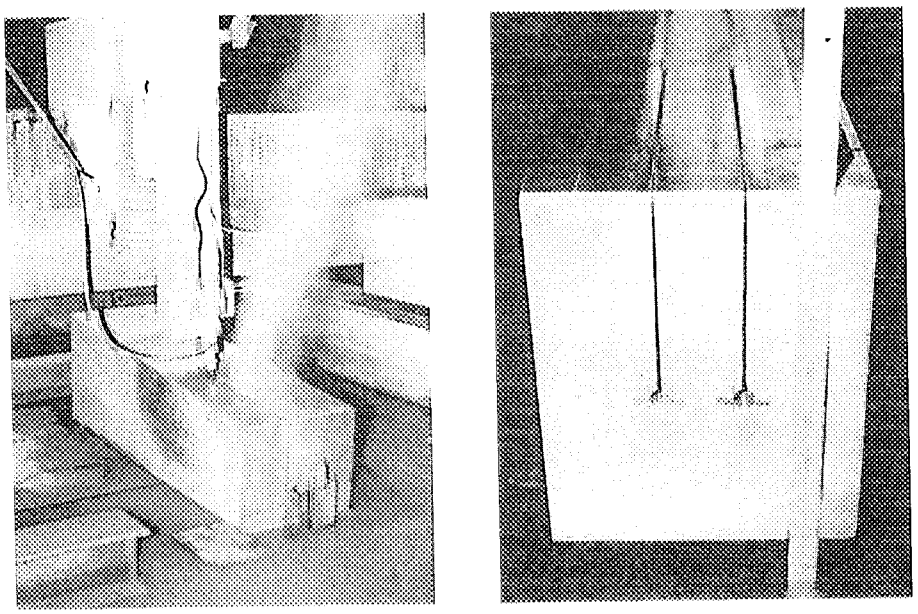

Fig. 1.3.4-1 Slit grooving by water jet method

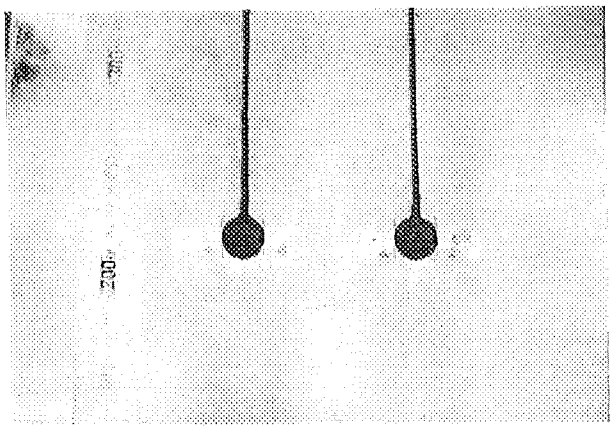

Fig. 1.3.4-2 Slit grooving finish at the bottom of the slit and jet stopping holes

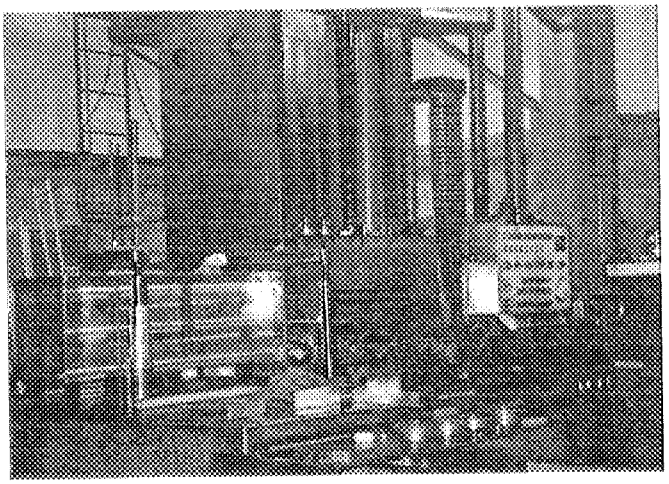

Fig. 1.3.4-3 Set up to gun-drill equipment

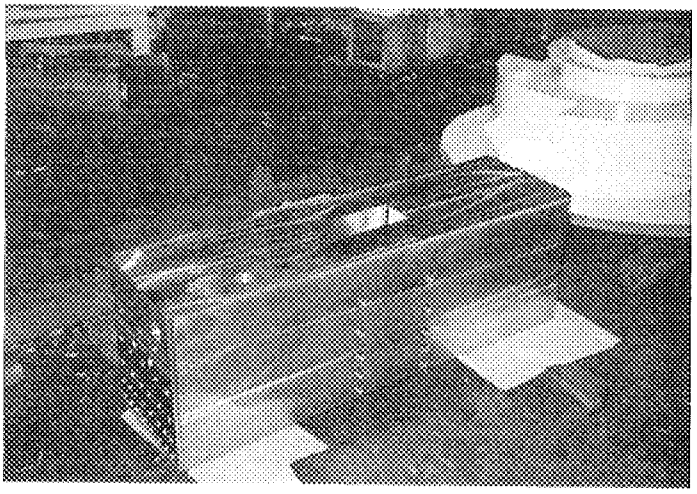

Fig. 1.3.4-4 Appearance of the cooling channels and toroidal headers

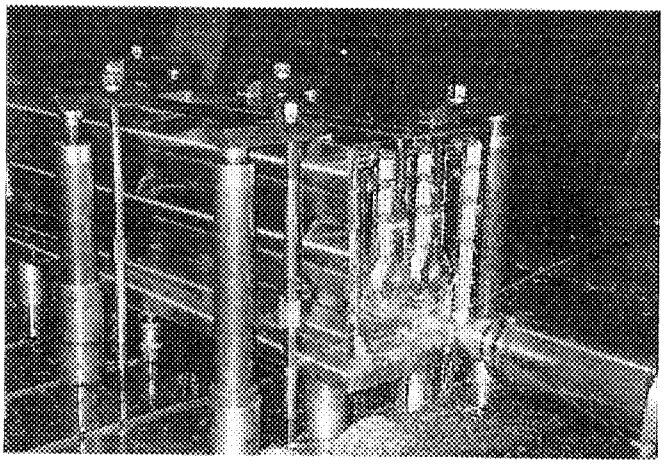

Fig. 1.3.4-5 Machining of the top and bottom headers

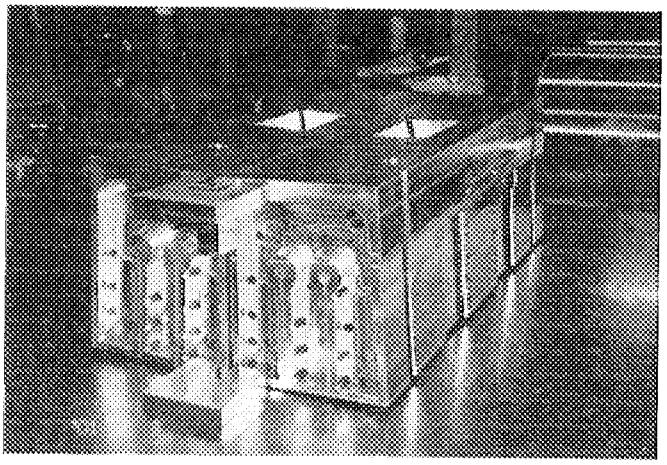

Fig. 1.3.4-6 Preparation for EB welding of two 1/4 shield blocks

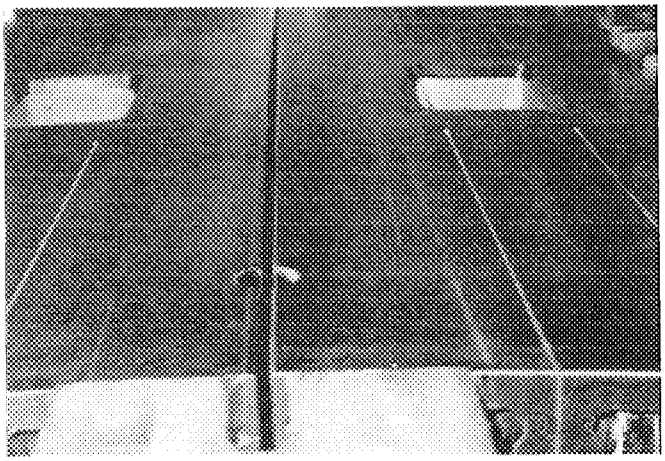

Fig. 1.3.4-7 Appearance of the front part of the slit where the EB go through

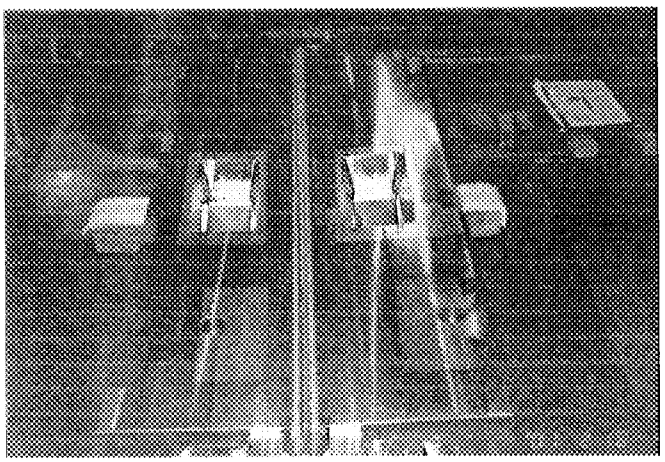

Fig. 1.3.4-8 Appearance of the rear part of the slit where the EB go through

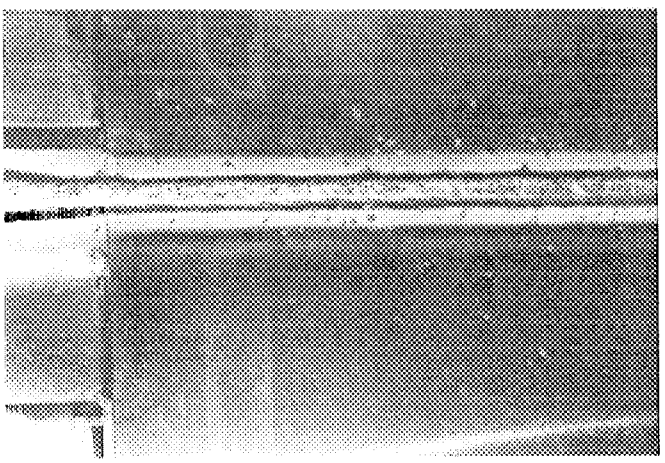

Fig. 1.3.4-9 Close-up appearance of the rear part of the slit where the EB go through

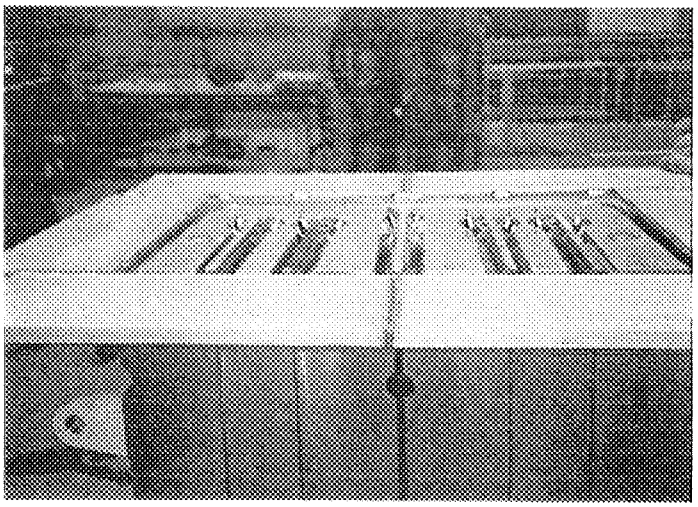

Fig. 1.3.4-10 TIG welding of top and bottom header plates

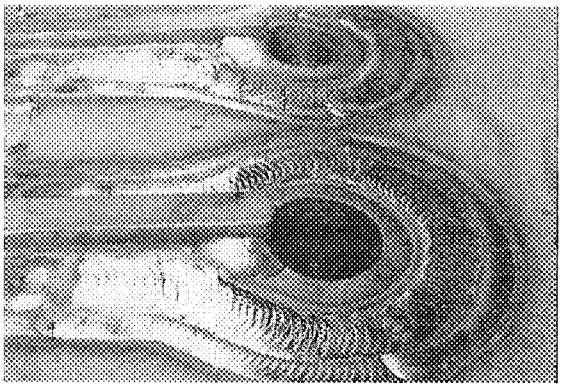

Fig. 1.3.4-11 Appearance after TIG welding of top header plates

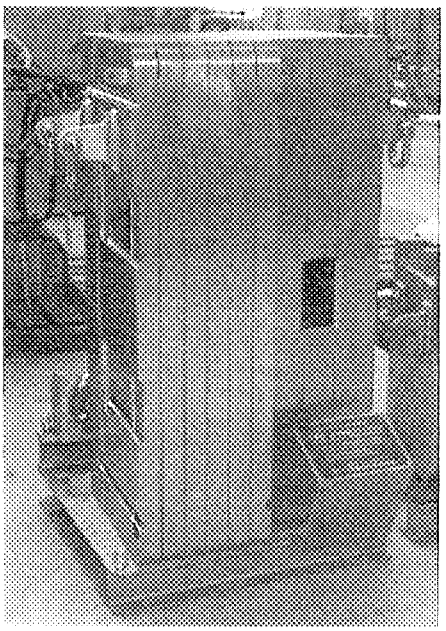

Fig. 1.3.4-12 Fabricated shield block and assembled first wall mockup

3.1.4 1/4 Radial Channel Shield Block Fabrication

3.1.4.1 Design of Be Armored FW Model

Figure 1.4.1-1 and 1.4.1-2 show the specific design sketches of the fabricated 1/4 radial shield block.

3.1.4.2 Fabrication Procedure

Figure 1.4.2-1 shows the flow chart of the fabrication procedure for 1/4 radial channel shield block. Almost all part of the fabrication follows the similar procedure to poloidal channel; shield block fabrication. Coaxial tubes and flanges are additional to poloidal channel shield block fabrication. All necessary information in critical fabrication steps are clarified in the fabrication R&D of 1/2 poloidal channel shield block.

3.1.4.3 Fabrication

Figure 1.4.3-1 shows the forged block after rough machining of outer surface for drilling of radial coolant channels. Figure 1.4.3-2 shows the drilling work to form radial coolant channels. Figure 1.4.3-3 shows the result of machining of the front headers, poloidal headers and toroidal coolant path. Figure 1.4.3-4 shows all prepared parts, shield block, coaxial tubes, coaxial flanges and front header plates just before assembly and final welding. Figure 1.4.3-5 shows welded coaxial cooling tubes in the front header. Figure 1.4.3-6 shows the welded plugs of the holes which interconnect the cooling channels. Figure 1.4.3-7 the final picture after completing the fabrication.

3.1.4.4 Section Conclusions

Basically, there is no additional critical issue to the fabrication technique of poloidal channel shield block. All fabrication process were carried out successfully. Critical issues are already clarified in the previous chapter.

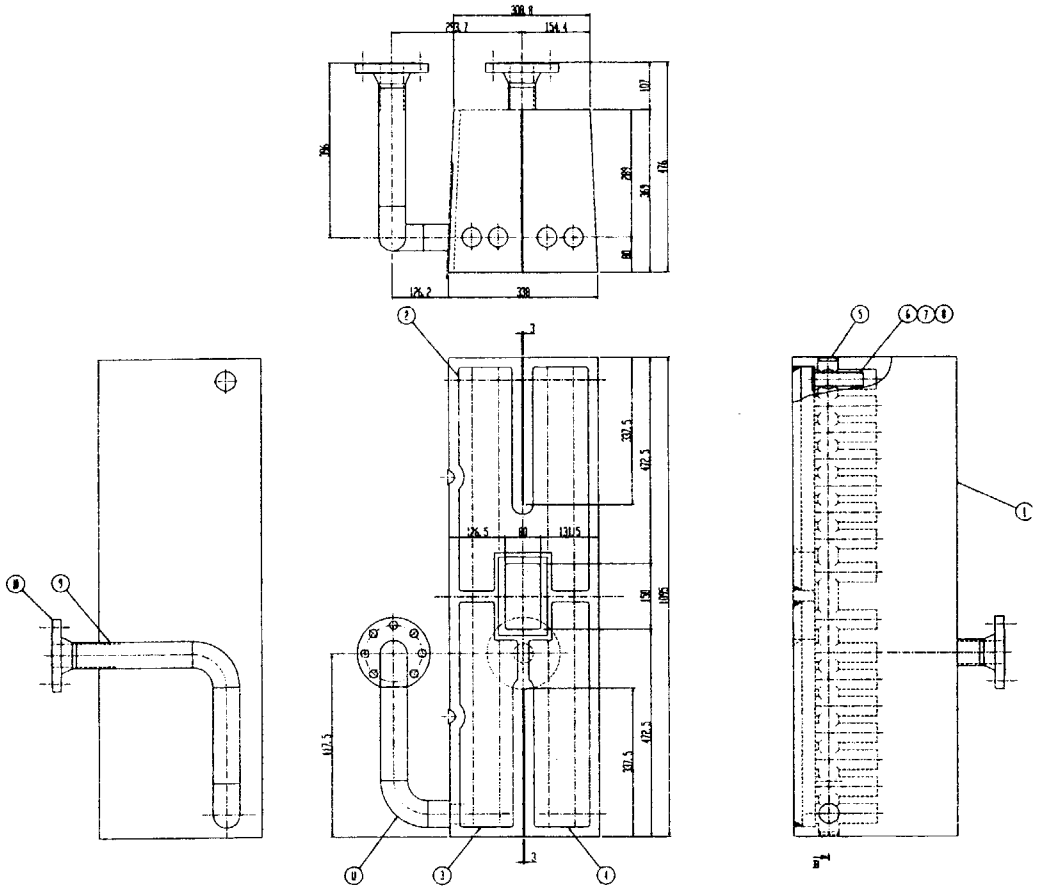

Fig. 1.4.1-1 Design sketch of 1/4 radial channel shield block (1)

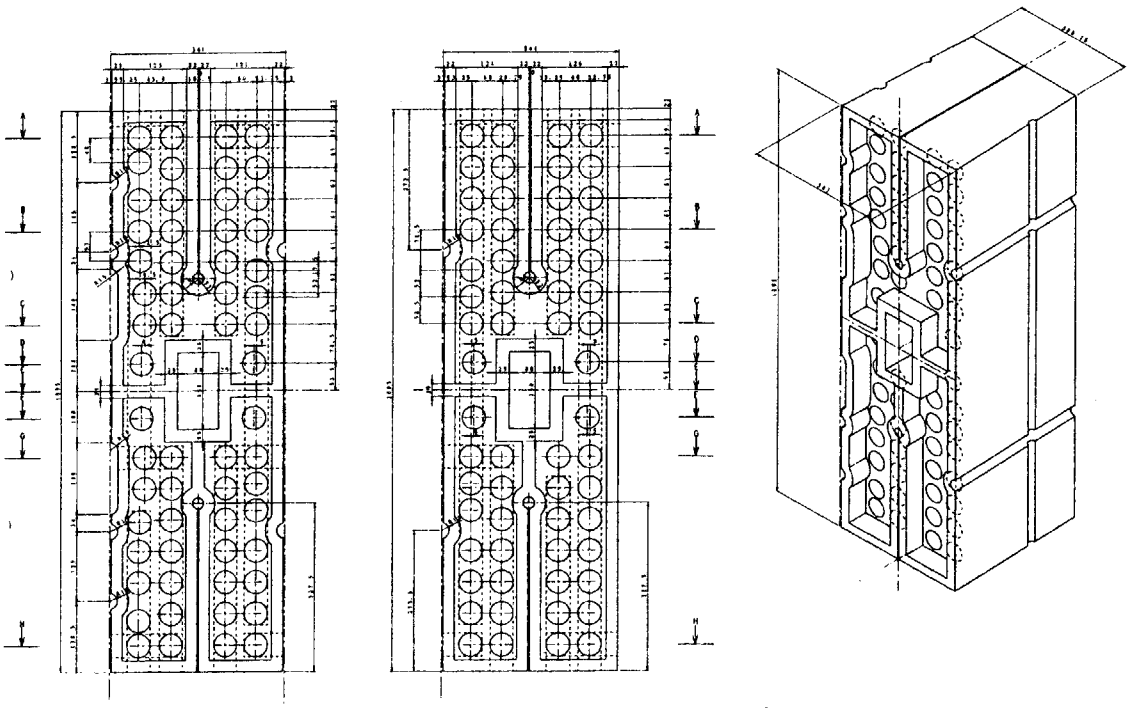

Fig. 1.4.1-2 design sketch of 1/4 radial channel shield block (2)

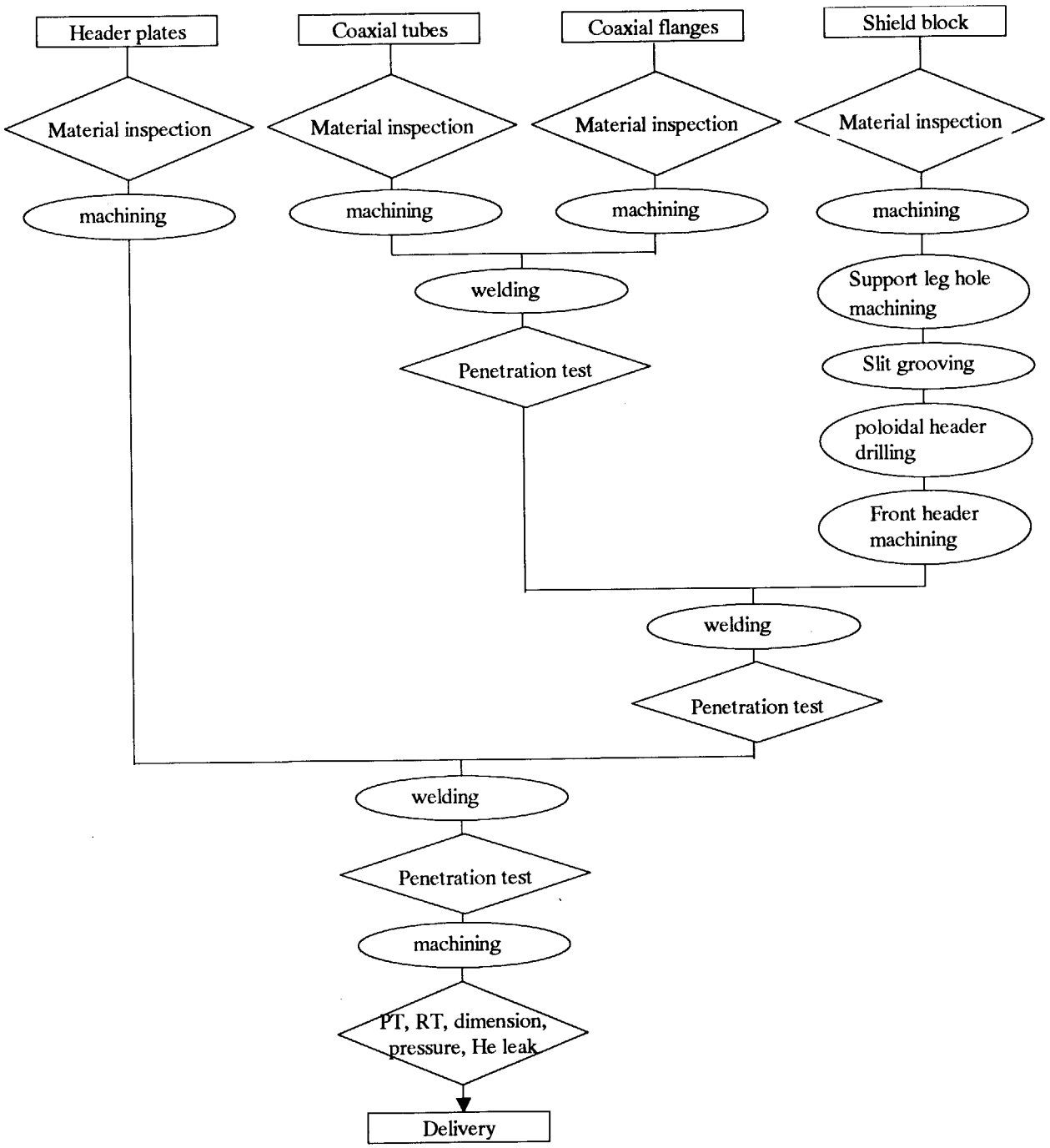

Fig. 1.4.2-1 Flow chart of fabrication procedure for 1/4 radial channel shield block mockup

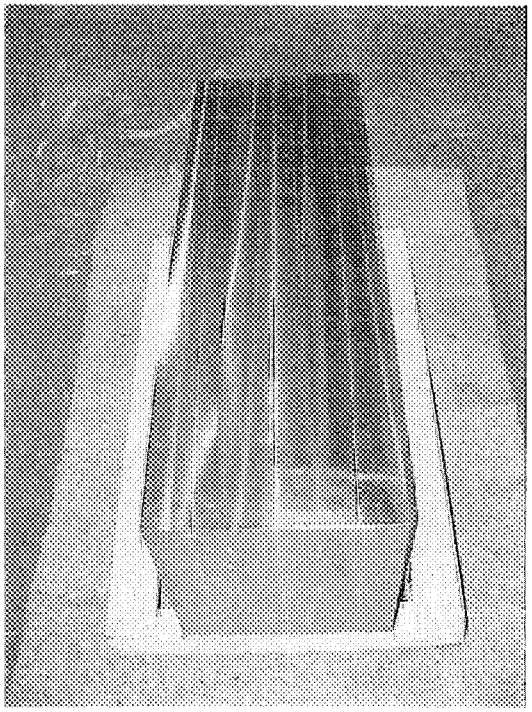

Fig. 1.4.3-1 Forged SS block for shield block

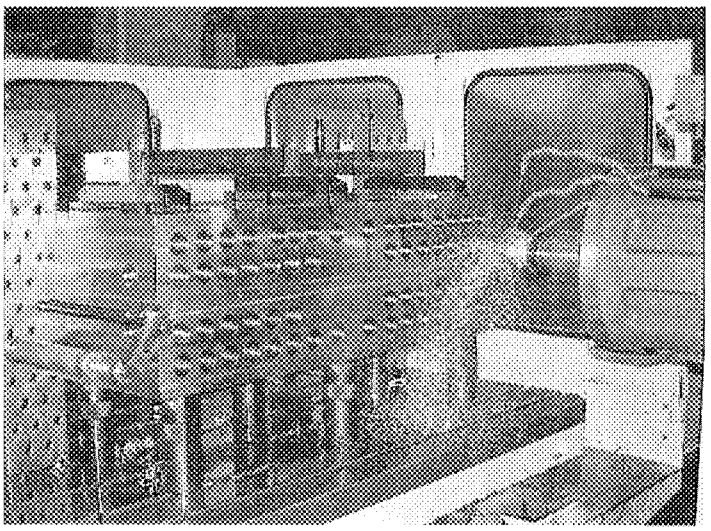

Fig. 1.4.3-2 Drilling of radial coolant channels

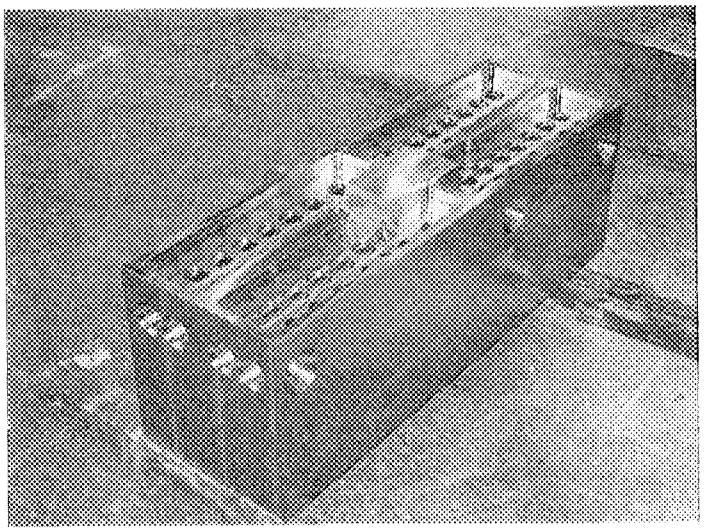

Fig. 1.4.3-3 Machining of the front headers, poloidal headers and toroidal coolant path

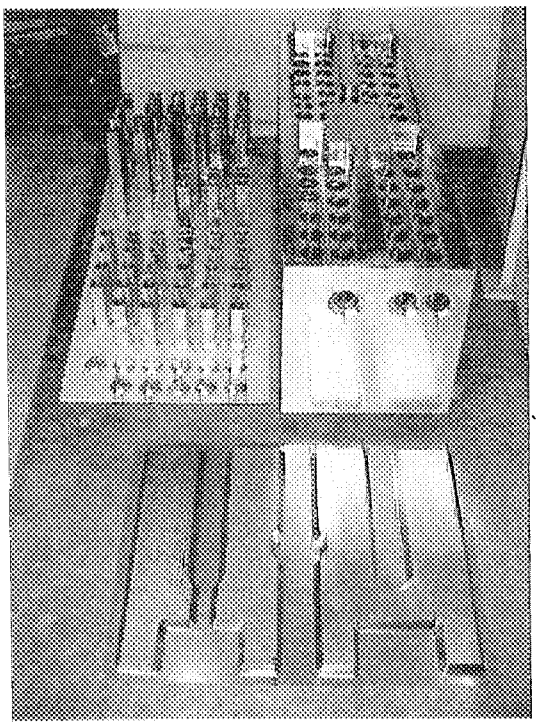

Fig. 1.4.3-4 All prepared parts, shield block, coaxial tubes, coaxial flanges and front header plates

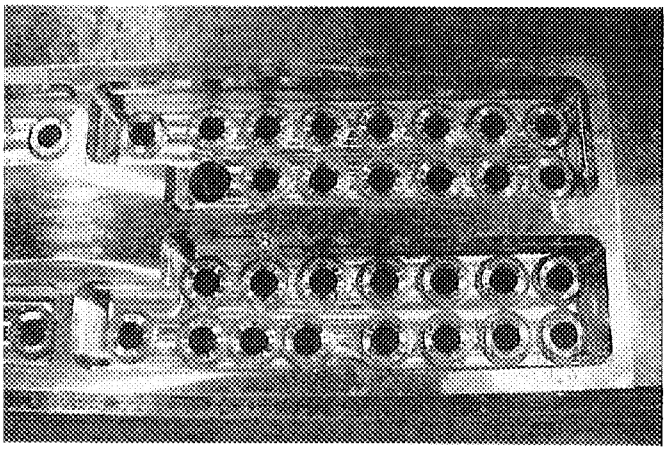

Fig. 1.4.3-5 Welded coaxial insert tube of cooling channels

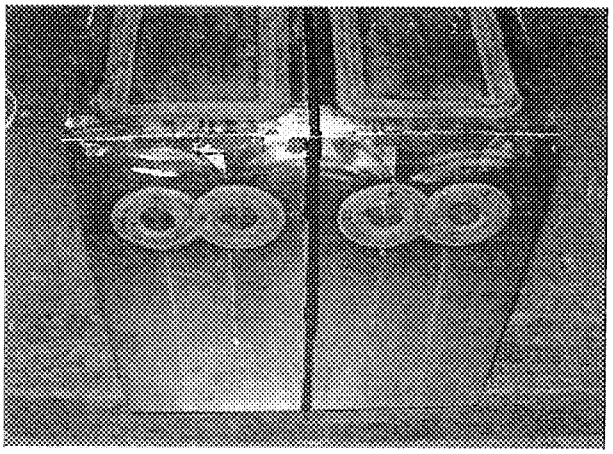

Fig. 1.4.3-6 Welded plugs of poloidal header which interconnect different groups of cooling channels

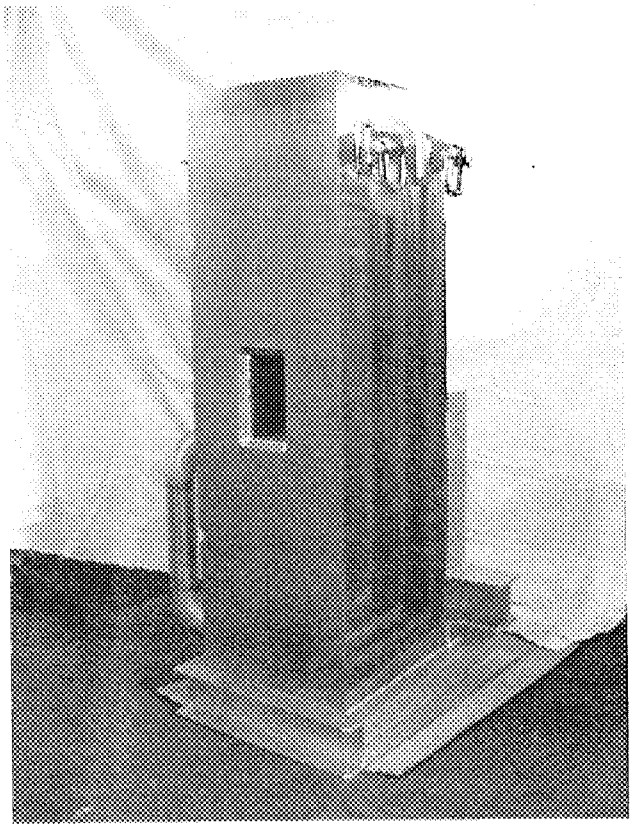

Fig. 1.4.3-7 Fabricated mockup of 1/4 radial channel shield block

3.1.5 Conclusions of Prototype Fabrication

In section 3.1.2, the fabrication technique of full scale width Be armored First Wall Pannel is demonstrated. In section 3.1.3, the fabrication technique of the shield block is demonstrated by using poloidal channel shield blocks. In section 3.1.4, the fabrication technique of the radial channel shield block was demonstrated. With respect to totally full scale first wall panel, Task T420-1 covers the fabrication technique demonstration without Be armor. With respect to the Be joining technique, full scale width demonstration is the critical point and the technique is applied without critical point to full scale FW panel fabrication. In this task, insertion of the full scale FW panel to the fabricated 1/2 shield block was also demonstrated successfully. Concluding to the all R&D results, fabricability of the prototype of the option B separable first wall blanket module was successfully demonstrated.

3.2 Development of NDE Method for FW

3.2.1 Introduction

In the task report of T212, "development of fabrication methods for the Cu-alloy/stainless steel bonding", estimation of detectable defect size was performed for DSCu/SS plate-plate HIP joint. The estimation resulted that 5 MHz of ultra-sonic and 10 MHz of ultra-sonic may detect 1.8 mm and 1.4 mm in diameter, respectively from the thich outer surface of the DSCu part incorporating the noise level of 20 dB. After the above stated theoretical estimation, experimental work for plate-plate NDE tests by using DSCu/SS HIP defect specimens were performed. The test was concluded that, 10 MHz ultra-sonic beam of 1 mm diameter detected minimum of 0.4 mm defect test specimen. Thus, the essential applicability of UT to detect defect between DSCu/SS HIP joint. After the detailed fabrication procedure was researched, it was also clarified that the NDE from inside the cooling channel of the FW panel of DSCu heat sink is important. The development work in this chapter was performed from such background.

3.2.2 Test Procedure

Test items

Specific test items in this work are,

(1) Characteristics of reflection wave at the back side of simple SS tube
(2) Characteristics of reflection wave at the SS tube / DSCu boundary without defect
(3) Characteristics of reflection wave at the SS straight tube / DSCu boundary with artificial defect
(4) Characteristics of reflection wave at the SS bent tube / DSCu boundary with artificial defect

Defect specimen

Figure 2.2-1 shows the configuration of the test specimens used in the tests. Defect size of the specimen was selected from the previous test results stated in previous chapter. Figure 2.2-2 shows example of the test specimen photograph. In the photograph of the backside of straight TP, one can see the defect machined by EDM. Three identical defects, which have same dimension, were machined for one test piece. Configuration of the DSCu/SS tube test pieces are summarized in Table 2.2-1.

As the preliminary reference measurements, half split simple SS tube (10/12 mm inner/outer diameter) was used as the reference test piece.

Detectors

Applied detector was selected from the requirement that detector should be transported inside 10 mm diameter bent tube (R36) and should poses the penetration depth of 1 mm (thickness of the SS tube). Selected detectors are listed in Table 2.2-2. Picture of the detector is shown in Fig. 2.2-3.

Location record

Figure 2.2-4 shows the locationing basement and the location data system. Location of the sensor was logged by X-Y-Z location data.

Test procedure

Detection tests were performed in water. The distance between the detector and the specimen surface is also one of important measurement parameters. This value was changed to 4, 5, and 6 mm by using spacers. The followings are the test procedure.

(1) Set a spacer of 5 mm to TP in water shale.
(2) Set UT sensor
(3) Measure echo for three defects whose dimension is the same on the TP (three data are obtained)
(4) Change the spacer to 4 mm and repeat (2) and (3)
(5) Change the spacer to 5 mm and repeat (2) and (3)
(6) Change the TP which has different defect size
(7) Repeat (1) to (5)
(8) For First TP, use reference split SS tube, first for preliminary reference tests. This data will be used as the standard value for calculation of arbitrary relative echo from raw data.
(9) Then apply straight TP, and measure the echo from no defect part. This data will be the noise level data, which should be distinguished from defect signal.
(10) Then, perform measurements by defect of each TP.

3.2.3 Test Results

3.2.3.1 Reference Measurement

Reference data of echo from back side of simple SS tube was measured for obtaining the baseline echo. Figure 2.3.1-1 shows the test results as the function of spacer distance. In case of type 1 (10 MHz) sensor, spacer dimension of 6 mm gives a few dB higher echo than other spacer dimension (4 and 5 mm). This means spacer distance of 6 mm gives somewhat larger noise. In case of type 2 (30 MHz), there is no effect of spacer distance. The value of echo obtained in this reference measurement is used as the standard data for obtaining arbitrary echo height.

3.2.3.2 Characteristic Measurement at No Defect Part of DSCu/SS HIP Straight Test Pieces

Figure 2.3.2-1 shows the characteristics of the reflection wave from DSCu/SS boundary without defect as the function of spacer distance. As can be seen from this figure, the normalized echo was -3 to -5 dB by type 1 (10 MHz) and -12 to -17 dB by type 2 (30 MHz). The deviation of the data is considered as the measurement error.

3.2.3.3 Characteristic Measurement of Defect of DSCu/SS HIP Straight Test Pieces

Figure 2.3.3-1 shows the typical echo wave. The figure shows comparison of wave photograph of no defect and 0.9 mm defect by type 1 sensor (10 MHz). The marked point is the wave peak of defect.

With respect to the test result of type 1 sensor (10 MHz), Fig. 2.3.3-2, 3 and 4 show the results of spacer distance of 4, 5 and 6 mm, respectively, as the function of defect size. As can be seen from those figures, the relative echo height becomes 6 dB larger from 0.3 mm to 0.6 mm defect. As the defect become 0.9, the increase of echo height is 1 to 2 dB. The echo height deviated by the difference of spacer distance, however, the deviation was small enough compared

to the measurement deviation itself. No clear correlation was observed on the effect of the spacer distance by the results.

Figure 2.3.3-5, 6 and 7 show the results of spacer distance of 4, 5 and 6 mm, respectively, as the function of defect size by type 2 sensor (30 MHz). In case of type 2, the increase of the echo wave is linear (5 to 6 dB for both of 0.3 to 0.6 mm and 0.6 to 0.9 mm) for defect size change up to 0.9 mm.

All size of defect was detectable in this measurement runs. Type 2 sensor showed higher sensitivity because width of the echo by type 2 (30 MHz) is smaller than type 1 (10MHz). However, the echo wave of 0.6 mm defect was hard to be distinguished from the echo wave of the inner surface echo. In case of 0.3 mm defect, it was very difficult to distinguish between them without state-of art technique of veteran technicians.

3.2.3.4 Characteristic Measurement of Defect of DSCu/SS HIP Bent Tube Test Pieces

Inside Bent TP

In case of type 1 sensor (10 MHz), Fig. 2.3.4-1, 2 and 3 show the results of spacer distance of 4, 5 and 6 mm, respectively, as the function of defect size. As can be seen from those figures, the relative echo height becomes 4 to 8 dB larger from 0.3 mm to 0.6 mm defect. As the defect become 0.9, the increase of echo height is 2 to 6 dB. The echo height deviated by the difference of spacer distance, however, the deviation was small enough compared to the measurement deviation itself and, also, no clear correlation was observed on the effect of the spacer distance by the results, as observed in straight TP measurements. Figure 2.3.4-4, 5 and 6 show the results of spacer distance of 4, 5 and 6 mm, respectively, as the function of defect size by type 2 sensor (30 MHz). In case of type 2, the increase of the echo wave was, 5 to 6 dB for 0.3 to 0.6 mm defect size increase and 6 to 8 dB for 0.6 to 0.9 mm defect size increase. The sensitivity tendency was the same as the straight TP.

Outside Bent TP

In case of type 1 sensor (10 MHz), Fig. 2.3.4-7, 8 and 9 show the results of spacer distance of 4, 5 and 6 mm, respectively, as the function of defect size. As can be seen from those figures, the relative echo height becomes 2 to 5 dB larger from 0.3 mm to 0.6 mm defect. As the defect become 0.9, the increase of echo height is the same or a few dB larger, in case of 4 and 5 mm spacer distance. However, in case of spacer distance of 6 mm, as the defect become 0.9, the echo height decreased a few dB. The echo height deviated by the difference of spacer distance, however, the deviation was small enough compared to the measurement deviation itself and, also, no clear correlation was observed on the effect of the spacer distance by the results, as observed in straight TP measurements. Figure 2.3.4-10, 11 and 12 show the results of spacer distance of 4, 5 and 6 mm, respectively, as the function of defect size by type 2 sensor (30 MHz). In case of type 2, the increase of the echo wave was, 5 to 6 dB for 0.3 to 0.6 mm defect size increase and 6 to 8 dB for 0.6 to 0.9 mm defect size increase.

With respect to the sensitivity tendency, the angular of the sensor was most sensitive in bent TP cases because the perpendicular injection of the ultra sonic gives the most effective echo.

On the other hands, echo becomes smaller by angular.

Side TP

In case of type 1 sensor (10 MHz), Fig. 2.3.4-13, 14 and 15 show the results of spacer distance of 4, 5 and 6 mm, respectively, as the function of defect size. As can be seen from those figures, the relative echo height becomes a few dB larger if the defect size becomes larger from 0.3 mm to 0.6 mm and, also, 0.6 to 0.9 mm in case of spacer distance of 4 and 5 mm. In case of spacer distance of 6 mm, as the defect become larger from 0.6 to 0.9, the echo height was the same or smaller. Figure 2.3.4-16, 17 and 18 show the results of spacer distance of 4, 5 and 6 mm, respectively, as the function of defect size by type 2 sensor (30 MHz). In case of type 2, echo height was largest in case of the defect size of 0.9 mm and echo of 0.6 mm was the same or smaller than that of 0.3 mm. The sensitivity tendency was the same as the inside and outside bent TP.

3.2.3.5 Discussion of the Detection Ability

Table 2.3.5-1 shows the summary of the detection ability. The evaluation was made by comparing each data with the echo of no defect boundary of DSCu/SS tube. The factor of the 6 dB was selected for the consideration of effective defect area ratio in the same wave area for larger defect size in this work. In case of 0.3 mm defect, only side bent TP resulted excellent sensitivity by type 2 (30 MHz). Defect of 0.3 mm in other position is technically difficult.

3.2.4 Conclusions

The followings are the conclusions of this work.

(1) Type 2 (30 MHz) is more sensitive than type 1(10 MHz).

(2) Side of bent part gives less effect of bending and for this reason high sensitivity is expected.

(3) Inside or outside of bent part gives lower sensitivity.

(4) Automatic defect sensing may normally require 6 dB safety factor. Incorporating this factor, 0.9 mm is the minimum defect size which can be guaranteed by detection inspection.

Table 2.2-1 DSCu/SS tube test piece configuration

Defect width	Test piece shape			
	Straight	Bent inside	Bent outside	Bent side
0.3mm	1	1	1	1
0.6mm	1	1	1	1
0.9mm	1	1	1	1

Table 2.2-2 Specification of detectors applied in this tests

	Type 1	type 2
Frequency	10 MHz	30 MHz
Type of detector	convergence type, non-contact	convergence type, non-contact
Biblater dimension	4 mm diameter	4 mm diameter
Detector dimension	7 mm dia. x 14 mm length	5.5 mm dia. x 10 mm length

Table 2.3.5-1 Summary of the detection ability

Sensor type	Defect size	straight	Inside bent	Outside bent	Side bent
Type 1 (10 MHz)	0.9 mm	excellent	excellent	excellent	excellent
	0.6 mm	good	fair	good	excellent
	0.3 mm	no	no	fair	Fair
Type 2 (30 MHz)	0.9 mm	excellent	excellent	excellent	excellent
	0.6 mm	excellent	good	good	excellent
	0.3 mm	good	fair	fair	excellent

excellent: All data are more than the echo of no defect DSCu/SS boundary.

good: Part of data are below the echo of no defect DSCu/SS boundary, however, detection is enough possible practically.

fair: Half of data are below the echo of no defect DSCu/SS boundary, however, detection is possible, at least.

no: All data are below the echo of no defect DSCu/SS boundary

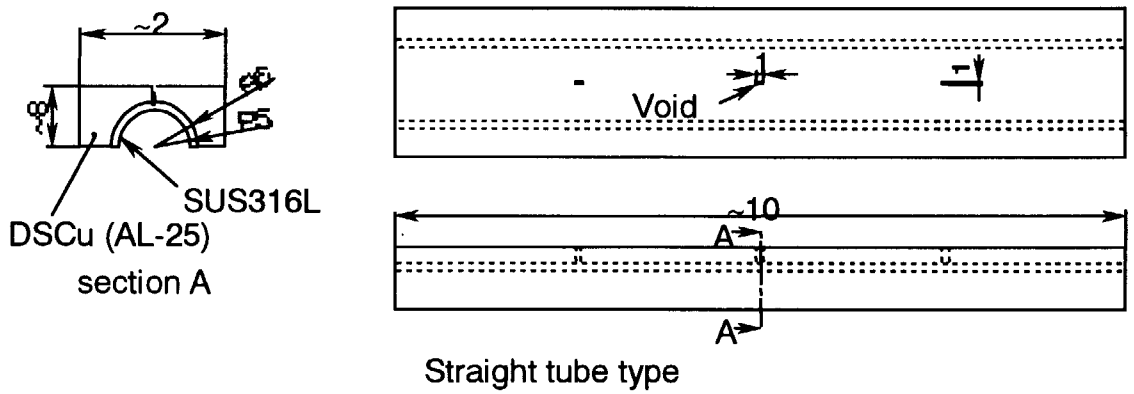

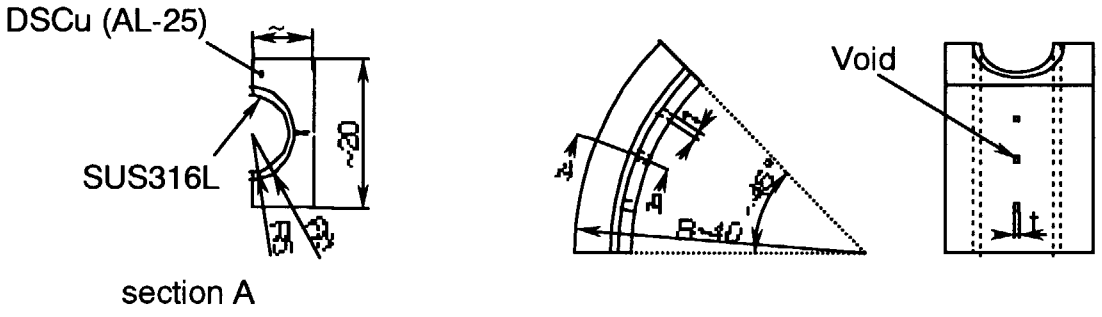

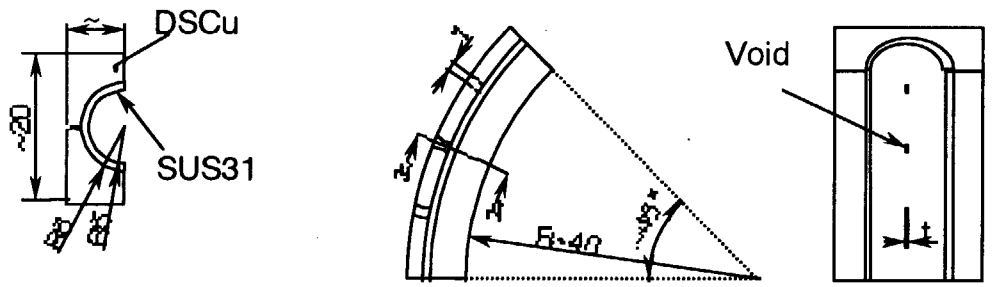

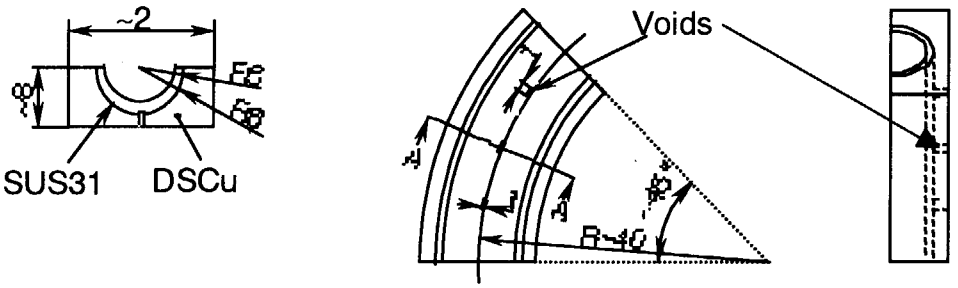

Fig. 2.2-1 Test specimens of NDE development test by UT (defect size = 0.3, 0.6 and 0.9 mm)

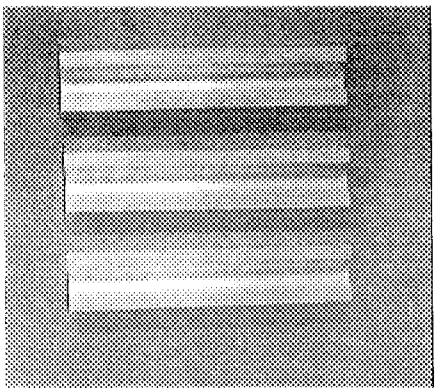

Straight TP (Top View)

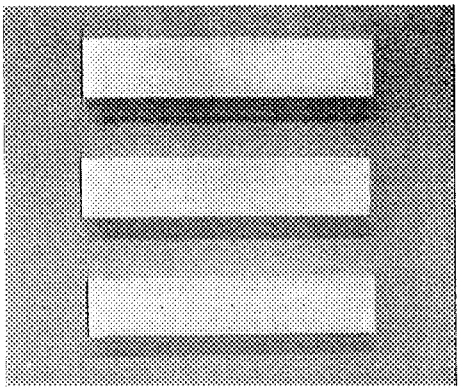

Straight TP (Bottom View)

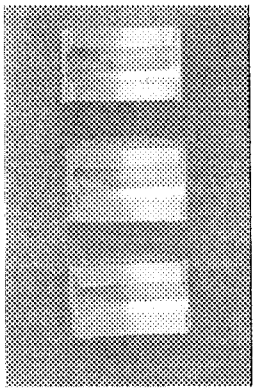

Outside Bent TP

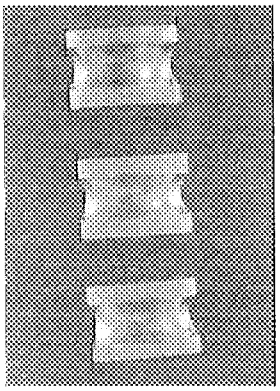

Inside Bent TP

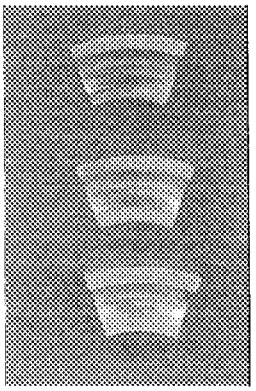

Side Bent TP

Fig. 2.2-2 Photograph of test specimen (artificial defects)

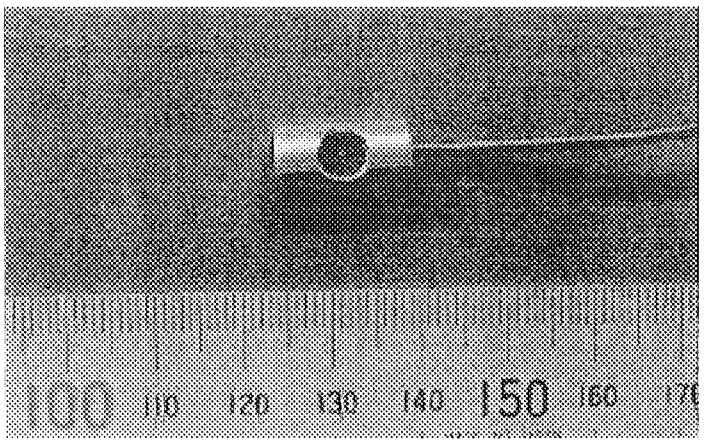

Fig. 2.2-3 Photograph of a sensor applied in this work (Type 1)

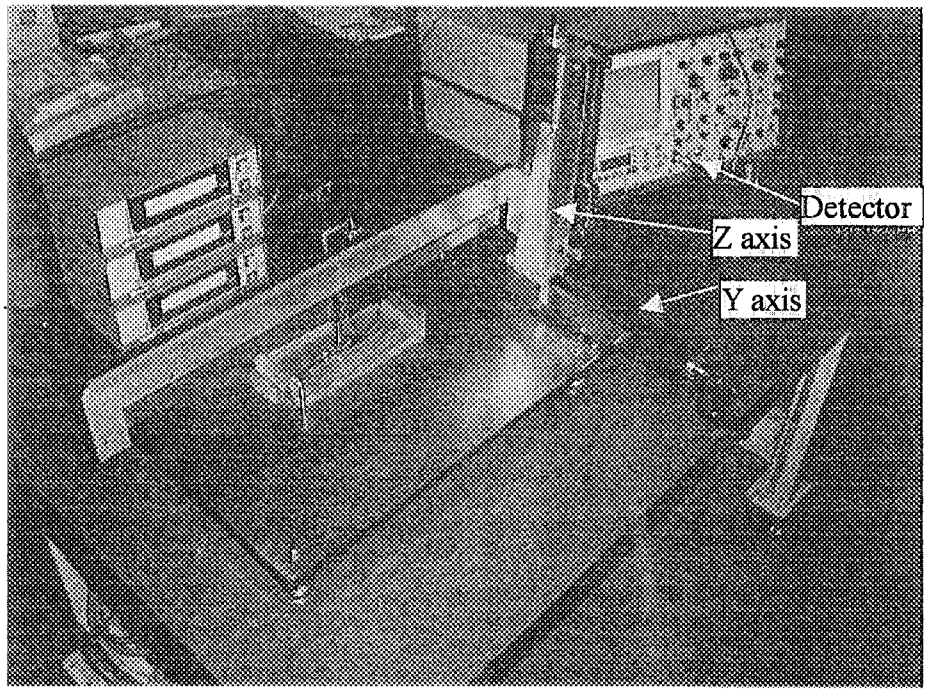

Fig 2.2-4 Scanner basement and location data recorder

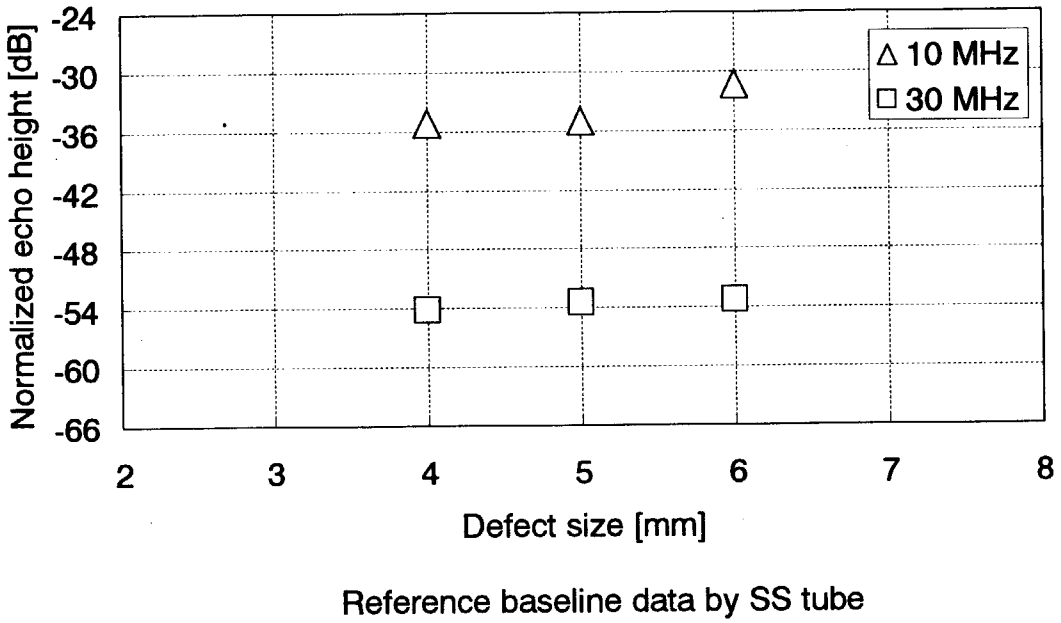

Figure 2.3.1-1 Reference data of echo from back side of simple SS tube as the function of spacer distance

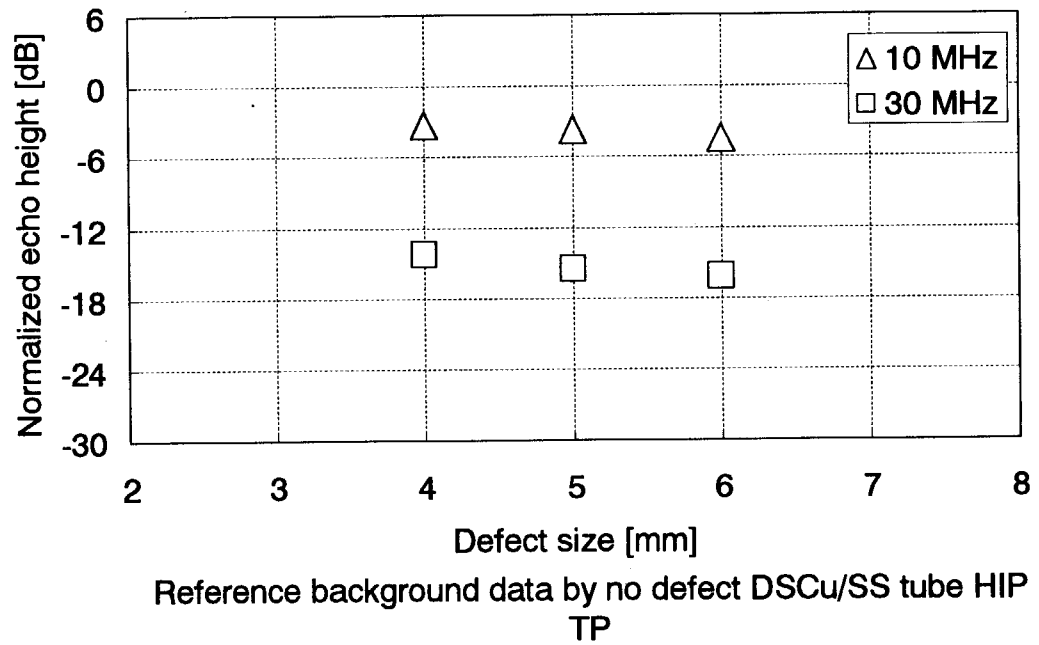

Fig. 2.3.2-1 Characteristics of the reflection wave from DSCu/SS boundary without defect as the function of spacer distance

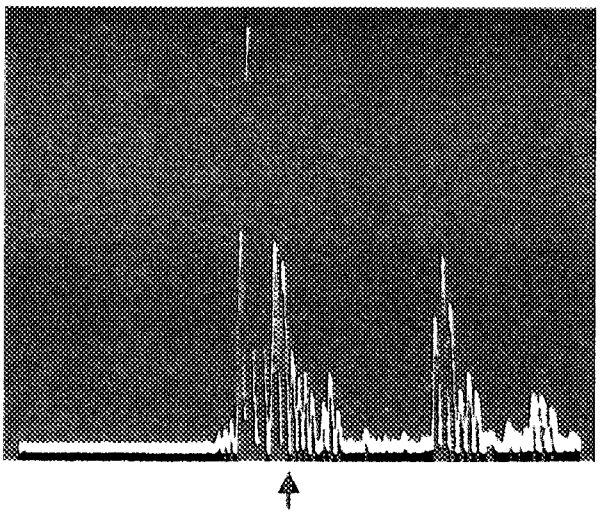

Wave of no defect case

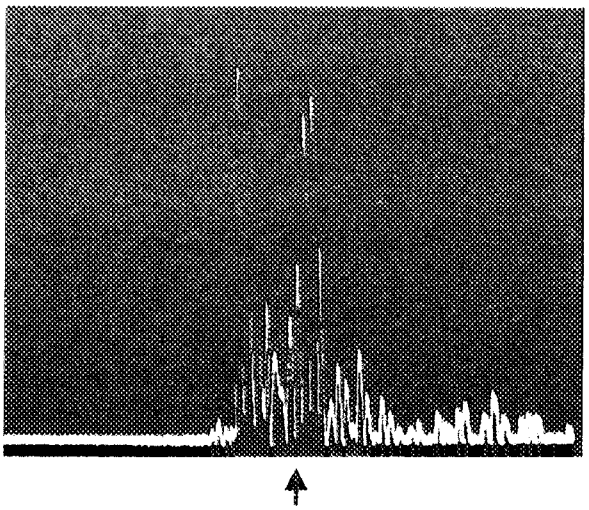

Wave of defect case

Fig. 2.3.3-1 Typical wave photographs of type 1 detector (10 MHz) (comparison of no defect and 0.9 mm defect)

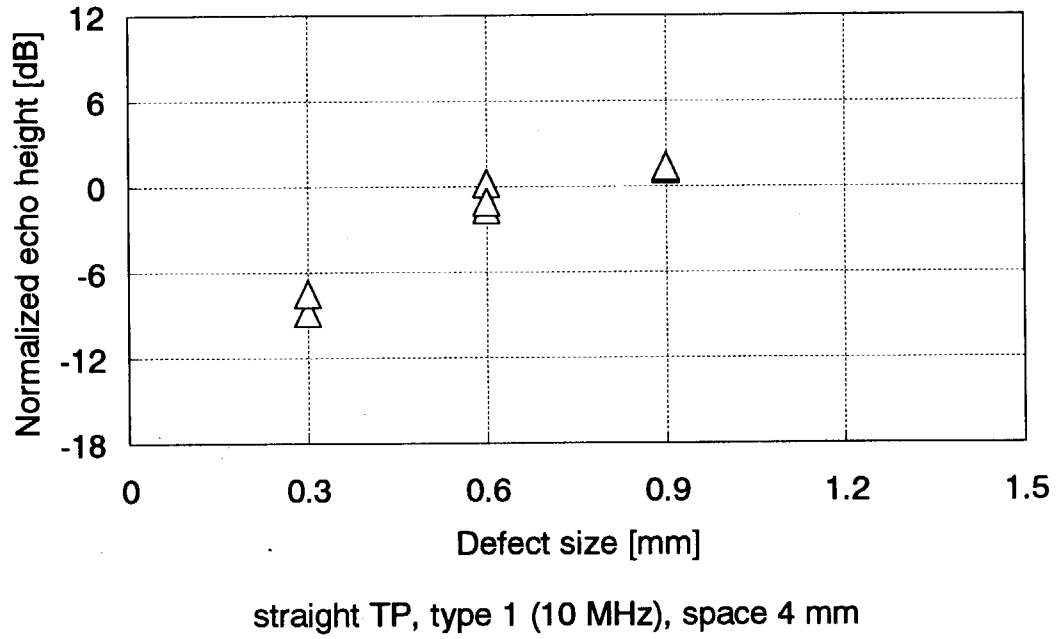

Fig. 2.3.3-2 Characteristics of the echo height from defect of straight TP with 4 mm spacer distance by type 1 probe as a function of defect size

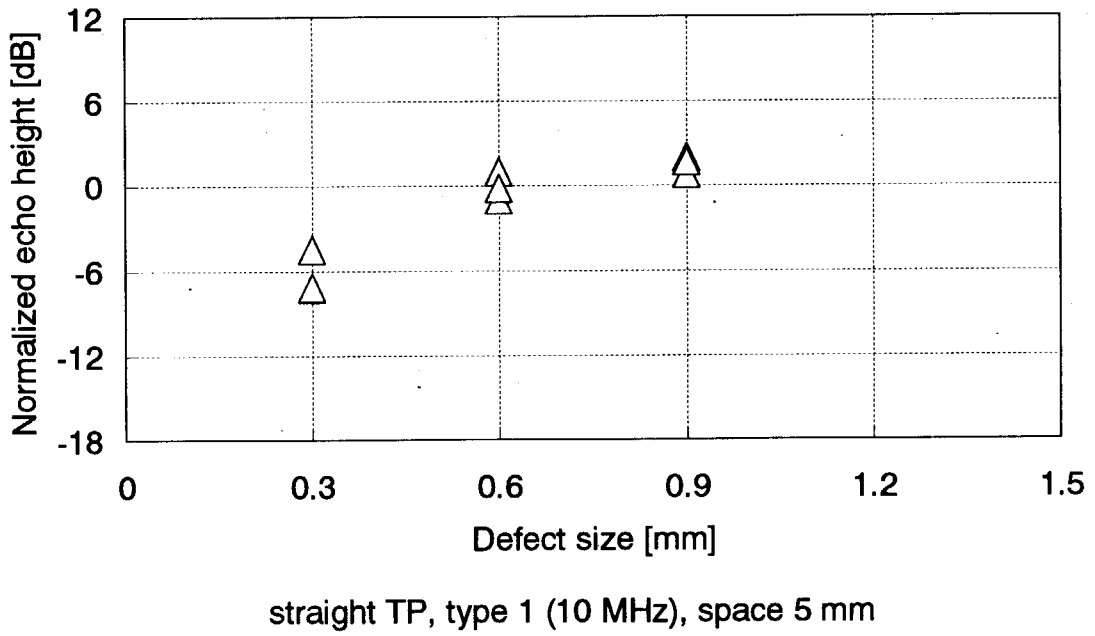

Fig. 2.3.3-3 Characteristics of the echo height from defect of straight TP with 5 mm spacer distance by type 1 probe as a function of defect size

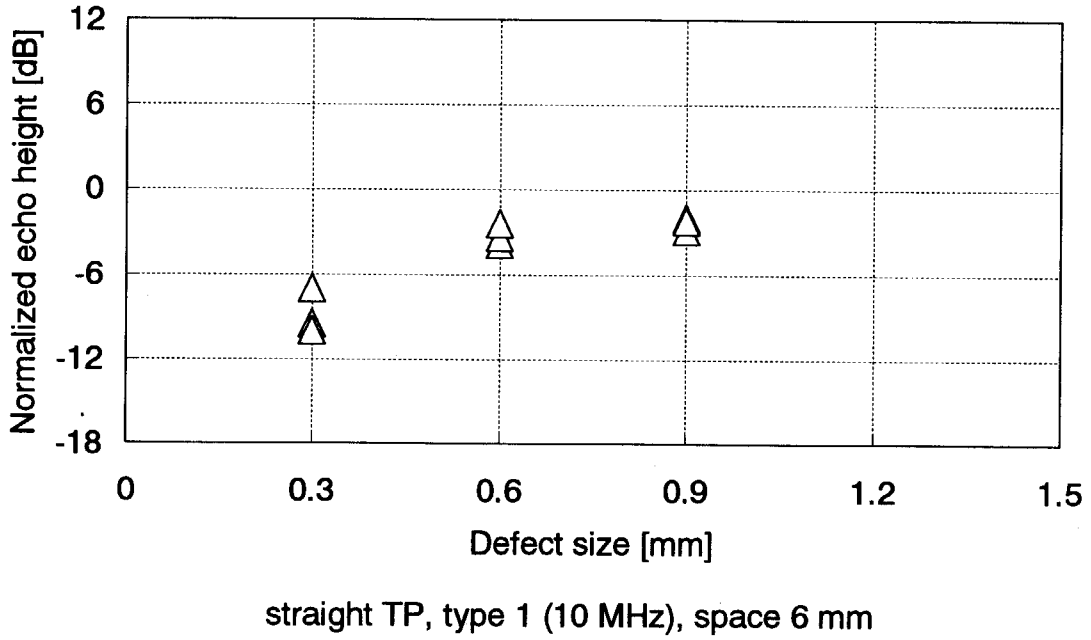

Fig. 2.3.3-4 Characteristics of the echo height from defect of straight TP with 6 mm spacer distance by type 1 probe as a function of defect size

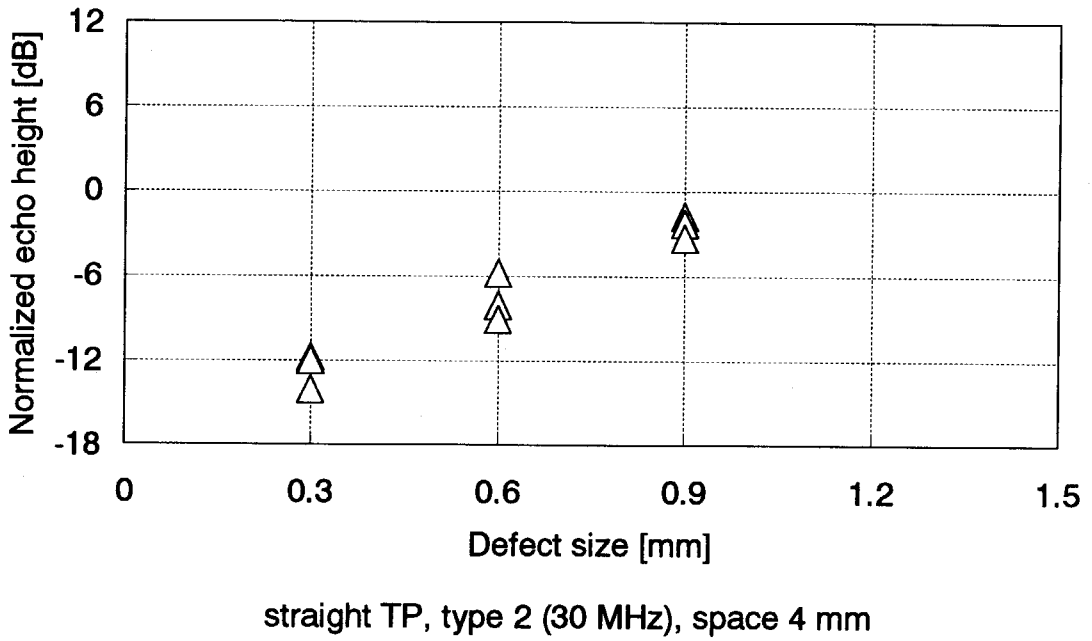

Fig. 2.3.3-5 Characteristics of the echo height from defect of straight TP with 4 mm spacer distance by type 2 probe as a function of defect size

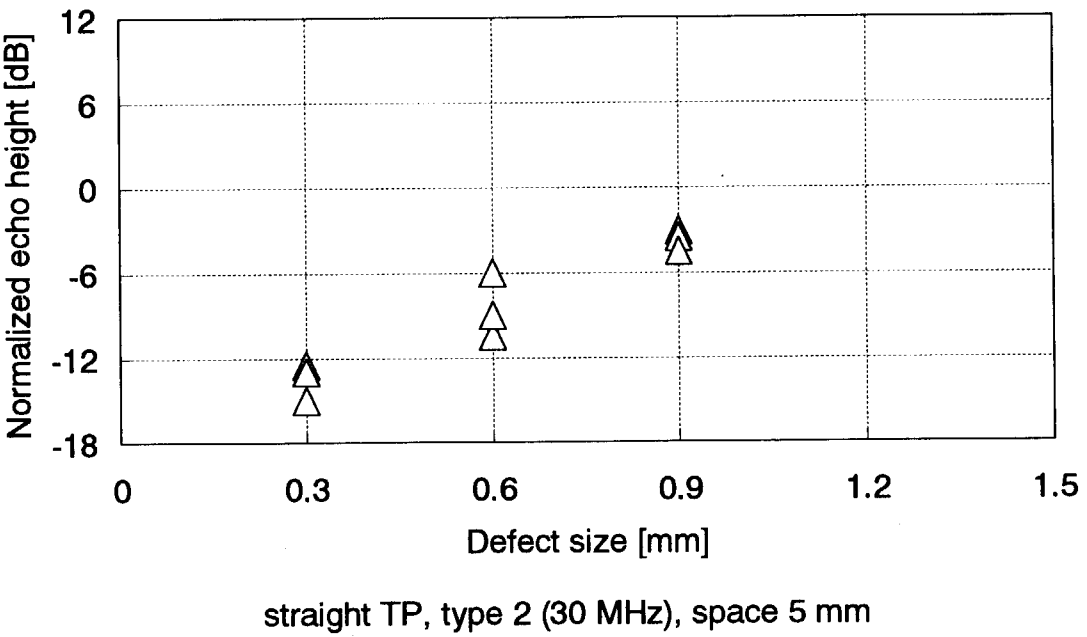

Fig. 2.3.3-6 Characteristics of the echo height from defect of straight TP with 5 mm spacer distance by type 2 probe as a function of defect size

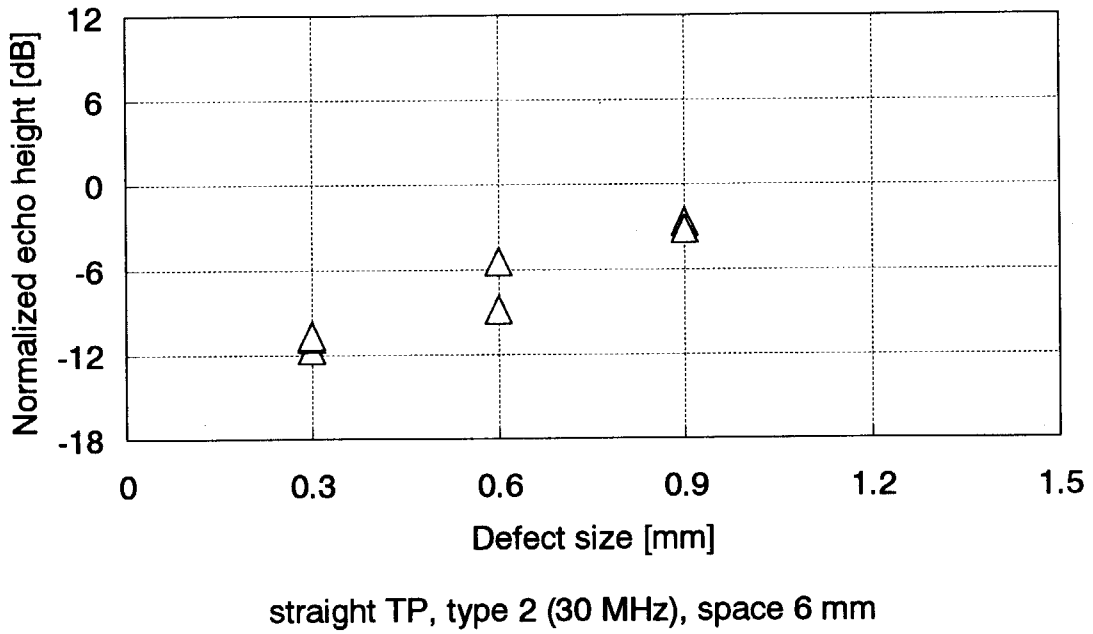

Fig. 2.3.3-7 Characteristics of the echo height from defect of straight TP with 6 mm spacer distance by type 2 probe as a function of defect size

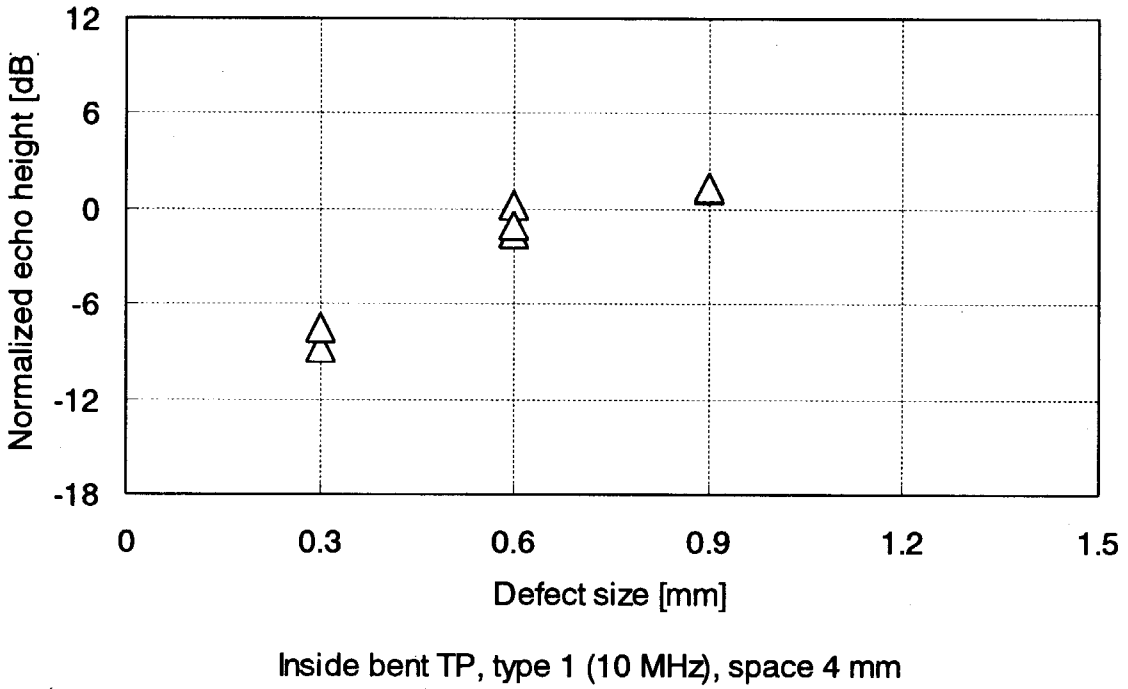

Fig. 2.3.4-1 Characteristics of the echo height from defect of inside bent TP with 4 mm spacer distance by type 1 probe as a function of defect size

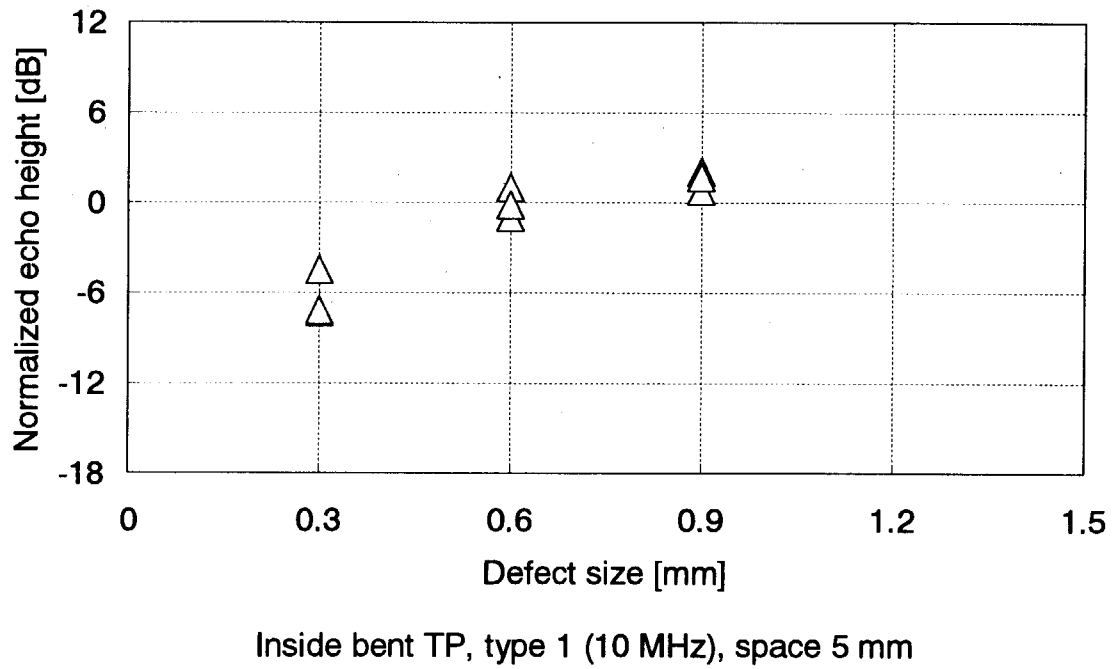

Fig. 2.3.4-2 Characteristics of the echo height from defect of inside bent TP with 5 mm spacer distance by type 1 probe as a function of defect size

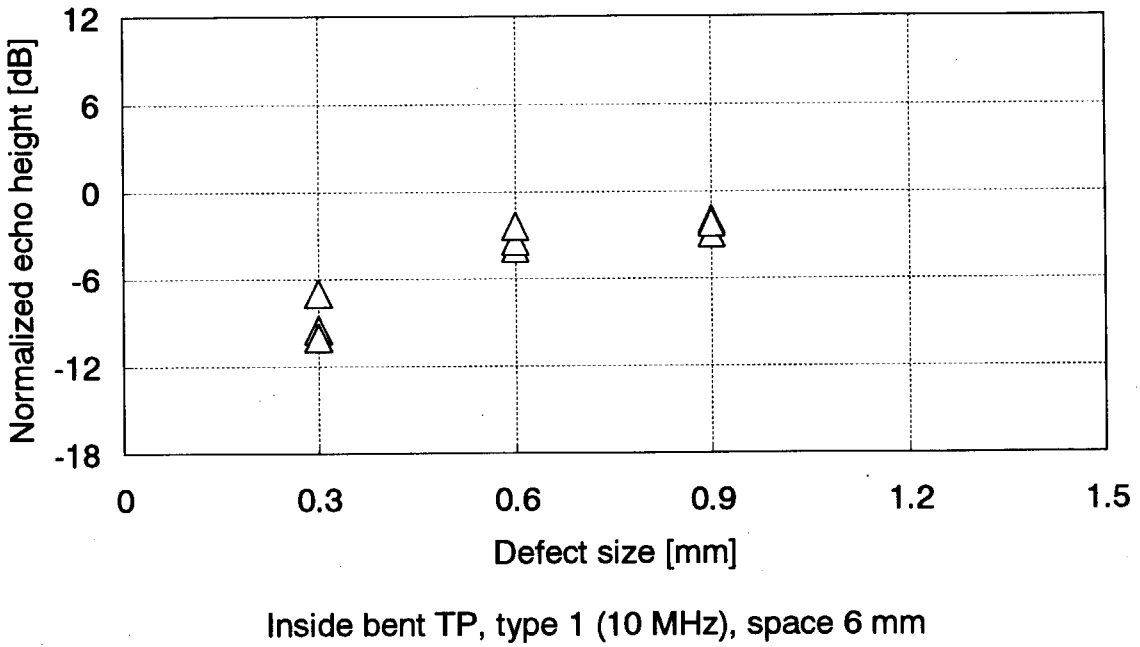

Fig. 2.3.4-3 Characteristics of the echo height from defect of inside bent TP with 6 mm spacer distance by type 1 probe as a function of defect size

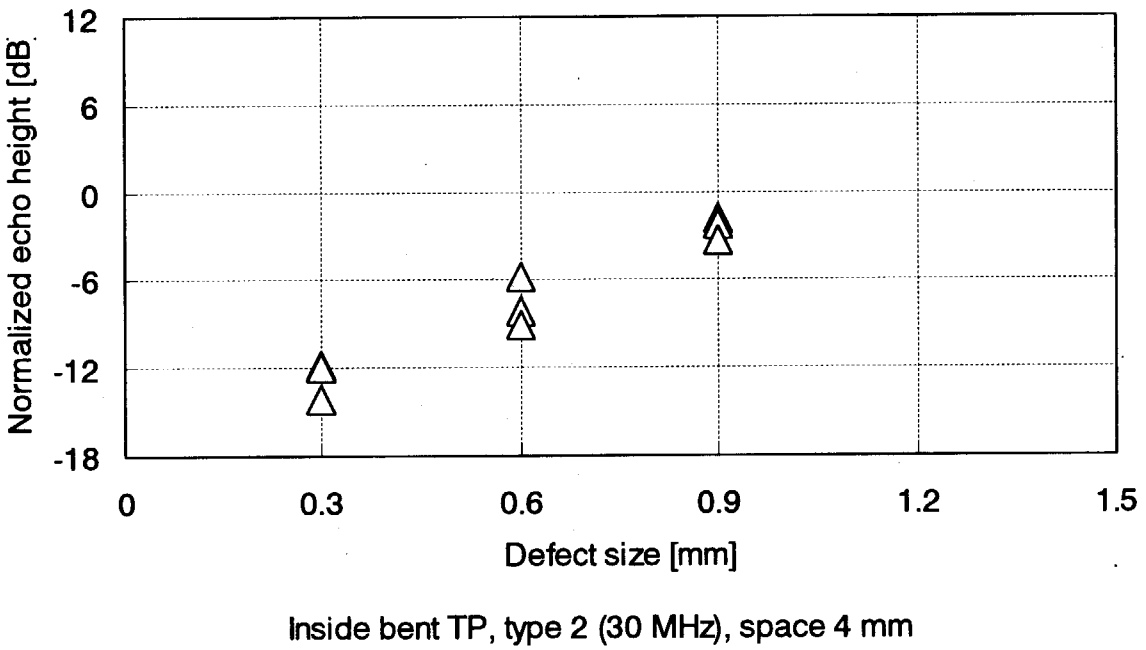

Fig. 2.3.4-4 Characteristics of the echo height from defect of inside bent TP with 4 mm spacer distance by type 2 probe as a function of defect size

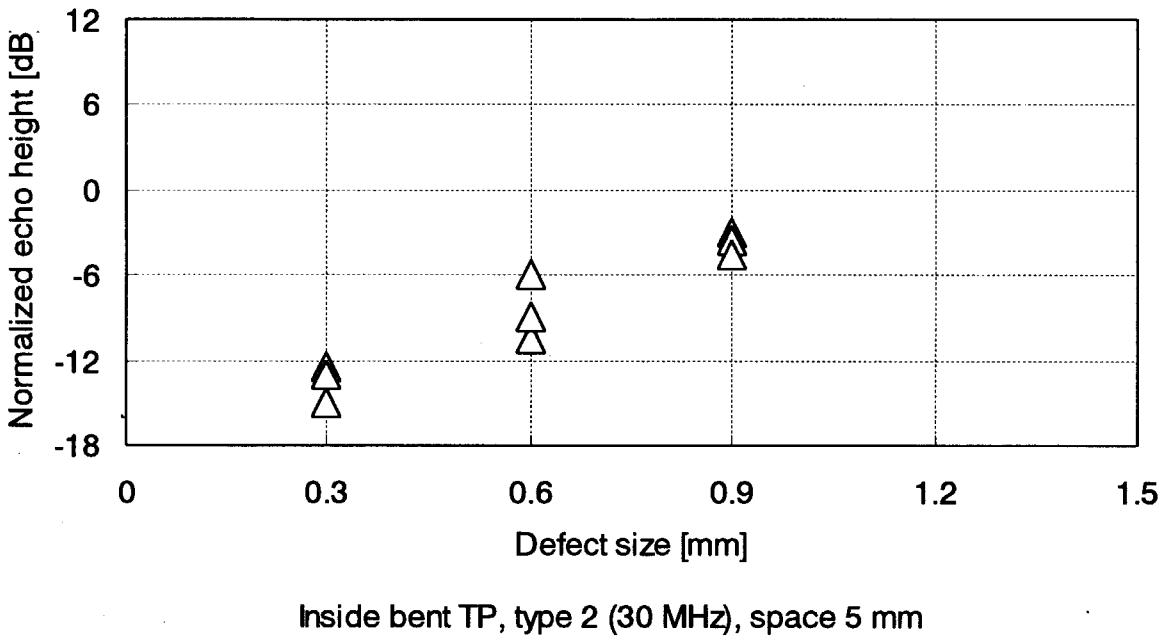

Fig. 2.3.4-5 Characteristics of the echo height from defect of inside bent TP with 5 mm spacer distance by type 2 probe as a function of defect size

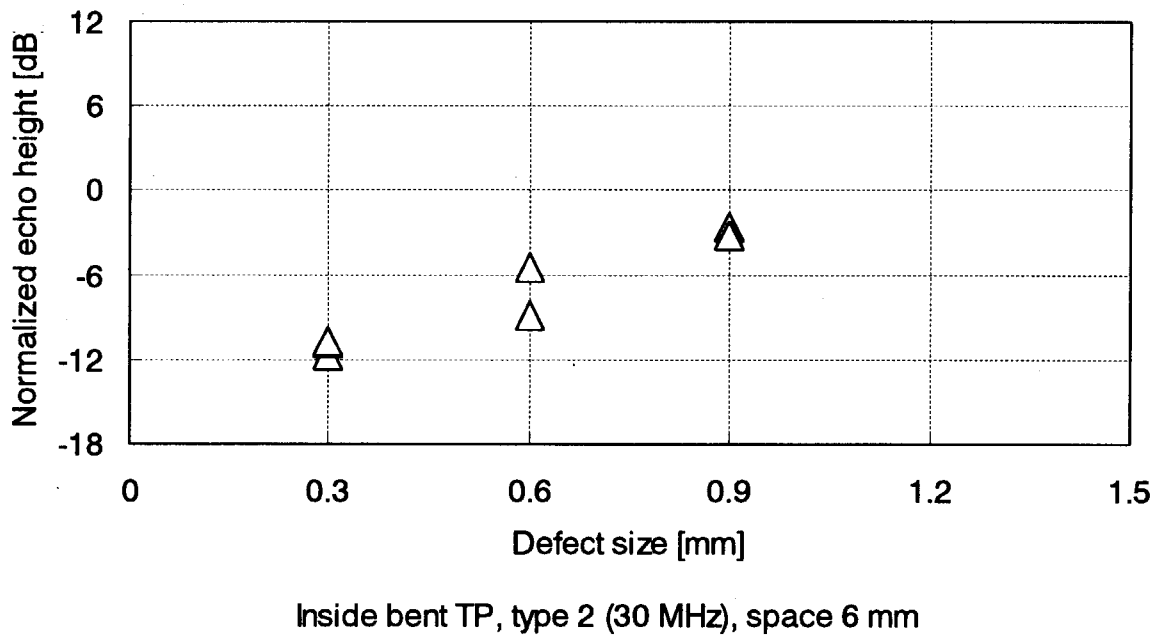

Fig. 2.3.4-6 Characteristics of the echo height from defect of inside bent TP with 6 mm spacer distance by type 2 probe as a function of defect size

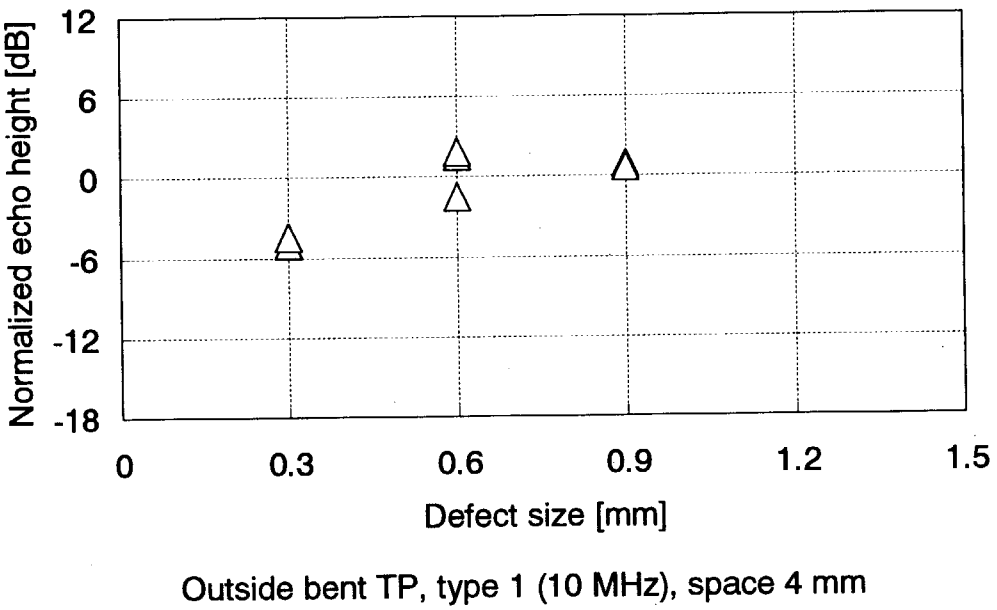

Fig. 2.3.4-7 Characteristics of the echo height from defect of outside bent TP with 4 mm spacer distance by type 1 probe as a function of defect size

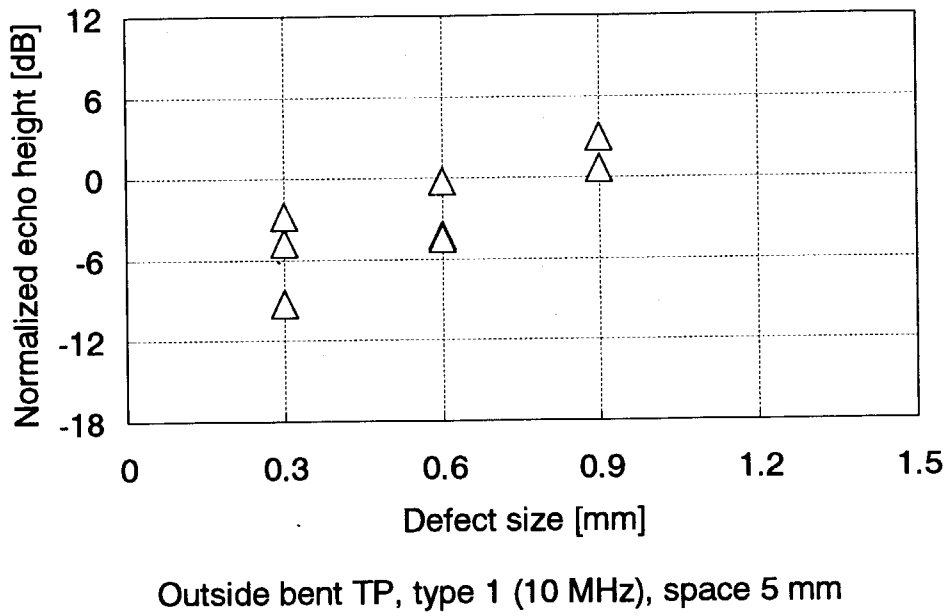

Fig. 2.3.4-8 Characteristics of the echo height from defect of outside bent TP with 5 mm spacer distance by type 1 probe as a function of defect size

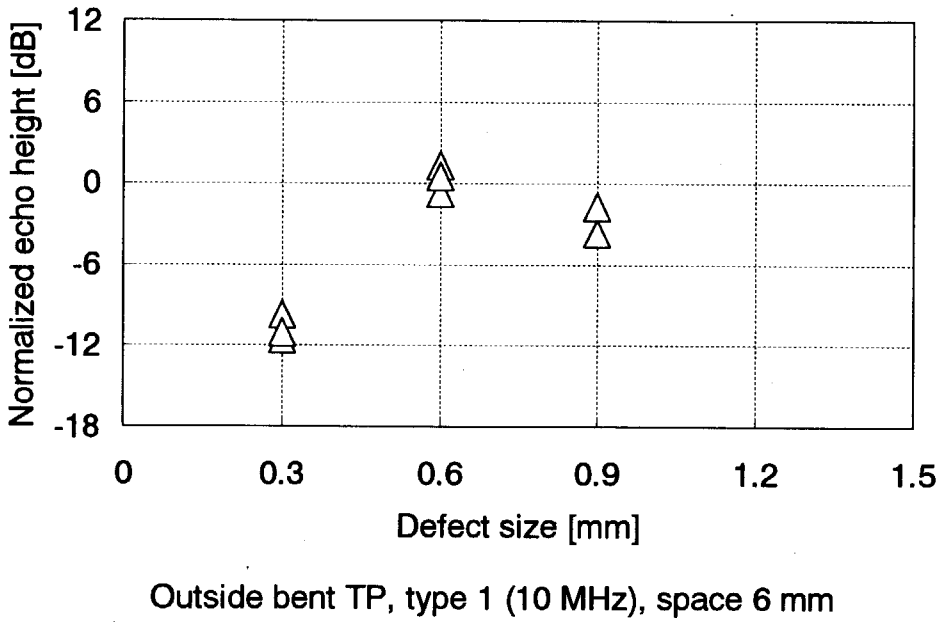

Fig. 2.3.4-9 Characteristics of the echo height from defect of outside bent TP with 6 mm spacer distance by type 1 probe as a function of defect size

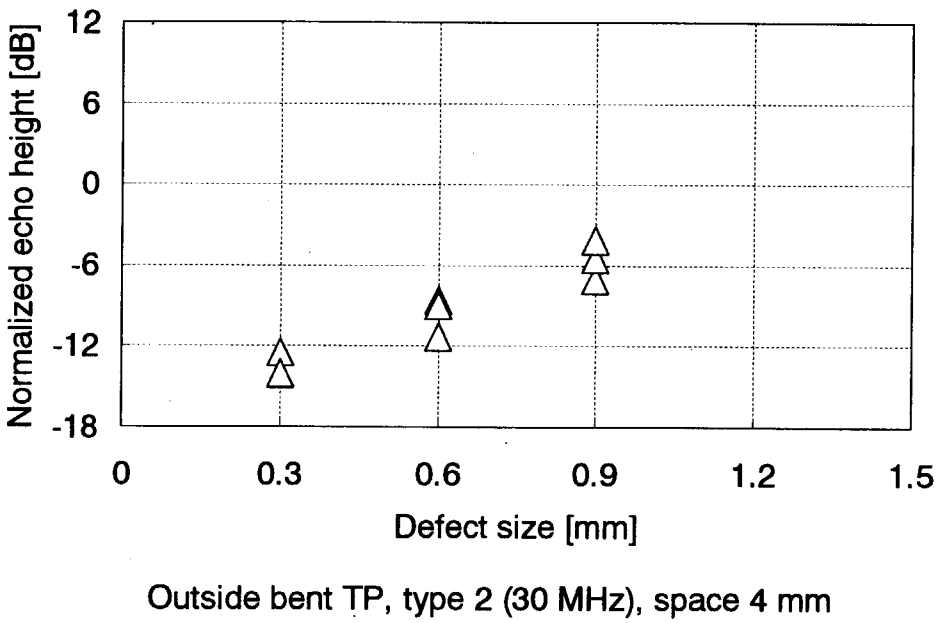

Fig. 2.3.4-10 Characteristics of the echo height from defect of outside bent TP with 4 mm spacer distance by type 2 probe as a function of defect size

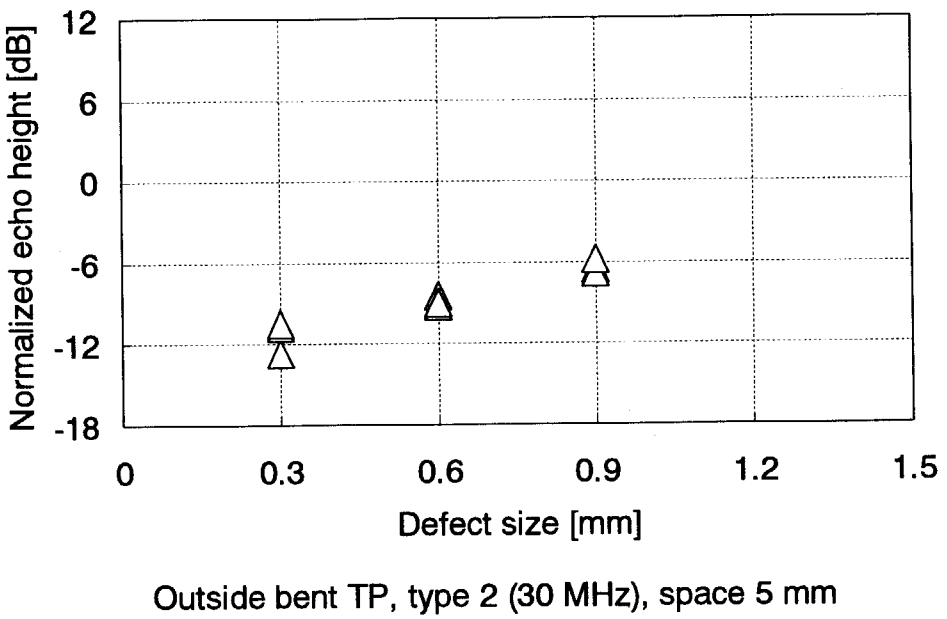

Fig. 2.3.4-11 Characteristics of the echo height from defect of outside bent TP with 5 mm spacer distance by type 2 probe as a function of defect size

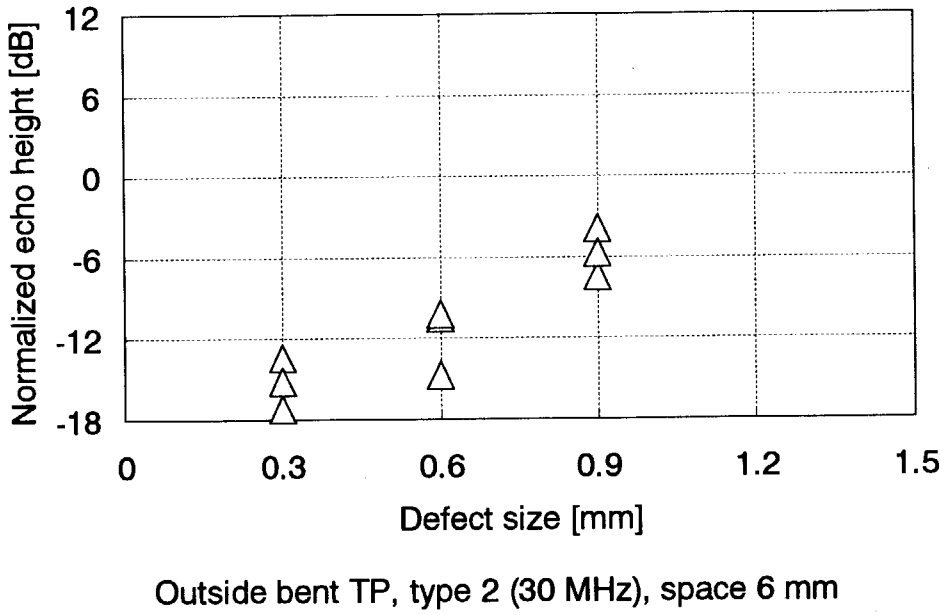

Fig. 2.3.4-12 Characteristics of the echo height from defect of outside bent TP with 6 mm spacer distance by type 2 probe as a function of defect size

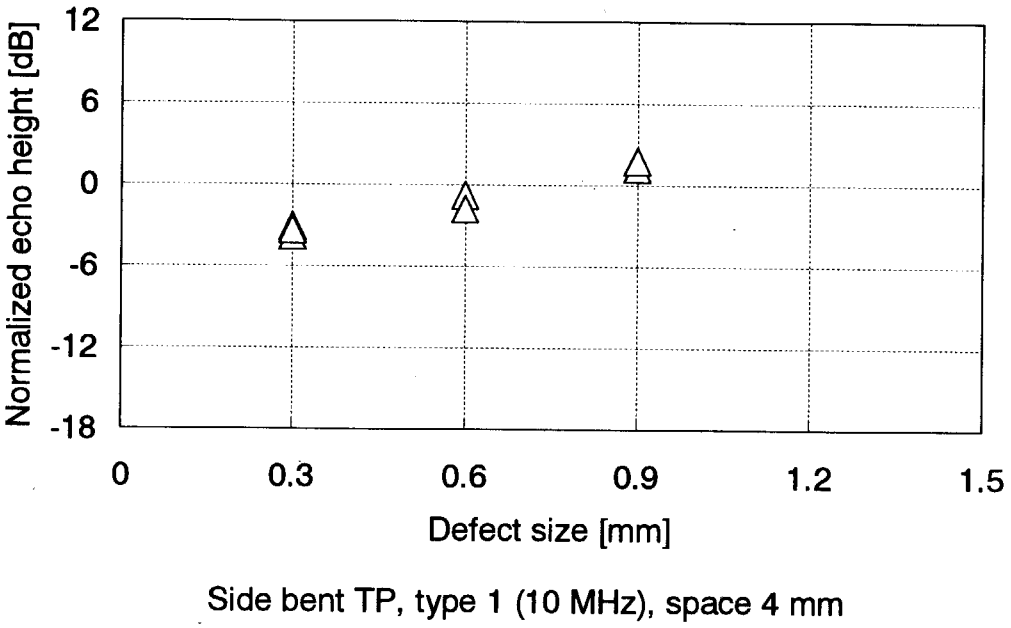

Fig. 2.3.4-13 Characteristics of the echo height from defect of side bent TP with 4 mm spacer distance by type 1 probe as a function of defect size

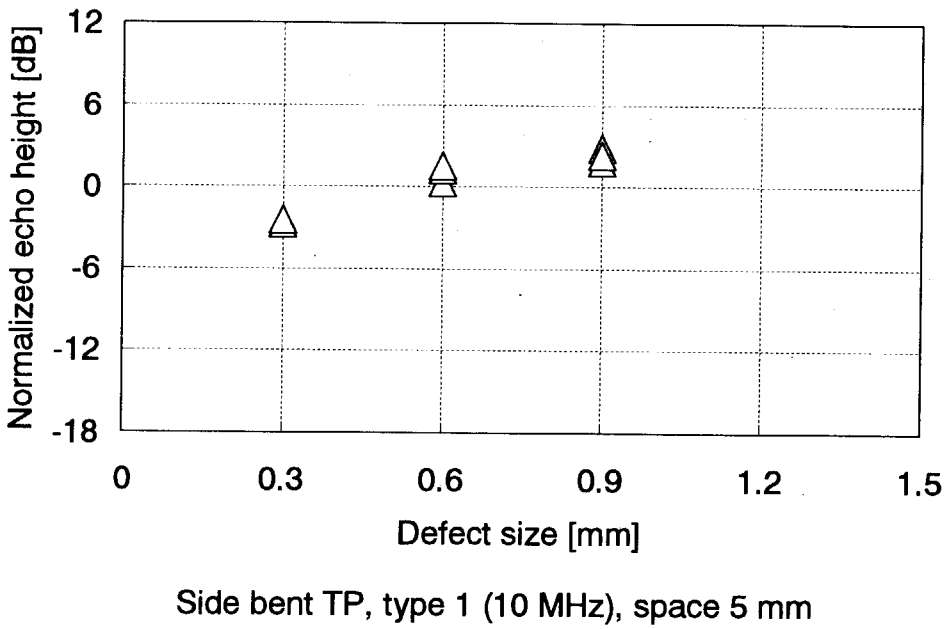

Fig. 2.3.4-14 Characteristics of the echo height from defect of side bent TP with 5 mm spacer distance by type 1 probe as a function of defect size

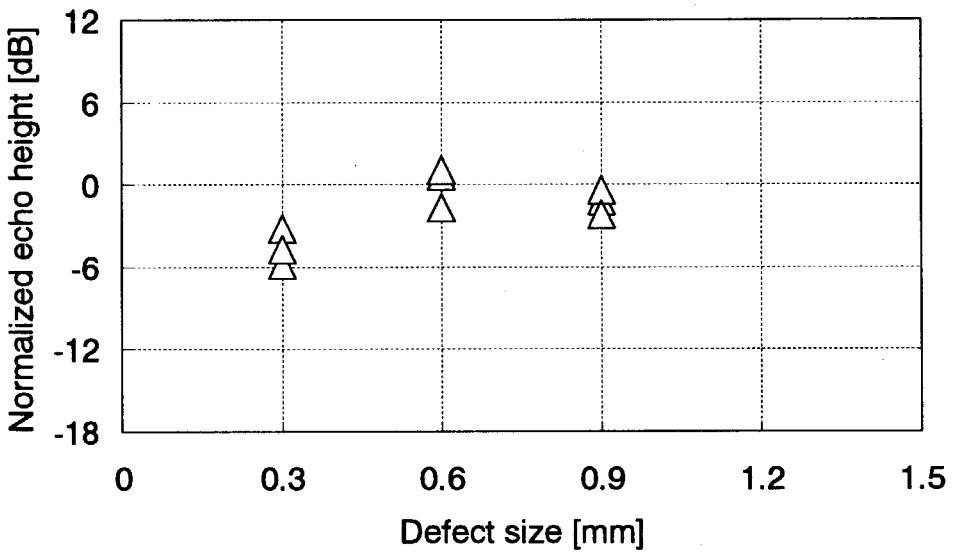

Fig. 2.3.4-15 Characteristics of the echo height from defect of outside bent TP with 6 mm spacer distance by type 1 probe as a function of defect size

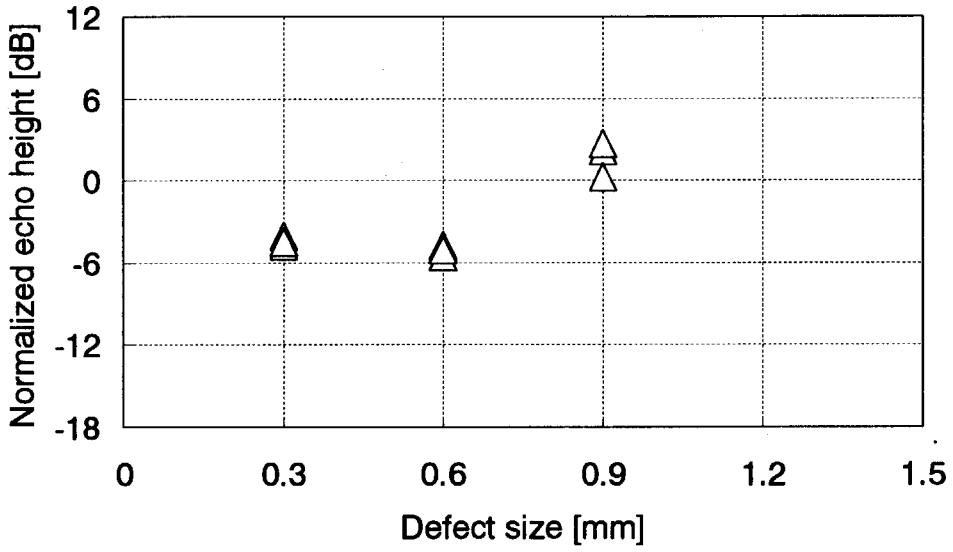

Fig. 2.3.4-16 Characteristics of the echo height from defect of outside bent TP with 4 mm spacer distance by type 2 probe as a function of defect size

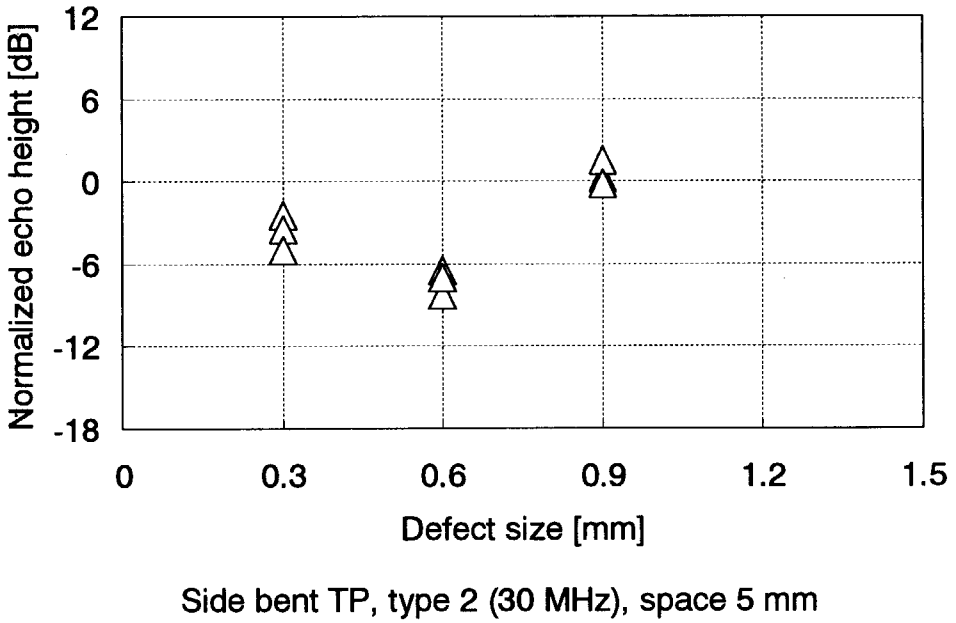

Fig. 2.3.4-17 Characteristics of the echo height from defect of outside bent TP with 5 mm spacer distance by type 2 probe as a function of defect size

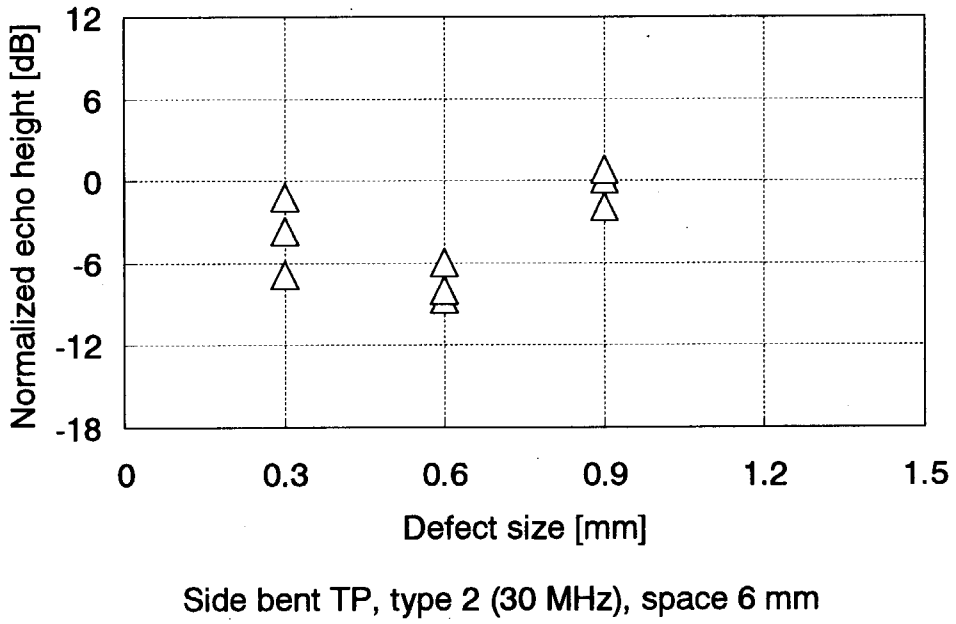

Fig. 2.3.4-18 Characteristics of the echo height from defect of outside bent TP with 6 mm spacer distance by type 2 probe as a function of defect size

4 Conclusions

Subtask 1 demonstrated the final feasibility of the fabrication technique of separable first wall type shielding blanket. Also, in subtask 1, NDE method for FW Cu alloy/SS tube interface by UT was developed. Subtask 2 developed the improved fabrication technique for the application of CuCrZr heat sink material.

By subtask 1, the fabrication technique of full scale width Be armored First Wall Pannel is demonstrated. Also, the fabrication technique of the shield block is demonstrated by using poloidal channel shield blocks. As the R&D for updated cooling channel configuration, the fabrication technique of the radial channel shield block was demonstrated. Concluding to the all R&D results, fabricability of the prototype of the option B separable first wall blanket module was successfully demonstrated. Additionally, UT data was obtained to show the applicability of UT method for in tube access detection of defect on the Cu alloy/SS tube interface. As the result of each fabrication and testing, the followings are concluded.

(1) Joining technique of Be armor and Cu alloy heat sink, and Cu alloy heat sink and SS base panel was developed and demonstrated for the real scale width of FW panel.
(2) Slit formation for FW panels was demonstrated.
(3) Slit formation of a shield block was demonstrated.
(4) Thick header plate welding technique and welding deformation of shield blocks was optimized.
(5) Welding technique for one quarter shield blocks by EB welding was optimized.
(6) Fabricability of radial cooling channel shield block was demonstrated.
(7) Non destructive examination method development for FW Cu alloy/SS cooling channel was performed and the basic detection data was clarified.

Acknowledgement

The authors wish to express sincere appreciation to Dr. Masahiro Seki, Dr. Hideyuki Takatsu and Dr. Syogo Seki for their continuous encouragement. Also, the authors wish to express special gratitude to Dr. Kimihiro Ioki and Dr. Antonio Cardella of ITER JCT for their guidance of R&D items. The authors acknowledge the tremendous contributions by Kawasaki Heavy Industries, Ltd. and NGK Insulators, Ltd. to accomplish this work.

References

[1] Final Report of the ITER Engineering Design Activities, ITER EDA IC Vienna ROD Attachment 7 (2001).
[2] S. Sato, et al., J. Nucl. Mater. ,233-237, 940-944 (1996)
[3] S. Sato, et al., J. Nucl. Mater., 258-263, 265-270 (1998)
[4] T. Hatano, et al., J. Nucl. Mater., 258-263, 950-954 (1998)
[5] T. Kuroda, et al., J. Nucl. Mater., 258-263, 258-264 (1998)
[6] T. Hatano, et al., Proc. 10th Int. Conf. Fusion React. Mater., Baden-Baden, Germany, Oct. 2001
[7] K. Furuya, et al., Proc. 19th Symp. Fusion Technol., Lisbon, Portugal, Sept. 1996, pp. 1343-1346
[8] S. Sato, et al., Fusion Eng. Des., 39-40, 765-773 (1998)
[9] S. Sato, et al., Fusion Eng. Des., 39-40, 609-614 (1998)
[10] S. Sato, et al., FUSION TECHNOL., 34, 892-897 (1998)

[11] T. Hatano, et al., Fusion Eng. Des., 39-40, 363-370 (1998)
[12] M. Akiba, et al., Plasma Dev. Oper. 1, 205 (1991)

国際単位系 (SI) と換算表

表 1　SI 基本単位および補助単位

量	名称	記号
長さ	メートル	m
質量	キログラム	kg
時間	秒	s
電流	アンペア	A
熱力学温度	ケルビン	K
物質量	モル	mol
光度	カンデラ	cd
平面角	ラジアン	rad
立体角	ステラジアン	sr

表 2　SI と併用される単位

名称	記号
分，時，日	min，h，d
度，分，秒	°，′，″
リットル	l，L
トン	t
電子ボルト	eV
原子質量単位	u

1 eV = 1.60218 × 10^{-19} J

1 u = 1.66054 × 10^{-27} kg

表 5　SI 接頭語

倍数	接頭語	記号
10^{18}	エクサ	E
10^{15}	ペタ	P
10^{12}	テラ	T
10^{9}	ギガ	G
10^{6}	メガ	M
10^{3}	キロ	k
10^{2}	ヘクト	h
10^{1}	デカ	da
10^{-1}	デシ	d
10^{-2}	センチ	c
10^{-3}	ミリ	m
10^{-6}	マイクロ	μ
10^{-9}	ナノ	n
10^{-12}	ピコ	p
10^{-15}	フェムト	f
10^{-18}	アト	a

表 3　固有の名称をもつ SI 組立単位

量	名称	記号	他の SI 単位による表現
周波数	ヘルツ	Hz	s^{-1}
力	ニュートン	N	$m \cdot kg/s^2$
圧力，応力	パスカル	Pa	N/m^2
エネルギー，仕事，熱量	ジュール	J	N·m
工率，放射束	ワット	W	J/s
電気量，電荷	クーロン	C	A·s
電位，電圧，起電力	ボルト	V	W/A
静電容量	ファラド	F	C/V
電気抵抗	オーム	Ω	V/A
コンダクタンス	ジーメンス	S	A/V
磁束	ウェーバ	Wb	V·s
磁束密度	テスラ	T	Wb/m^2
インダクタンス	ヘンリー	H	Wb/A
セルシウス温度	セルシウス度	℃	
光束	ルーメン	lm	cd·sr
照度	ルクス	lx	lm/m^2
放射能	ベクレル	Bq	s^{-1}
吸収線量	グレイ	Gy	J/kg
線量当量	シーベルト	Sv	J/kg

表 4　SI と共に暫定的に維持される単位

名称	記号
オングストローム	Å
バーン	b
バール	bar
ガル	Gal
キュリー	Ci
レントゲン	R
ラド	rad
レム	rem

1 Å = 0.1 nm = 10^{-10} m

1 b = 100 fm^2 = 10^{-28} m^2

1 bar = 0.1 MPa = 10^5 Pa

1 Gal = 1 cm/s^2 = 10^{-2} m/s^2

1 Ci = 3.7 × 10^{10} Bq

1 R = 2.58 × 10^{-4} C/kg

1 rad = 1 cGy = 10^{-2} Gy

1 rem = 1 cSv = 10^{-2} Sv

（注）

1. 表 1－5 は「国際単位系」第 5 版，国際度量衡局 1985 年刊行による。ただし，1 eV および 1 u の値は CODATA の 1986 年推奨値によった。
2. 表 4 には海里，ノット，アール，ヘクタールも含まれているが日常の単位なのでここでは省略した。
3. bar は，JIS では流体の圧力を表わす場合に限り表 2 のカテゴリーに分類されている。
4. EC 閣僚理事会指令では bar，barn および「血圧の単位」mmHg を表 2 のカテゴリーに入れている。

換　算　表

力	N(=10^5 dyn)	kgf	lbf
	1	0.101972	0.224809
	9.80665	1	2.20462
	4.44822	0.453592	1

粘　度　1 Pa·s(N·s/m^2) = 10 P(ポアズ)(g/(cm·s))

動粘度　1 m^2/s = 10^4 St(ストークス)(cm^2/s)

圧力	MPa(=10 bar)	kgf/cm^2	atm	mmHg(Torr)	lbf/in^2(psi)
	1	10.1972	9.86923	7.50062 × 10^3	145.038
	0.0980665	1	0.967841	735.559	14.2233
	0.101325	1.03323	1	760	14.6959
	1.33322 × 10^{-4}	1.35951 × 10^{-3}	1.31579 × 10^{-3}	1	1.93368 × 10^{-2}
	6.89476 × 10^{-3}	7.03070 × 10^{-2}	6.80460 × 10^{-2}	51.7149	1

エネルギー・仕事・熱量	J(=10^7 erg)	kgf·m	kW·h	cal(計量法)	Btu	ft·lbf	eV
	1	0.101972	2.77778 × 10^{-7}	0.238889	9.47813 × 10^{-4}	0.737562	6.24150 × 10^{18}
	9.80665	1	2.72407 × 10^{-6}	2.34270	9.29487 × 10^{-3}	7.23301	6.12082 × 10^{19}
	3.6 × 10^6	3.67098 × 10^5	1	8.59999 × 10^5	3412.13	2.65522 × 10^6	2.24694 × 10^{25}
	4.18605	0.426858	1.16279 × 10^{-6}	1	3.96759 × 10^{-3}	3.08747	2.61272 × 10^{19}
	1055.06	107.586	2.93072 × 10^{-4}	252.042	1	778.172	6.58515 × 10^{21}
	1.35582	0.138255	3.76616 × 10^{-7}	0.323890	1.28506 × 10^{-3}	1	8.46233 × 10^{18}
	1.60218 × 10^{-19}	1.63377 × 10^{-20}	4.45050 × 10^{-26}	3.82743 × 10^{-20}	1.51857 × 10^{-22}	1.18171 × 10^{-19}	1

1 cal = 4.18605 J (計量法)

= 4.184 J (熱化学)

= 4.1855 J (15 °C)

= 4.1868 J (国際蒸気表)

仕事率　1 PS (仏馬力)

= 75 kgf·m/s

= 735.499 W

放射能	Bq	Ci
	1	2.70270 × 10^{-11}
	3.7 × 10^{10}	1

吸収線量	Gy	rad
	1	100
	0.01	1

照射線量	C/kg	R
	1	3876
	2.58 × 10^{-4}	1

線量当量	Sv	rem
	1	100
	0.01	1

（86 年 12 月 26 日現在）

Fabrication of Prototype Mockups of ITER Shielding Blanket with Separable First Wall

R100
古紙配合率100%
白色度70%再生紙を使用しています